BRNO UNIVERSITY OF TECHNOLOGY
VYSOKÉ UČENÍ TECHNICKÉ V BRNĚ

FACULTY OF CHEMISTRY
FAKULTA CHEMICKÁ

INSTITUTE OF PHYSICAL AND APPLIED CHEMISTRY
ÚSTAV FYZIKÁLNÍ A SPOTŘEBNÍ CHEMIE

NEURAL BIOCERAMIC SCAFFOLD PREPARED BY FREEZE-CASTING

BIOKERAMICKÝ SKAFOLD PRO VEDENÍ NERVŮ PŘIPRAVENÝ METODOU FREEZE-CASTING

MASTER'S THESIS
DIPLOMOVÁ PRÁCE

AUTHOR
AUTOR PRÁCE

Bc. Michaela Vojníková

SUPERVISOR
VEDOUCÍ PRÁCE

doc. Ing. David Salamon, Ph.D.

BRNO 2021

BRNO UNIVERSITY OF TECHNOLOGY
FACULTY OF CHEMISTRY

Specification Master's Thesis

Project no.:	FCH-DIP1526/2020	Academic year:	2020/21
Department:	Institute of Physical and Applied Chemistry		
Student:	**Bc. Michaela Vojníková**		
Study programme:	Chemistry for Medical Applications		
Study field:	Chemistry for Medical Applications		
Head of thesis:	**doc. Ing. David Salamon, Ph.D.**		

Title of Master's Thesis:

Neural bioceramic scaffold prepared by freeze–casting

Master's Thesis:

1. Literature review of neural scaffolds and a possible application of the freeze–casting method.
2. Preparation of calcium phosphate–based ceramic materials by freeze–casting with macro and microstructures suitable for neural scaffolds.
3. Analysis and evaluation of impact of the shaping method on microstructure, mechanical and biological properties.

Deadline for Master's Thesis delivery: 28.5.2021:

Master's Thesis should be submitted to the institute's secretariat in a number of copies as set by the dean This specification is part of Master's Thesis

Bc. Michaela Vojníková Student	doc. Ing. David Salamon, Ph.D. Head of thesis	prof. Ing. Miloslav Pekař, CSc. Head of department

In Brno dated 1.2.2021

prof. Ing. Martin Weiter, Ph.D.
Dean

ABSTRAKT

Pre regeneráciu a rast poranených nervových vlákien bolo preskúmaných mnoho postupov, no výsledný rast axónov je často náhodný až dezorganizovaný a odráža sa na zložitejšom zotavovaní pacienta. V tejto práci boli vyrobené nové skafoldy s mikroštruktúrnymi a mechanickými vlastnosťami nervového skafoldu pomocou metódy freeze-casting. Konkrétne boli vyrobené biokeramické skafoldy na báze fosforečnanov vápenatých, oxidu titaničitého alebo oxidu zirkoničitého. Pomocou kontrolovaného rastu ľadu v jednom smere bola pripravená orientovaná mikroštruktúra. Pozorovanie pomocou skenovacej elektrónovej mikroskopie potvrdilo lineárne orientované póry (lamelárny systém), v ktorých priemerná veľkosť pórov klesala so zvyšujúcou sa rýchlosťou mrazenia. Skafoldy pripravené pomocou mrazenia v tekutom dusíku vykazovali vynikajúce mechanické vlastnosti, kde pevnosť v ohybe bola získaná v rozmedzí 10–17 MPa. Tie isté skafoldy mali vzdialenosť medzilamelamelárnych priestorov 10–30 μm, ktorých parametre sú vhodné pre nervové skafoldy. Biokompatibilita bola vyhodnotená pomocou Schwannových buniek *in vitro*, kde bola pozorovaná adhézia a rast v lamelárnom smere. Cytotoxické testy odhalili negatívny vplyv vyššej koncentrácie vápnika na prežitie Schwannových buniek. Pripravené skafoldy mali schopnosť tvorby apatitu na povrchu v podobe embryonálnych a nukleačných centier a apatitu samotného. Skafoldy na báze fosforečnanov vápenatých a oxidu titaničitého vykazovali sľubné regeneračné vlastnosti, konkrétne adhéziu a rast prostredníctvom pórovitej štruktúry a taktiež vynikajúce mechanické vlastnosti.

KĽÚČOVÉ SLOVÁ

fosforečnany vápenaté, oxid titaničitý, oxid zirkoničitý, biokeramika, nervový skafold, freeze-casting, Schwannove bunky

ABSTRACT

Several procedures have been investigated for the regeneration of injured nerves. However, the resulting axonal growth can be random or disorganized and has limitations reflected on patient recovery. Therefore, the novel freeze-casted scaffolds were manufactured with mechanical and microstructural properties suitable for the neural scaffold. Concretely, the bioceramic scaffolds were based on calcium phosphates, titania, and zirconia. The oriented microstructure was prepared by controlled ice growth in one direction. The observation with scanning electron microscopy confirmed linearly oriented pores (lamellar system) in which average pore size decreased with a higher freezing rate. According to the results, the scaffolds prepared by freezing in liquid nitrogen showed excellent mechanical properties, where flexural strength was in the range of 10–17 MPa. Interlamellar distances of these scaffolds were 10–30 µm, which are appropriate for neural scaffolds. Biocompatibility was evaluated with Schwann cells' line *in vitro*, where the adhesion and growth in the lamellar direction were observed. Cytotoxic tests revealed a negative impact of a high calcium level on Schwann cell' survival. The prepared scaffolds could form an apatite layer on its surface in the form of embryonic and nucleation centers and apatite itself. Calcium phosphate and titania scaffolds exhibited promising regenerative characteristics of adhesion and ingrowth through porous structures with outstanding mechanical properties.

KEYWORDS

calcium phosphates, titania, zirconia, bioceramic, neural scaffold, freeze-casting, Schwann cells

VOJNÍKOVÁ, Michaela. *Biokeramický skafold pro vedení nervů připravený metodou freeze-casting*. Brno, 2021. Dostupné také z: https://www.vutbr.cz/studenti/zav-prace/detail/129784. Diplomová práce. Vysoké učení technické v Brně, Fakulta chemická, Ústav fyzikální a spotřební chemie. Vedoucí práce David Salamon.

ACKNOWLEDGEMENT

Firstly, I would like to thank my supervisor, doc. Ing. David Salamon, PhD., for his helpful and scientific supervision, thoughtful comments and recommendations, and patience during my studies. Further, I would like to thank M.Sc. Maliha Siddiqui, who took the microstructural photos, and Dr. Hana Michálková, who helped me with an evaluation of biological properties.

DECLARATION

I declare that the diploma thesis has been worked out by myself and that all the quotations from the used literary sources are accurate and complete. The content of the diploma thesis is the property of the Faculty of Chemistry of Brno University of Technology and all commercial uses are allowed only if approved by both the supervisor and the dean of the Faculty of Chemistry, BUT.

.....

Student´s signature

TABLE OF CONTENT

1 INTRODUCTION

The regeneration of peripheral nerve injuries with tissue-engineered scaffolds has been studied for over 30 years. The peripheral nerve system (PNS) has an excellent regenerative ability for minor damages. If the damage is major, the tissue lost control in a large area; the recovery is too difficult or impossible. Autologous nerve grafting of a less important nerve site is the current "golden standard" to reconstruct injuries and defects. The autograft (a nerve segment taken from the healthy site of the patient) is inserted into the damaged location with connected ends. The autograft provides a similar extracellular matrix (ECM) environment. Still, additional surgery is necessary, and the most crucial fact is that the donor site loses its function, which leads to tissue morbidity [1].

Alternative tissue-engineering strategies have been investigated to avoid autografting and enhance axonal regeneration. The application of neurotrophic factors at the injured site and the neutralization of growth inhibitory molecules were tested. However, these strategies can promote disorganized axonal growth with a lack of linear movement and have no use for major damages. The development of neural scaffolds enhanced new strategies in tissue engineering. The neural scaffold is a guidance channel that bridges the injured site's gap and supports the growth of axons across a lesion toward the appropriate target with linear alignment [2].

The neural scaffold should direct axonal growth from the proximal to the distal nerve stump and possess the internal pores in the range of 5–30 μm (recommended 10–20 μm) to avoid infiltration of fibrous scar tissue while allows diffusion of the nutrients and waste products. The mechanical properties should be appropriate, with sufficient flexibility to provide structural support. The neural scaffold should have similar properties as native ECM, where cell adhesion and proliferation are enabled. Biocompatible materials should be used nontoxic to cells, with no immune response, and may even enhance cell behaviour for improved regeneration [2].

A promising technique for fabricating neural scaffolds with linearly oriented architecture is the freeze-casting method. The process is straightforward, inexpensive, and adaptive to fabricate bioceramic scaffolds with a controlled microstructure. It is based on the directional solidification of water solution, which leads to the creation of longitudinal channels. During freezing, the ice crystals are formed along the thermal gradient, and the suspension particles are concentrated between crystals. The ice phase is sublimed during the lyophilization process (freeze-drying) when the lamellar structure is formed, and the mechanical properties are improved with sintering. Various materials can be used as a powder in freeze-casting suspensions. Biocompatible materials provide unique properties, including bioactivity, biocompatibility, and biodegradability [2, 3].

This thesis is focused on the freeze-casting technique as a possible technique to produce linearly oriented scaffolds made from biocompatible materials, including calcium-phosphate materials, zirconia, and titania. The microstructure, mechanical, and biological properties are studied and compared.

2 LITERATURE REVIEW

2.1 Neural scaffolds – state of the art

Neural tissue repair and regeneration strategies are given great attention due to influencing a patient´s life quality. Several scientific methods have been developed aimed at nerve regeneration using conventional autologous neural grafts and newly developed therapeutic strategies to reconstruct damaged nerves. Neural tissue engineering is focused on synthetic scaffolds mainly, which are analogous to the natural extracellular matrix. The scaffolds provide an environment for the adhesion and proliferation of neural cells, biocompatible, biodegradable, and bioactive to support neural outgrowth.

2.1.1 Autologous neural graft

Neural grafts are the traditional technique to bridge the gap between two nerve ends. The destroyed part of the nerve is cut, removed, and replaces by the new nerve taken from the less binding site. Nerve grafts from a donor are ideal because autografts are not rejected. The sural nerve at the back of the leg is most used as a conduit. This type of regeneration is the gold standard for the reconstruction of limited peripheral nerve deficits. The reparation must be performed without tension because it causes fibrosis, which can cause regenerative failure. The graft should be long enough to avoid this problem.

A second surgery is often needed. The donor site loses its function by reduction of the length, and this leads to harmful changes such as scarring and the formation of painful neuromas. The golden standard cannot always be utilized in extensive injuries due to the shortage of donor tissue [4, 5].

2.1.2 Biologic neural scaffolds

Neural guides based on tissue from different biologic tissues have been used as an alternative method for neural reparation. It is possible to use tissue as arteries, veins, muscles, and other materials. A different biologic neural guide was a nerve conduit made from modified tissue with laminin and collagen. This type of neural guide has more disadvantages than advantages. It causes many tissue reactions, such as early fibrosis, scar infiltration, lack of mechanical properties. Nowadays, it is easier to achieve all requirements with synthetic neural guides despite problems with biocompatibility [4].

2.1.3 Synthetic neural scaffolds

Synthetic polymers can be either biodegradable or non-biodegradable. Poly (α-hydroxy acid) polymers (PLA, PGA, PLGA), polyesters of these acids are considered biodegradable, but hydrogels based on PEG, methacrylate are usually non-biodegradable. Some synthetic materials (PLLA, collagen) show piezoelectric properties – electrical charges generated under mechanical stimulation [6]. However, new better suit scaffolds were created, highly aqueous, soft, and share similarities and properties with natural nerve tissue [7]. Many methods are used to develop scaffolds with all requirements, such as electrospinning, freeze-casting, foam formation, etc.

Non-biodegradable synthetic neural scaffolds

Silicone was the primary material used as a nonabsorbable neural guide in the early 1980s. In a hollow tube, a fibrin matrix was formed between proximal and distal nerve ends. The fibrin matrix prerequisite for the nerve regeneration process consists of migration and proliferation of Schwann cells and axonal growth. This treatment was used in several studies for various nerves, and they reported partial recovery with that technique after four weeks. Mostly, nerves were recovered on the morphological level, but motor functions have rarely been achieved [4, 8].

PEG hydrogels are biodegradable, biocompatible, biochemically inert with hydrophilic properties, but also non-bioactive. Lampe et al. developed 3D hydrogel, which closely matched the stiffness of the native brain, and increased metabolic activity and proliferation [9]. Luo et al. reported PEG scaffolds as a promising method for accelerating and enhancing the membrane releasing process and improved mechanical compression [10]. Another non-biodegradable material was used as a hydrophilic sponge, concretely **pHEMA**. It provides supporting axonal regeneration. Hydrogels could be used as neural guides with mechanical properties similar to the spinal cord (200–600 kPa) [11].

Biodegradable synthetic neural scaffolds

Degradable, absorbable, and more body-like materials have been chiefly used after researches with silicone tubes. Polymeric materials, such as polyglycolic acid (PGA), polylactic acid (PLA), polycaprolactone (PCL), or polyhydroxy butyrate, are currently of great interest to nerve regenerations. PLA scaffolds showed good biocompatibility with a function as potential stem cell carriers. On the other side, it was observed that PCL has poor biocompatibility and create massive foreign body reaction. PCL guides are commercially available despite the negatives. However, they are less attractive, and present studies focus on PLA-scaffolds only. PLA supports Schwann cell proliferation, allows elongation of axons and vascular overgrowth [12].

The topography of a porous scaffold is suitable to provide cell adhesion, proliferation and it plays a role as topical guidance. It is possible to prepare scaffolds with the appropriate 3D structure according to the shape of the injured area. All three polymers do not undergo chemical modification in the body, and their degradation is by bulk rather than by surface, which is the ideal degradation process [4, 8].

For comparison, the regeneration of axonal length was minor in the PLA neural guide than in the autologous graft. The porosity and structure of the scaffold increased the surface area and regenerated axons extended in different directions. The structure allowed the infiltration of Schwann cells, and it provided a natural environment and supporting system for regeneration. However, scaffolds smaller than 10 mm were used in this study. In larger injured areas, the deficiency of regeneration time will be negligible since the gold standard will not be possible to use [8].

PLGA copolymer was studied for its permeability, swelling, deformation, and degradation rate controlled by the ratio of PLA:PGA. PLGA scaffolds showed a synergistic effect on neuronal regeneration. They effectively transported therapeutic agents to deliver anti-tumor drugs or glial neurotrophic factors to treat Parkinson´s disease [13, 14].

Biodegradable neural scaffold made of natural materials

Collagen is a widely used biomaterial for its biocompatibility, biodegradability, and availability. It is the most distributed class of proteins in the human body, and it finds enforcement in a wide range of tissue engineering [15]. Natural collagen is used for the regeneration of various tissues, organs, and peripheral nervous systems. According to Archibald et al., a collagen-based neural guide is physiologically similar to a neural graft, and it found an application for more significant gaps [16]. Neural collagen scaffolds are primarily used in hydrogel form or linear crosslinked scaffolds with laminin [17]. Collagen is the only biopolymer commercially available for nerve tissue engineering under the names NeuraGen® or Neuromaix® [18, 19].

Gelatin is a denatured protein obtained by collagen hydrolysis. Electrospinning allows a combination of gelatin with other natural and synthetic polymers to improve the nanofibers' mechanical, biological, and kinetic properties, which are critical components of a safe scaffold [19]. Nanofibrous gelatin conduits allow the differentiation of neuron cells. Gelatin is usually combined with PCL, which supports neurite outgrowth and Schwann cell proliferation. The second most used combination of gelatin is with PLA, where the neuron differentiation and promotion of neurite outgrowth are supported [20]. PLA can be used as a nanoparticle coat for the gelatin scaffold, which increases the viability of the nerve cells *in vitro* and *in vivo* [21].

Hyaluronic acid has widespread success in neural tissue engineering due to supporting neurite outgrowth, differentiation, and proliferation on different substrates [22]. Hydrogels are the most used neural scaffolds for suitable mechanical properties and biological properties, opening new therapies for neurodegenerative diseases [23]. Hyaluronic acid was combined with several biomaterials, including collagen, gelatin, chitosan [24].

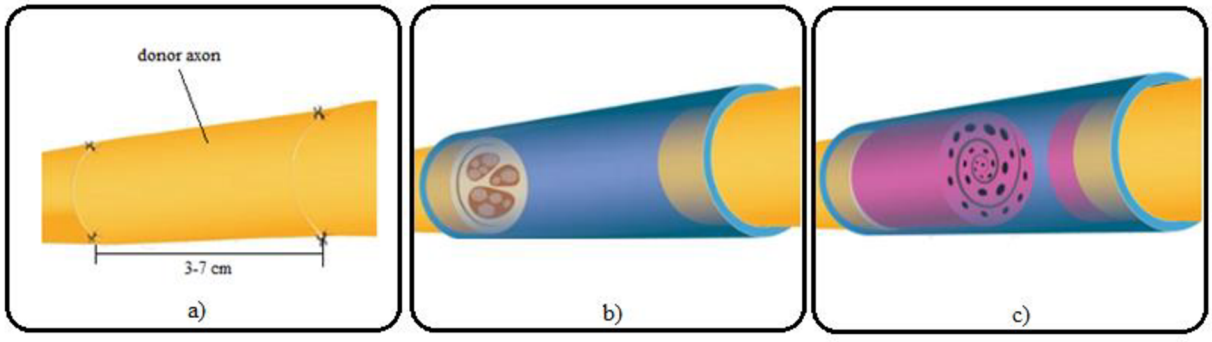

Figure 1: *Comparison of neural guides: a) neural graft; b) non-biodegradable synthetic nerve silicone tube; c) biodegradable neural scaffold made from PLA and PCL [8].*

Chitosan and chitin are other very used biomaterials that show biocompatible character. Chitosan is used in combination with alginate very often. Chitosan is a cationic copolymer composed of N-acetyl-D-glucosamine and D-glucosamine units, and alginate is an anionic polysaccharide composed of α-L-glucuronic acid and β-D-mannuronic acid. In aqueous solutions, two opposite charged polysaccharides interact to form polyelectrolyte complexes. The complexes can be used for the delivery of neurotrophic factors. It is possible to prepare a chitosan-alginate scaffold by freeze casting method with highly aligned, porous structure and longitudinal channels [2]. Chitosan hydrogels exhibited cell adhesion, interaction, survival, and outgrowth [25]. 3D printing was used in the study Gu et al., where a combination of chitosan, alginate, and agarose was used to form a bioink. After printing, 25 % of cells died, but proliferation continued, and after three weeks, the signs of mature neurons were present [26].

Ceramic and carbon materials

Carbon-based nanomaterials obtain electrical, mechanical, and biological properties for neural tissue engineering. Graphen biocompatibility was studied *in vitro* with PC12, BV2, and NSCs cells and *in vivo* in rats and mice as an electrode [27, 28, 29, 30]. Graphene is an allotrope of carbon formed from carbon atoms stored in a single layer arranged in a 2-dimensional hexagonal lattice. Graphen materials reported heat and electrical conductivity, and they are bactericidal and antiviral with low cytotoxicity. 3D graphene foam scaffolds were used to accelerate the differentiation and proliferation of human neural stem cells [31].

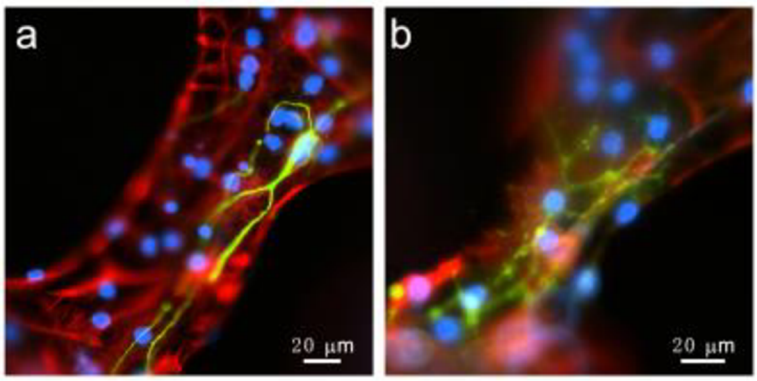

Figure 2: *The differentiation of NSCs on a 3D-graphene scaffold [31].*

For long-term neurite outgrowth (brain injury, spinal injury), the carbon nanotubes (CNTs) were developed with a cylindrical structure. CNTs showed mechanical and electrical properties, biocompatibility, and non-biodegradability. Carbon nanotubes could be organized in single-walled (SWCNTs) or multi-walled (MWCNTs) nanotubes. SWCNTs are used as substrates that modulate and stimulate neural cells. On the other hand, MWCNTs are applied in 3D technologies due to their remarkable stability applicable for scaffolds and drug delivery systems [24, 32].

Silica-charged nanoparticles agglomerate in biological solutions and settle on the cell surface. Particles larger than 50 nm cannot be easily penetrated inside the biological barriers by simple diffusion, so they agglomerate on the surface of the cell membrane. SiO_2 nanoparticles can be used for fluorescent marking in biomedical applications [33].

CeO_2 and SiO_2 nanoparticles were investigated *ex vivo* on frog sciatic nerve fibers. Kosmidis et al. showed CeO_2 had no neurotoxic effect even after long hours of exposure and helped nerve growth by 0.45–0.58 mm/h [34].

ZnO nanostructures have multifunctional properties, including semiconducting, catalytic, and piezoelectric properties. Several studies have highlighted that ZnO promotes the growth, proliferation, and differentiation of several cell lines, including nerve cells. ZnO nanostructures morphologies show high diversity (dots, nanotubes, nanowires, nanobelts, nanocombs, nanoflowers). The *in vivo* study was performed with PC12 cells, modeling neuronal cells. PC12 cells exhibited a well-developed neurite network, with neurite approaching 100 µm in length [35].

2.1.4 A superstructure of neural scaffolds

A superstructure is an internal arrangement for tissue simulation with tissue-like topography. Multiple paths can create a superstructure, including using hydrogels to stimuli the natural environment or freeze-casting to create longitudinal channels or fibers [4, 36].

Longitudinally oriented guides

Longitudinally oriented channels are usually made by adding macroscopic structure, needle, wire, or second polymer, inside the guide and then is removed. Usually, multiple macroscopic structures are added. It forms well-defined microtubular channel architecture, which helps to format regenerating axons straight along the scaffold. The axons grow through longitudinal channels like they usually grow through endoneurial tubes of peripheral nerves [36].

Fiber templating is another possible preparation method for creating longitudinally oriented channels involving the solubilization of embedded PCL fibers dispersed in gels. PCL was removed in the sonification process for 75 minutes, resulting in the complete dissolution of the PCL fibers in the solvent [11].

One of the principal methods is the freeze-casting technique that improves physicomechanical features, controlling pore size according to cell size. The scaffold is designed to guide cellular proliferation and differentiation, and it is expected that it has suitable morphology for neural regeneration [37].

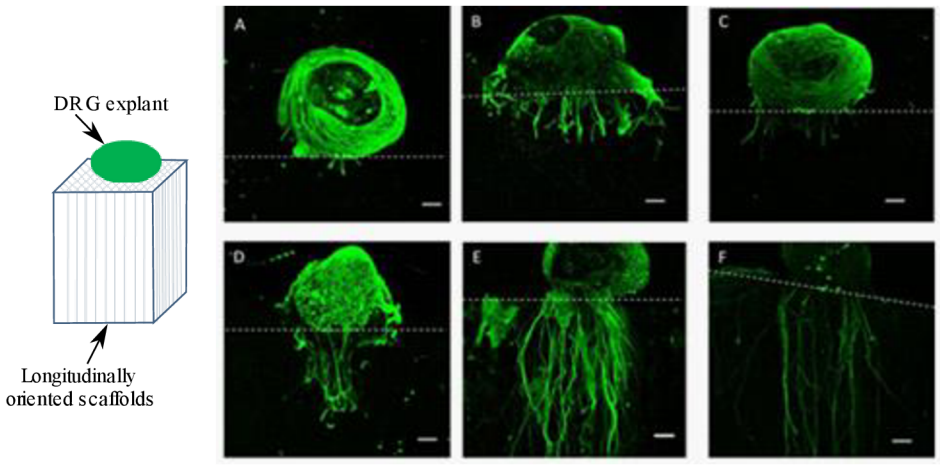

Figure 3: *Dorsal root ganglion (DRG) growth in longitudinally oriented scaffold; 100 µm scale bar [2].*

The freeze-casting method was used in several studies for the creation of a guidance scaffold. Collagen scaffold supported excellent glial cell attachment, proliferation, and oriented migration, as well as direct axonal growth. The directionality of the cell´s growth was somewhat random and poorly oriented. However, the cultivation with Schwann cells was entirely successful after four weeks. It was shown that the small diameter of pores (2–20 μm) promoted better orientation of cells, but pore size also influenced other parameters such as cell attachment and viability [38]. Stokols et al. prepared a linearly oriented neural guidance scaffold for spinal cord injury by freeze-drying method from agarose. The hydrated scaffolds were soft and flexible and contained extending pores throughout the whole length. The pore diameters were over 100 μm [39].

Longitudinally oriented fibers

Longitudinally oriented fibers can be added to a conduit along with channels to provide regenerating axons with guidance for longitudinally direct growth. The size of the fibers is about 500 μm. By adding fibers, the waste and nutrients can be exchanged better, and it has superior repair performance over nonpermeable scaffolds. Conductive and nonconductive fibers based on carbon and tungsten can be used. Studies showed that there is no difference between them in supporting axonal growth. Compared to non-fiber scaffolds, the neurite extension increased significantly [4].

The microfiber guidance characteristics from PLLA were added to extend the surface area of the hollow PLA tube. A wet-spinning process fabricated PLLA microfilaments. No matter what the gap length was, the microfiber improved cell migration and axonal regeneration and provided myelination during nerve repair. It enhanced endogenous repair by organizing the extracellular matrix, revascularization, and Schwann cell migration. The microfibers created an environment for the initiation substrate for Schwann cell migration out of the nerve stumps while preventing myofibroblasts from subdividing the nerve stump [4, 40].

2.2 Bioceramic materials

Nowadays, bioceramic has become a diverse class of biomaterials, including bioinert ceramic with high strength. Bioactive ceramic is mainly used for bone tissue which forms direct chemical bonds. Bioresorbable ceramic actively participates in the metabolic processes of an organism. Bioinert ceramics are alumina, zirconia, and titania, bioactive are bioglass and glass, and calcium phosphate is categorized as bioresorbable.

The application of bioceramic is very diverse. Bioceramic is most used in orthopedics to reconstruct arthritic or fractured joints (hip, knee, shoulder), repairing fractures or damaged parts of the bone, or replacing diseased, damaged, or loosened teeth. The medical community accepted bioceramic as a possible way to treat damaged parts of the body for its unique biocompatibility (without cytotoxicity), bioactivity (support cell adhesion and proliferation, vascularization), and bioresorption [41].

Alumina (Al_2O_3)

The first bioceramic widely used in medicine was alumina (α-Al_2O_3). Alumina shows excellent properties, such as corrosion resistance, good biocompatibility, high wear resistance, and high strength, so it is mainly used in load-bearing hip prostheses and dental implants [42].

Alumina ceramic is bioinert material with high abrasion resistance and hardness due to the surface energy and smoothness. Al_2O_3 has one stable phase, a hexagonal structure with aluminum ions at the octahedral interstitial sites. A minimal amount of magnesia is added (<0.5 %) to limit grain growth during sintering [43]. With an increase of the grain size to >7 μm, the mechanical properties can decrease by 20 %. However, unique tribiologic properties occur if the grains are tiny (<4 μm). It is biocompatible material because implants showed no signs of rejection or prolapse after weeks. After four weeks, the fibroblast proliferation and vascularization started [41, 44]. Lemons et al. reviewed other alumina implants, including knee prostheses, bone screws, alveolar ridge, ossicular bone substitutes (middle ear), keratoprostheses, segmental bone replacements, blade and screw, and post-type implants [45].

Zirconia (ZrO_2)

Zirconia, the metal dioxide, is a bioinert ceramic material with high mechanical properties and fracture toughness. The biomedical application of zirconia is to manufacture ball heads for total hip replacement, and it is used in dentistry for crowns, bridges, and implant abutments for several years [46]. Tetragonal zirconia polycrystals (TZP), partially stabilized zirconia (PSZ), and fully stabilized zirconia (FSZ) are the main types of zirconia used in clinical dentistry for their chemical identity with slightly different physical properties (porosity, density, purity, and strength). The most commonly used zirconia in dentistry and orthopedics are yttrium cation-doped tetragonal zirconia polycrystals and magnesium cation-doped partially stabilized zirconia [47]. Roy et al. showed that magnesium-stabilized zirconia removed from femoral heads did not show aging after five years from implantation [48].

Pure zirconia is allotropic which possesses different crystallographic phases (monoclinic, tetragon, and cubic) due to atomic arrangement. The temperature determines the different phases. The monoclinic phase is stable at temperatures up to 1170 °C, the tetragonal is stable between 1170–2370 °C with superior mechanical properties, and above 2370 °C, the cubic phase is stable [49].

Zirconia is considered a biocompatible material, and no cytotoxic effect for zirconia ceramic was observed in several cell types when tested both *in vitro* and *in vivo* [50, 51]. The excellent adhesion and spreading properties were shown with human osteoblast. The cells preserved their capacity to proliferate and differentiate. Biocompatibility of zirconia is often attributed to good hydrophilicity and protein adsorption (e.g., albumin, the cell adhesion-inhibiting protein, is adsorbed more quickly than fibronectin, a cell-adhesive protein) [52].

Another critical parameter of zirconia ceramic is the formation of a bacteriostatic biofilm on its surface. It has been demonstrated that zirconia accumulates fewer bacteria *in vivo* than titanium. Bacterial accumulation causes extensive bone loss around implanted biomaterial [53].

Titania (TiO_2)

Titania or titanium dioxide is bioinert and safe material with many applications, also studied as a "natural" material. Titania has gained widespread attention due to its properties, relatively low price, and processing. Furthermore, TiO_2 is approved by Food and Drug Administration (FDA) in the application for dental paste, oral capsules, suspensions, tablets, dermal preparations, and non-parenteral medicines [54].

Crystalline titania occurs naturally in three polymorphs – anatase, rutile, and brookite. Brookite is the most stable polymorph. It is semiconducting material that exhibits photocatalytic activity in the presence of light with an energy equal to or higher than its band-gap energy. A 230 nm particle size powder scatters visible light, with 60 nm particle size scatters UV light and reflects visible light. Under UV, titania exhibits photocatalytic activity, which is more present in anatase polymorph [54]. The antibacterial activity could be attributed to its photocatalytic activity, where the titania could culminate in the production of reactive oxygen species which are toxic to bacteria [55]. However, studies showed DNA damage and considerable toxicity with human cells caused by titania [56].

Titania and its alloys were used successfully in orthopedic and dental implants due to their excellent mechanical properties, corrosion resistance, and biocompatibility. Porous structures can facilitate cellular activities, such as the migration and proliferation of osteoblasts and mesenchymal cells, transport nutrients, and support vascularisation [57].

Bioactive glasses and glass-ceramics

Bonding to the bone showed some glasses, ceramics, glass-ceramics, and composites, classified as bioactive ceramics. A more specialized composition of bioactive ceramics can bond to the soft tissue. Bioactive glasses and ceramics showed the surface formation of a biologically active hydroxycarbonate apatite (HCA) layer, which provides the bonding interface with tissues. The HCA layer is chemically and structurally equivalent to a mineral phase in the bone. The bioactive glass contains two main crystal phases: mica and apatite. The apatite phase is a calcium phosphate layer with apatite crystals grown between bone tissue and ceramic material. All types of bioglass are structurally made from silica blocks. Bioglass is a bioactive material, especially osteoconductive [41].

Bonding to the bone was first demonstrated with the composition of bioactive glasses consisted of SiO_2, Na_2O, CaO, and P_2O_5, referred to 45S5 Bioglass® (signifying 45 wt.% SiO_2, S as the network former, and a 5 to 1 molar ratio of Ca as CaO to P as P_2O_5). Glasses with lower molar ratios Ca to P do not bond to the bone. 45S5.4F Bioglass®, or KGS Ceravital®. The highly reactive surface can be achieved with less than 60 mol.% SiO_2, high-Na_2O, and high-CaO content, or high-CaO/P_2O_5 ratio [58].

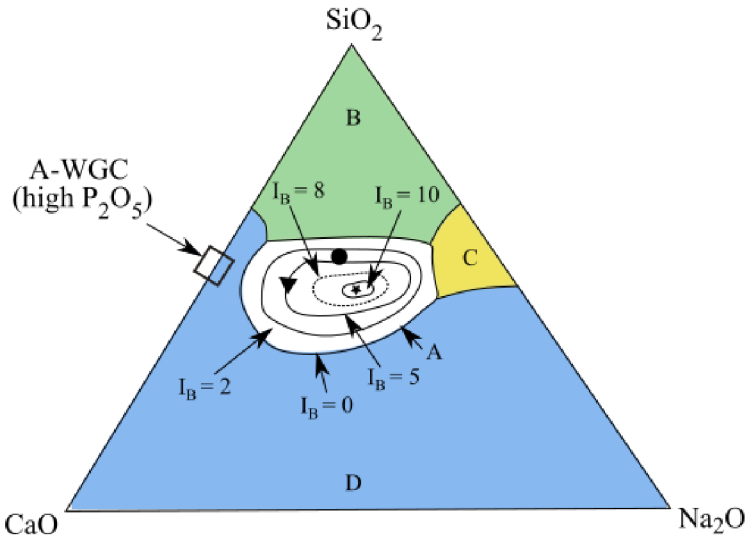

Figure 4: *Diagram of compositional dependence of bioactive glasses and glass-ceramics in bone bonding and soft-tissue bonding; ★ refers to 45S5 Bioglass®, ▽ refers to Cerevital ®, and ○ refers to 55S4.3 Bioglass® [58].*

In Figure 4, the compositional Na_2O-CaO-P_2O_5-SiO_2 dependence (in weight percent) of bone-bonding and soft-tissue is shown. All glasses contain 6 wt.% of P_2O_5. Region A (in the middle of the diagram) forms a bond with a bone, termed a bioactive bone-bonding boundary. Silica glasses without region B are not bioactive. Due to slow reactions, they behave as inert material. Glasses within region C are resorbable and disappear 10 to 30 days after implantation. Glasses within region D are not technically practical, and therefore they have not been tested as implants yet [58].

Calcium phosphate ceramics

Calcium phosphate ceramics (CPCs) are a class of elastic bioactive materials, which have been widely used for bone tissue repair. The surface of CPCs supports osteoblast adhesion and proliferation (osteoconduction) and stimulates new bone formation (osteoinduction). However, not all types of CPCs obtain the same biological reactions, most are osteoconductive, but certain types are osteoinductive. Surface chemistry and charge can also influence protein adsorption, which promotes differentiation via cell-extracellular matrix interactions. Accordingly, surface roughness can also aid cell differentiation by influencing cell adhesion [59].

The osteoinductive capacities differences of CPCs are mostly linked to the differences in properties, including solubility, crystallinity, and stoichiometry (e.g., the ratio of calcium to phosphate). The CPCs group consists of hydroxyapatite (HAP), tricalcium phosphates (TCP), amorphous calcium phosphates (nano-crystalline calcium phosphate, ACP), biphasic calcium phosphates (BCP), and whitlockite (WH). The difference between CPCs in osteoinductivity is shown in table 1 [59, 60, 61, 62].

The porosity of calcium phosphates also influences bioactivity. The increase in porosity improves contact with body fluids on the surface area. The presence of pores in the range of 20–500 µm affects protein adsorption [63].

Table 1: *Summary of CPCs properties, which influence osteoblastic differentiation [59, 60, 61, 62].*

CPC	Solubility (~K_{sp})	Ca/P ratio	Osteoinductivity
HAP	Poor (10^{-58})	1.67	+
TCP	Fair (10^{-25}–10^{-29})	1.5	++
ACP	Hight (10^{-23}–10^{-25})	1.15–1.67	+++
BCP	Variable (TCP/HAP ratio)	1.5–1.67	++++
WH	Poor (10^{-113})	1.43	+/++

Hydroxyapatite is a widely used calcium phosphate material due to the closest composition to bone mineral. It is a naturally occurring form of calcium phosphates of inorganic components in human bones. Despite it, various ions and vacancies form defective structures. Stoichiometric structures can have both monoclinic and hexagonal phases, but hexagonal is a more stable structure. Therefore it is more used in clinical research. It is osteoconductive material but with poor osteoinduction. These properties can be tuned via ionic substitutions. Anionic substitution of carbonate to phosphate increases solubility and bioactivity. Ions as fluoride, chloride also increase osteoinductivity. HAP is one of the most stable CPCs, but with poor solubility in a physiological environment defined by temperature, pH, body fluids, etc. [64]. The surface of HAP can provide nucleating sites for precipitation of apatite crystals in the culture medium, typically saturated with calcium and phosphate ions. HAP does not cause inflammatory reactions after applications to the body [59, 65].

Tricalcium phosphate occurs in two phases, α and β, which possess identical chemistry but different crystal structures. α-TCP has the crystal structure of the monoclinic space group, whereas this phase is formed at 1125 °C or higher. β-TCP shows the crystal structure of a rhombohedral space group with a temperature of phase transformation at 900–1100 °C. Both phases are less stable and more soluble in an aqueous environment than HAP. β-TCP is examined to be both osteoconductive and osteoinductive with low interfacial energy, which invokes the precipitation of an apatite layer in aqueous solutions [66]. Besides, it has a high resorption rate and is used for increasing HAP biocompatibility. These properties are caused by excellent biomineralization and cell adhesion by the nanoporous structure [63].

Biphasic or multiphasic materials were developed to utilize the properties of TCP and HAP simultaneously. These phases can coexist in a form because each component is homogenously mixed at the submicron level. The biphasic calcium phosphates combine two incompatible calcium phosphates – HAP, which is more stable and more soluble than TCP. The combination provides higher bioactivity, bioresorption, and osteoinductivity. The mixture stimulates the osteogenetic differentiation in mesenchymal stem cells, increases cell adhesion, attaches growth factors, and enhances mechanical properties. The biphasic calcium phosphate scaffolds became attractive due to the mentioned characteristics [63].

A lack of long-range order characterizes **amorphous calcium phosphate** materials. ACPs are produced by the rapid precipitation of calcium and phosphate ions in aqueous solutions. The impurities (Na^+, K^+, Mg^{2+}, Cl^-, etc.) are present. The stoichiometry is not well-defined. The Ca/P ratios are usually between 1.15–1.67, depending on conditions as pH. They obtain properties of releasing calcium, phosphate, and other ions, which causes their osteoinductivity [67]. However, the rapid release of ions can cause perturbations in the local pH and negatively affect cell proliferation and viability in the long term. The Zn and ZrO incorporation delay dissolution rates [59].

Whitlockite is calcium phosphate ceramic with magnesium ion-containing. It is the second most represented mineral in human bone with a rhombohedral space group. WH has a negatively charged surface and high stability at acidic conditions. It has been reported that WH is formed when Mg ions are present in acidic solutions containing calcium phosphate. WH's mechanical strength is higher than HAP, and the solubility is higher in physiological conditions with continuous ions release. The constant release of magnesium and phosphate ions promotes bone growth by controlling osteogenic differentiation, especially magnesium ions [63].

2.3 Freeze-casting

Freeze-casting, also known as ice-templating, is a simple, inexpensive process to produce ceramic or polymeric versatile porous complex. The concept of the process is to obtain porosity by forming solvent crystals by freezing the suspension. Afterward, the crystals (most commonly water crystals) are removed by sublimation of solvent in the freeze-drying process. The freeze-drying process is under vacuum, avoiding the shrinking and drying stress, which causes cracks and warping. After sublimating, the green body is sintered to remove solvent from micropores, and the scaffold achieves the final dimension with improved strength, stiffness, and required porosity. Freeze-casting can fabricate well-defined directional microstructures with open and interconnected pores [68, 69]. The whole process is shown in figure 5.

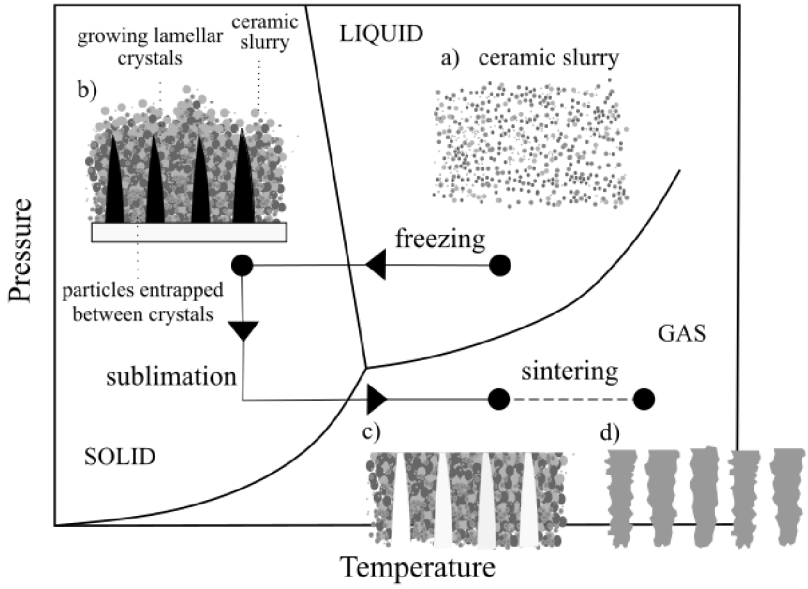

Figure 5: *Schematic diagram of the freeze-casting process [3].*

Freeze-casting is a widely used method for bio-related applications. In recent years, it is used mainly in tissue engineering for bone and tooth tissue applications. The low-temperature process allows us to use scaffold as a drug delivery system due to designable microstructure, promoting the gradual release of a drug. Freeze-casted materials are also excellent insulators, gas distributors, and separation filters with good absorption ability [69].

2.3.1 Starting powders

Freeze-casting is a physical process where all materials and composites, including polymer solutions, metal or ceramic suspensions, can be used. The freeze-casting gained high popularity for using biomaterials, which are primarily biocompatible, bioactive, and the liquid carriers (mostly water) are biocompatible too. The suitable combination of biomaterial with liquid makes it possible to control pore size, porosity, and pore geometry according to the desired location [69].

A great range of biomaterials compatible with the freeze-casting method exists: collagen, mainly used for repairing nerve tissue; calcium phosphate (hydroxyapatite, tricalcium phosphate, and a composite of the two) is used as a bone substitution in low to medium applications [70].

The freeze-casting method can also be applied where pores are not required. The pores are filled with a second phase (polymer, ceramic, or metal). The final scaffold is like the biological counterpart and has a higher toughness than the constituent [69].

The resulting scaffold is most affected by the properties of the ceramic powder. The freeze-casting process is based on the interactions between particles, including solidification. The particles' size, distribution, shape, surface tension, and roughness can be modified for the specific application. The solidification kinetics is connected chiefly with particle size [3].

Ceramic slurries are commonly composed of micro/submicrometre-sized particles dispersed in a water solution with binder and dispersant. Dispersants reduce particle aggregation and flocculation [69].

2.3.2 Solvents

The frozen solvent has a role as a binder to hold the part together for demolishing. On the other hand, the porosity of the sintered scaffold is a copy of the formed crystals developed during the freezing process. For this reason, the solvent is an essential component of the suspension. It defines the final micro and macroporosity and desired structure of the scaffold [3].

Water solvents are most used, but a wide range of solvents can be used. Other used solvents are camphene, silica sol, tert-butyl alcohol (TBA), dioxane, naphthalene, carbon dioxide, and terpene. The various solvents must be used because of increasing requirements, such as solidification temperature, viscosity, vapor pressure, volume change during freezing, environmental issues, and price. For example, freezing liquid carbon dioxide (CO_2) causes a dendritic structure, similar to camphene [3, 69].

Aqueous system

Water is environmentally friendly, suspension can be prepared at room temperature, and it works well with many materials as alumina, titanium dioxide, silica, and hydroxyapatite. The additives are added to modify water parameters: to adjust the freezing point, ice expansion, to change viscosity, and to change pore structure. They can also modify the solvent phase diagram, the interparticle forces, and the undercooling. It is possible to achieve the anisotropic crystals with a homogenous microstructure by uniform freezing. If the temperature gradient is controlled, the anisotropic crystal growth is preferable due to the chemical potential difference. The directional freezing results from lamellar, dendritic, parallel, columnar, or aligned pore systems [69].

Glycerol, polyacrylic acid (PAA), gelatin, silica, and clay are most used as water additives. Glycerol has a low freezing point and a low vapor pressure, improving homogeneity, and is non-toxic, soluble in water, and inexpensive. It plays a role as a lubricant between suspension particles. The result of adding glycerol is a localized amorphous ice structure, and a reduction in crystal size reduces the water expansion and modifies water viscosity. Glycerol can be used in combination with PAA and ammonium polymethacrylate. The suspension is more mesh-like with added PAA [69].

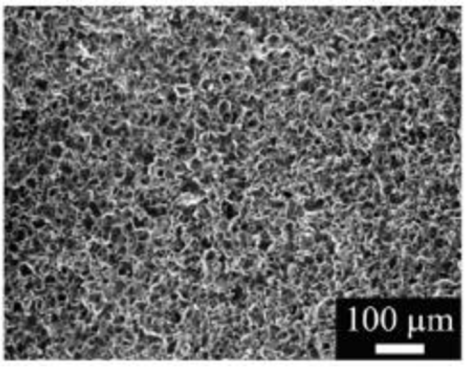

Figure 6: *The mesh-like microstructure in the alumina system with added glycerol [69].*

Gelatin with hydroxyapatite suspension adjusts microstructure and porosity. The HAP particles are slowly gelatinized during freezing, and they hinder the anisotropic growth. It forms a reticulated structure, the 3D network. The HAP suspension without gelatin has only a lamellar structure, as Figure 7 shows. Silica is additive in HAP suspension also. Phase transformation of the HAP to β-tricalcium phosphate is initialized by adding silica. It reduces shrinkage and increasing porosity [69].

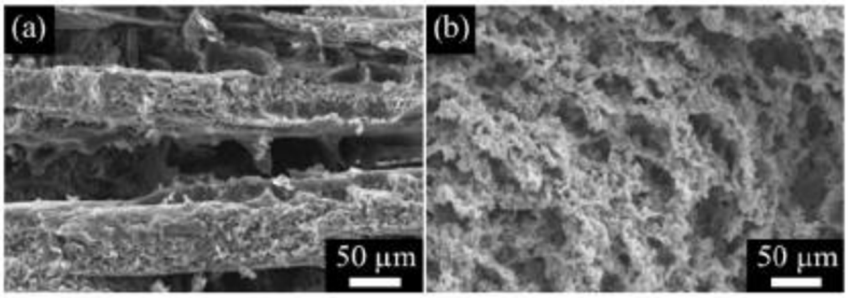

Figure 7: *Gelatin effect in hydroxyapatite system; a) lamellar system without gelatin, b) reticulated shape with added gelatin [69].*

Non-aqueous system

Camphene, naphthalene, and TBA are other chemicals used as dispersing mediums. Unlike water, they have different freezing temperatures, viscosities, volume changes, and vapor pressures during sublimation. Camphene is a popular non-aqueous system for its non-toxicity and environmental friendliness. This chemical makes it possible to freeze at room temperature because the melting point is 44–48 °C [69].

Polystyrene (PS) is the only additive used with camphene. PS acts as a binder in suspension, prevents the suspension from cracking in the walls. During the freezing, the PS interacts with HA particles and separates them from camphene, improving strength. The presence of PS increases the probability of the dendrites, so the pore sizes are decreased. The behaviour of camphene is not understood as the water properties are [69].

2.3.3 Suspension

Sedimentation

The sample without a structural gradient is possible to prepare by the precise control of the particle sedimentation. The sedimentation is depended on the density and size distribution of the particles and the viscosity of the liquid. The spherical particle is affected in liquid by two forces: gravitational acceleration and opposing force. This force F is equal to the weight of the volume of the fluid that it displaced:

$$F = \left(m - \rho_L \cdot V\right) \cdot g = \left(\rho_P - \rho_L\right) \cdot g \cdot \frac{4}{3} \cdot \pi \cdot r^3 , \qquad (1)$$

where m is mass and r is the particle's radius, g is the gravitational acceleration, ρ_P and ρ_L are the density of particle and liquid.

If the density of the particle is different than the liquid, then the particle is affected by the resisting force, which depends on the dynamic viscosity η of the liquid, radius, and the velocity v_P of the particle,

$$F_f = 6 \cdot \pi \cdot r \cdot \eta \cdot v_P \qquad (2)$$

The velocity of the particle is expressed by joining equation (1) and (2):

$$v_p = \frac{2}{9} \cdot \frac{\left(\rho_P - \rho_L\right) \cdot g \cdot r^2}{\eta} . \qquad (3)$$

The minimalization of the sedimentation is required in this process. The density between particle and liquid needs to be minimized, and the viscosity should be increased quadratically with an increase in the particle diameter [70].

Particle size effect

The solid loadings with lower water content produce lower porosity and higher density due to less expansion of ice crystals in the sample. The suspension also affects homogeneity. The homogeneity disappears when the particle size is too similar to the solvent crystals.

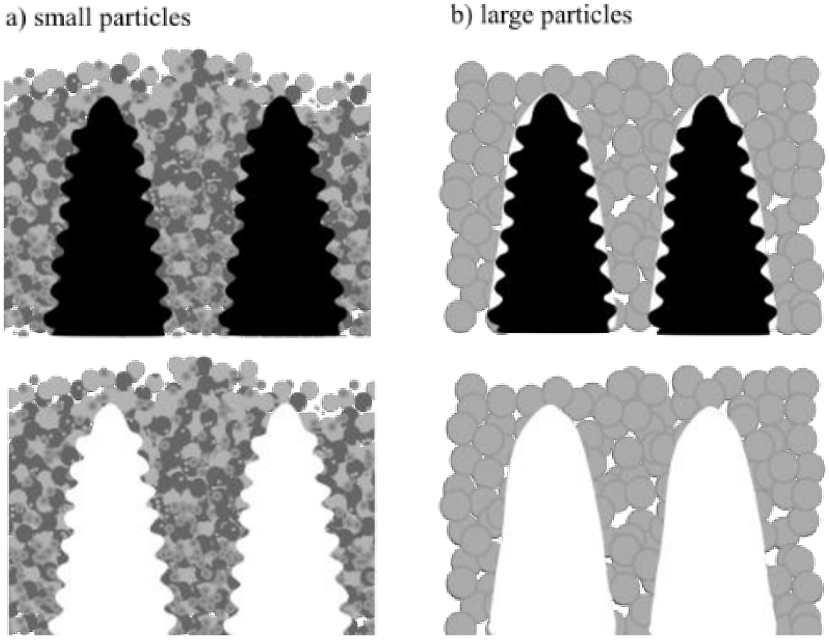

Figure 8: *Morphology of pores with different particle sizes [69].*

Morphological features are not well replicated, as is shown in figure 8. Small particles do not obstruct the solvent and allow natural ice-crystal growth. A "breakthrough" is a process where the solidification front rejects the particles, and the particle concentration is higher in melting areas. The solvent dendrites grow into the liquid and push ceramic particles into the interdendritic spaces. When the particle redistribution ends, the solid-liquid interface moves to the interdendritic space [3, 71].

2.3.4 Additives

Bioceramic scaffolds should have a structure at the micron and submicron levels comparable with natural materials. The thickness and separations between the ceramic layers, the roughness of ceramic walls, and bridges between lamellae play a crucial role due to their influence on mechanical stability [72].

Additives to control the structure

The microstructure can be manipulated by adding additives to the suspension. Additives control the microstructure of the growing ice crystals by changing the phase diagram of the solvent, the value and anisotropy of the solid/liquid and particle/liquid interfacial energies, the degree of under-cooling ahead of the fluid front, the viscosity of the solvent, or the forces between ceramic particles. The morphology and roughness of the ice crystals can be influenced by submicron levels [73].

Sodium chloride, carbohydrates including sucrose, glycerol, and ethanol, are well-known types of antifreeze. The viscosity of the suspension can be affected by gelatin, and citric acid, which influences pH, which manipulates interparticle forces [73].

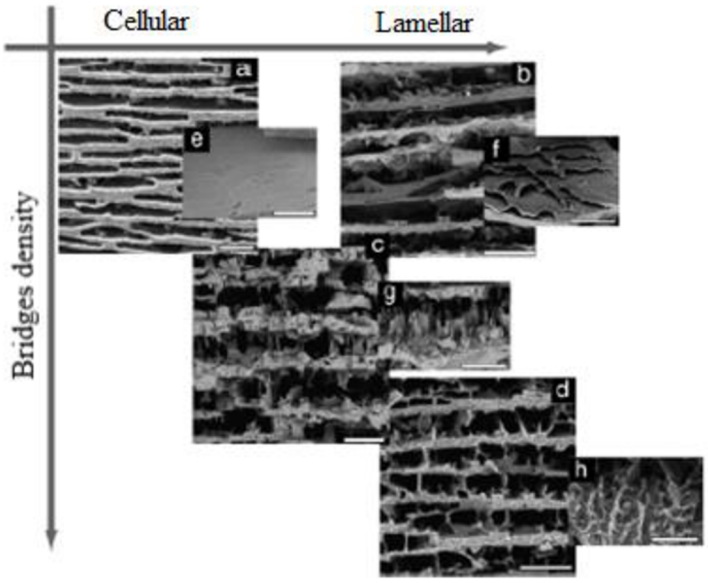

Figure 9: *Additives influence material architecture. The graph shows the difference of the structure by several additives (from lamellar to cellular structure and the roughness and density); a) 10 wt.% sucrose in citric water with pH = 2.5. b) 4 wt.% ethanol, c) 4 wt.% sodium chloride, d) 4 wt.% sucrose, e)–h): details of the surface roughness [73].*

Additives can dictate the final architecture of the scaffold, from lamellar (no additive, sucrose) to cellular (gelatin, glycerol, a combination of sucrose with citric acid), or bimodal pore width distribution (ethanol) with large pores under 100 µm. In figure 9, it is possible to see changes in microstructure by SEM micrographs. Sucrose with citric acid forms a cellular structure with smooth ceramic walls. Ethanol helps to form a lamellar structure with smooth roughness, sodium chloride forms a sharp-faceted lamellae surface, and sucrose promotes lamellar structure with microscopic roughness [73].

Additives to control lamellar bridges

The ceramic interlamellar bridges are another necessary microstructural feature due to mechanical response, preventing Euler buckling during compression and hindering crack propagation in the direction parallel to the lamellae. A particular bridge structure is formed by interfacial tension and interparticle forces affected by additives. For example, trehalose promotes a high density of thin bridges, and sucrose promotes a low density of wider bridges [73].

2.3.5 Freezing process

After the suspension with the required properties has been prepared, the air is removed from the suspension. The suspension is filled into a polymer mold (PLA, PTFE) and sealed by a copper bottom finger. The freezing of the copper finger on one side helps to create one-directional lamellas (Figure 10). It is possible to use two-sided freeze-casting systems, in which

the bottom and the mold are closed with a copper finger and are cooled, or to use the copper mold to achieve radial freezing [70, 74].

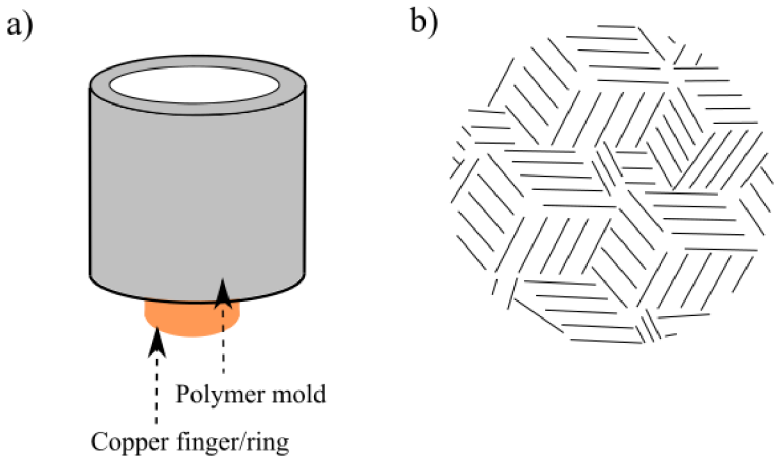

Figure 10: *Unidirectional freeze-casting; a) a cooled copper finger, b) achieved lamellar system[74].*

Freeze-casted sample – microstructure

The sample microstructure can be divided into three distinctive zones. Each of them can be characterized by different shapes and dimensions of the pores (Figure 11). The closest zone to the cooling is the initial zone (Zone 1), which is dense and with no porosity. Zone 2 obtains round pores, due to it is called a cellular zone. In upper Zone 3 (lamellar zone), the pores are linearly oriented and aligned in the direction of the ice front [68]. For neural tissue engineering, it is required to gain only lamellar zone to successful cell infiltration.

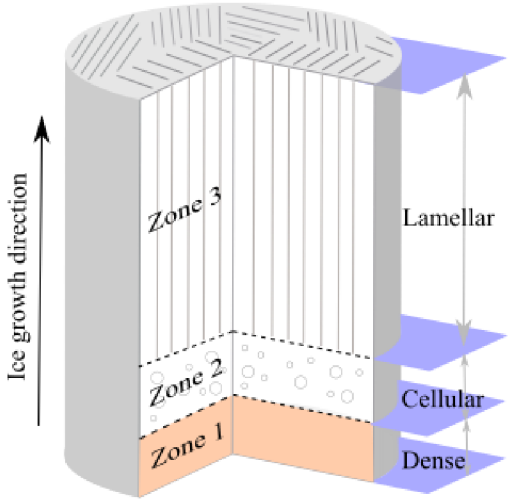

Figure 11: *Three distinctive freeze-casted scaffold zones [68].*

Solidification principles

The crystal morphology determines the resulting microstructure. The volume change is related to the phase transformation. Crystal nucleation and growth interactions between moving particles make solidification one of the essential points of the freeze-casting process.

Thermodynamically, the interfacial free energy between particles and front σ_{sp} should be larger than the sum of interfacial free energy of solid-liquid σ_{sl} and particle-liquid σ_{pl}

$$\Delta\sigma_0 = \sigma_{sp} - \left(\sigma_{sl} + \sigma_{pl}\right) > 0. \tag{4}$$

The thermodynamic criterion reflects the possibility of particle repulsion, where a liquid film is between the front, and the rejected particles and the transfer of the liquid molecules are available for growing crystals [69].

The rejection behaviour of the particles depends on the forces between particles, as repulsive force F_σ is shown in equation (5),

$$F_\sigma = 2 \cdot \pi \cdot R \cdot \Delta\sigma_0 \cdot \left(\frac{a_0}{d}\right)^n \tag{5}$$

and attractive force F_μ is shown in equation (6):

$$F_\mu = \frac{6 \cdot \pi \cdot \eta \cdot \nu \cdot R^2}{d}, \tag{6}$$

where R is particle radius, a_0 mentions average intermolecular distance, d is the distance between particle and ice front, n is the constant in the range from 1 to 4, v refers to the velocity of ice growth, and η is the viscosity of the suspension. The engulfment and repulsion of the particles can be predicted with these equations [69, 75].

The particle velocities have a serious impact on the freezing process. The velocities are affected by the particle's radius, density, dispersing medium, and temperature gradient. The critical velocity of the solidification front is expressed in the equation:

$$v_c = \frac{\rho_1}{9 \cdot \eta \cdot \rho_S} \cdot \left[-\frac{A}{2 \cdot \pi \cdot D \cdot d_0} - g \cdot D \cdot d_0 \cdot \left(\rho_P - \rho_L\right) \right], \tag{7}$$

D is the diameter of the particle, A is the Hamaker constant, d_0 refers to the minimal distance between the particle and freezing front, ρ_P is particle density, ρ_S and ρ_l is the density of the solid-liquid, and g is gravitational constant. The critical velocity is a crucial parameter because particle entrapment occurs when the solidification velocity is higher than the critical velocity.

All solidification principles above are for the aqueous systems; however, the fundamental principles can be applied to all freeze-casted systems with porous morphology [69, 76].

The nucleation and crystal growth of aqueous systems

The ice crystal has 15 crystalline phases, most commonly the hexagonal structure. The crystal structure and kinetics of crystal growth cause parallel growth to the *c* axis (Figure 12). The perpendicular growth is kinetically favorable, and it has a higher chemical potential than the growth on the *a*-axis [3, 69].

The formation of the lamellar process is possible due to the hexagonal structure. Direct growth is preferred in tissue engineering. This formation can be prepared by increasing the temperature gradient while lowering the particle hindrance. Homogenous freezing, where the sample is constantly cooling, gave rise to the formation of homogenous ice nucleation, which leads to lamellar pore architecture [3, 69].

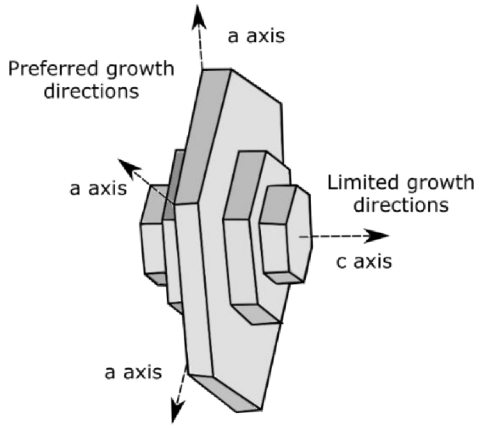

Figure 12: *Preferred hexagonal growth of water crystals [69].*

Freezing condition effect

Ice nucleation, crystal growth, and porous morphology are affected by freezing temperature, rate, and time. The aqueous and non-aqueous systems are affected differently by these factors. Most materials share the overall trend in microstructure evolution.

Freezing temperature affects ice nucleation and crystal growth. Supercooling is needed for ice nucleation. The nucleation rate is higher than crystal growth under high supercooling (from point O to B in Figure 13). Tiny crystals are formed, and the microstructure consists of small uniform pores. When the supercooling temperature is between points A to O, ice growth is favorable, and larger pores are formed.

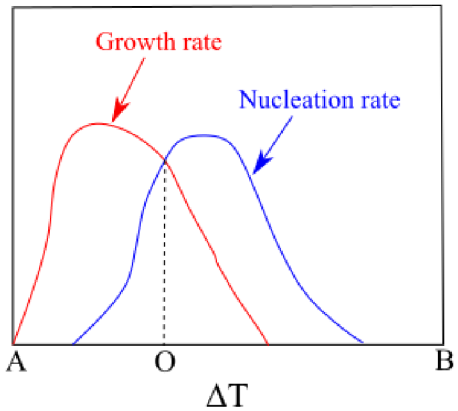

Figure 13: *How supercooling affects ice nucleation rate and growth rate. ΔT = Tm − T, where Tm is the freezing temperature, and T is the actual temperature [69].*

The freezing rate for the aqueous system is typically 0.05 °C/min. Ice nucleation is kinetically more favorable than crystal growth (small pore formation is likely) at a high freezing rate. The particles have less time to rearrange. A lower freezing rate offers lower porosity and densely packed nanoparticles. The freezing rate influences the heat transfer within the sample. When the temperature gradient is large, the ice crystals continuously grow and are interconnected or with dendritic microstructure [69].

Freezing time also has a significant impact on the resulting crystal growth. When a sample is maintained at a specific freezing temperature, ice crystals keep growing, and tiny crystals can link to each other and form large crystals. The long freezing time gives rise to columnar and lamellar microstructures [69].

2.3.6 Freeze drying

After the freezing process, the sample is carefully removed from the polymeric form and freeze-dried for 24–48 hours, depending on size. Freeze-drying or lyophilization is when the solvent from the sample is removed by sublimation, and the chemical stability is enhanced [70, 77]. The substances of most concern, peptides, proteins, organic molecules, undergo chemical reactions in water solution, which are often unacceptable for their safety. Freeze-drying can be used for stable pharmaceutical products (viruses, vaccines, peptides, liposomes, etc.). This process is divided into two steps, primary and secondary drying [78].

Primary drying step

Primary drying includes the sublimation of ice crystals. In the beginning, the heat is transferred from the shelf to the frozen solution and handled to the sublimation front. Next, the water vapor with ice sublimes is carried from the dried interior to the surface, and in the end, the vapor from the sample surface is transported to the chamber of the condenser, and vapor is condensed [77].

Secondary drying step

Secondary drying includes removing the water, which is not separate during the freezing process, and so did not sublimate off. The unfrozen water is usually adsorbed on the product's surface, or it is solute as hydrated water or dissolved in a solid. If this water is not removed, it will lead to faster product degradation [77].

2.3.7 Sintering

The sintering process is the last step of the freeze-casting process. Once the solvent has been removed, the green body can be sintered with the sintering technique. Usually, a low amount of the binder is used (organic substance), so the sintering process does not require a binder burnout process. The microporosity can be removed from the walls during this process, but macroporosity from the ice crystals is retained.

The porosity of the sintered materials is a replica of the original ice crystals (solvent crystals). Various porous structures can be gained, depending on the chosen solvent, slurries formulation, and solidification conditions [3].

3 AIMS OF THE THESIS

1. Literature review of neural scaffolds and a possible application of the freeze-casting method.
2. Preparation of calcium phosphate-based ceramic materials by freeze-casting with macro and microstructures suitable for neural scaffolds.
3. Analysis and evaluation of impact of the shaping method on microstructure, mechanical and biological properties.

4 MATERIALS AND METHODS

4.1 Materials

Neural bioceramic scaffolds were prepared using a freeze-casting technique with different freezing front velocity values and sintering temperatures, described in this part of the thesis. The commercially available hydroxyapatite, zirconia, and titania powders were used as the main component of water suspensions with several additives, including sugar, octanol, and dispersant

4.1.1 Freeze-casting suspension

The suspensions were prepared with solid loading 15 vol.%. The ceramic powders had particle diameters with a nanometer scale, only hydroxyapatite powder particles roughened after calcination treatment.

Table 2: *Properties of ceramic powders used for freeze-casting.*

Compound	Density ($g \cdot cm^{-3}$)	Purity (%)	Particle size (nm)
HAP	3.16	≥90.0	<200
ZrO_2 (TZ-8Y)	6.10	99.9	~40
TiO_2	3.89	99.9	~25

Hydroxyapatite suspension

Commercially available hydroxyapatite (HAP) powder (Sigma-Aldrich) was selected as a bioactive material. The HAP powder was treated by calcination at 800 °C per 1 hour in the air atmosphere before preparing the suspension itself. The calcination removes obtained carbonates, roughens the ceramic powder.

Table 3: *Composition of 15 vol.% HAP freeze-casting suspension.*

Compound	Weight (g)	Volume (cm^3)	Density ($g \cdot cm^{-3}$)	Mass fraction (wt.%)	Volume fraction (vol.%)
HAP powder	30.00	9.49	3.16	34.38	14.5
PVA	1.10	0.85	1.30	1.26	1.3
Water	51.50	51.50	1.00	59.0	78.8
Dolapix CE64	2.00	1.82	1.10	2.29	2.8
Octanol	0.06	0.07	0.83	0.07	0.1
Sugar	2.60	1.63	1.59	2.98	2.5

The water-based HAP suspension (solid loading 15 vol.%) was prepared with poly(vinyl alcohol) (PVA) solution (Mowiol® 10-98, M_w ~61.00, Sigma Aldrich) where PVA was an organic binder. The PVA solution was prepared by adding 9.61 g of PVA to 1000 ml of distilled water. Then it was dissolved in the water bath at 97 °C, 250 rpm. The required amount of PVA was weighed, zirconia milling balls, HAP, and several additives (sucrose, dispersant) were

added. The additives improve mechanical stability and control the micro-roughness of lamellae surfaces. A dispersant (Dolapix CE64) is used for a continuous distribution of ceramic particles. Sugar (sucrose) improves green-body mechanical stability by the formation of interlamellar bridges. Finally, the octanol was added to eliminate bubbles in the suspension and to decrease surface tension. The suspension was placed on a roller for 24 hours. The suspension composition is shown in table 3.

Zirconia suspension

Water-based suspension of zirconia was prepared from yttria-stabilized zirconia powder (TZ-8YSB, Tosoh). The solid loading of suspension was 15 %. The preparation process was the same as for HAP suspension, but Darvan C-N was used as a dispersant. The final composition of freeze-casting suspension with 15 vol.% of zirconia powder is shown in table 4.

Table 4: *Composition of 15 vol.% zirconia (8% yttria) freeze-casting suspension.*

Compound	Weight (g)	Volume (cm^3)	Density ($g \cdot cm^{-3}$)	Mass fraction (wt.%)	Volume fraction (vol.%)
Zirconia	60.00	9.84	6.10	50.76	14.8
PVA	1.10	0.85	1.30	0.93	1.3
Water	51.50	51.50	1.00	43.57	77.7
Darvan C-N	2.00	1.82	1.10	1.69	2.7
Octanol	0.06	0.07	0.83	0.05	0.1
Sugar	3.55	2.23	1.59	3.00	3.4

Titania suspension

Nanopowder of anatase (Titanium dioxide, Inframat® Advanced Materials™) with particle size 25 nm was used for water-based suspension. Darvan C-N was used as a dispersant. The final composition of titania suspension is shown in table 5.

Table 5: *Composition of 15 vol.% titania freeze-casting suspension.*

Compound	Weight (g)	Volume (cm^3)	Density ($g \cdot cm^{-3}$)	Mass fraction (wt.%)	Volume fraction (vol.%)
Titania	40.00	9.46	4.23	40.96	14.4
PVA	1.10	0.85	1.30	1.13	1.3
Water	51.50	51.50	1.00	52.73	78.5
Darvan C-N	2.00	1.82	1.10	2.05	2.8
Octanol	0.06	0.07	0.83	0.06	0.1
Sugar	3.00	1.89	1.59	3.07	2.9

4.2 Processing

4.2.1 Freeze-casting

Two different freeze-casting methods were chosen to achieve different lamellae sizes in HAP scaffolds by changing the front velocity. To obtain larger lamellae sizes, the cooling plate was chosen with a controlled temperature gradient. The smaller sizes were achieved with very fast freezing in a nitrogen bath.

Freeze-casting with the controlled temperature gradient

The controlled temperature gradient was achieved by the preset program in the cooling plate (Medite). The temperature was changed every 20 minutes by 5 °C from the initial −5 °C to the final −35 °C. This cooling rate enables lamellae formation in the whole volume of all samples. First, the cooling plate was pre-cooled at −5 °C. The PLA form with a copper ring was folded, 18 PVC tubes were inserted into the form. The HAP suspension was vacuated to remove air bubbles. The PLA form was situated at the plate for about 5 minutes, and the HAP suspension was slowly injected into every tube to avoid bubbles. The set program was started, and the cooling went by itself without intervention. The process of freezing took about two and a half hours. After proper freezing, the form with frozen suspension was disassembled. The frozen rods were placed on the alumina plate, and the samples were inserted into the freezer before the freeze-drying process. The apparatus is shown in figure 14.

Figure 14: *Freeze-casting apparatus.*

Freeze-casting with liquid nitrogen

Method freezing in nitrogen is rapid, usually took about 30 minutes. The exact form with PVC tubes was used. The bath for nitrogen consisted of an alumina plate inserted in the PLA dish. Firstly, the form with tubes and alumina plates was cooled on a cooling plate for 5 minutes. Then, the form and plate were laid in a PLA dish. The HAP suspension was injected as above. The liquid nitrogen was carefully poured into the dish from the Dewer flask. The nitrogen was added continuously during the whole freezing. The apparatus was isolated from heat transfer from the surroundings by PS underlay. After freezing, the frozen rods in PVC tubes were

removed from the alumina plate in the freezer. It was necessary to wait one hour before removing the rods from tubes due to the low temperature of the scaffolds.

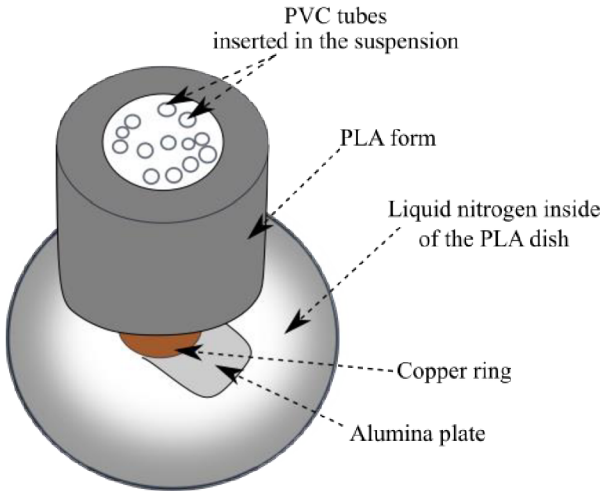

Figure 15*: Freeze-casting in liquid nitrogen.*

4.2.2 Freeze-drying

The freezing step was followed by freeze-drying. It is a process where ice crystals are removed. The bioceramic rods were inserted into the lyophilizer at a pressure of 10 Pa for 24 hours with a constant increase of temperature for 30 °C. The selected program prevents damage to the scaffold lamellae structure after the dissolution of water, and the temperature of sugar glass transition is possible to achieve. The freeze-drying process formed the green body.

4.2.3 Sintering

The HAP and titania green-bodies were sintered on the zirconia plate in a muffle furnace (CLASIC HT1200M) at 1200 °C per 2 hours in the air atmosphere. The heating program was set to every minute the temperature increased by 2 °C to 600 °C. The temperature raised by 5 °C per minute to 1200 °C from 600 °C to 1200 °C. The samples were heated for two hours, and the cooling was set at 5 °C/min down to 700 °C.

Sintered zirconia green-body samples were firstly sintered at 1200 °C/2h, and the second samples were sintered at 1550 °C per 2 hours, which is recommended sintering temperature for zirconia. The heating rate was set to 10 °C·min^{-1} to 700 °C. Then the temperature increased slower by 5 °C·min^{-1} to temperature 1550 °C where it was kept for 2 hours. The cooling rate was set to 5 °C for a minute to avoid thermal shock and cracking.

Moreover, the finished scaffolds were cooled in an open furnace at room temperature, and after that, it was possible to use them for the following measurements, discussed in the next chapter.

A few HAP samples were subjected to temperature 1550 °C per 2 hours to detect a change in microstructure, porosity, and density. The zirconia samples were exposed equally with temperature 1200 °C/2h.

4.3 Characterization

The neural bioceramic scaffolds were characterized by studying the microstructural properties with SEM microscopy and density measurements by the Archimedes method. The investigation of mechanical properties, and biological properties, including testing in SBF solution and MTT test, are presented.

4.3.1 Microstructure characterization of sintered scaffolds

The neural scaffolds must have specific microstructure parameters for proper behaviour. The required properties were determined with scanning electron microscopy, optical microscopy, and density measurement with the Archimedes method.

Scanning electron microscopy

The microstructure of sintered neural scaffolds was analyzed with a field emission scanning electron microscope FIB/SEM Lyra3 XMH (Tescan, Czech Republic) or FEI/SEM Verios 460L (Thermo Fisher, Czech Republic). FIB/SEM microscope is focusing electron/ion beam for scanning over the sample to generate a picture of the surface. FEI/SEM microscope is based on field-emission with excellent material contrast.

For observation, the images were taken from fractured samples to obtain surface characteristics, such as grain sizes, micro features, and lamellae thickness by the emission of secondary electrons. Backscattered electrons were used for compositional contrast. The images were taken for both freezing methods to find out differences at the micro-level.

To enhance the contrast of the samples, the samples, which were immersed in simulated body fluid, were coated with a 12 nm carbon layer in a sputter coater (Leica EM ACE600, Leica Microsystems, Austria).

Stereomicroscopy

The microstructure was measured with stereomicroscope Zeiss Stemi 508 (Zeiss, Germany). The interlamellar distances were measured in constructed photos of sintered neural scaffolds. AxioVision software offers the evaluation from images.

X-ray diffraction

The phase composition of samples was measured with Rigaku SmartLab 3 kW (Rigaku Corporation, Japan) equipped with a Goebble mirror. It is a high-resolution diffractometer with a Cu anode. The XRD was operated at 40 kV voltage, and 30 mA current in Bragg-Brentano measurement mode. 2 theta (2 θ) was measured, which is the angle between the transmitted x-ray beam and the reflected beam.

Measurement of density and porosity

Density, open and closed porosity of sintered samples were measured with the immersion Archimedes method (EN 623-2 [79]) with an analytical balance containing density kit (Mettler Toledo, XSE 204).

Samples were placed under the infra-red lamp for 30 minutes to remove residual wetness. The samples were weighted to get drying mass m_1, which represented the dry mass of

the samples. Then, the samples were inserted into the vacuum chamber (desiccator) and vacuated for 30 minutes under vacuum. The distilled water was infused into the desiccator to cover the whole volume of the samples. The samples were vacuated again for 30 minutes. The samples were left for 30 minutes under atmospheric pressure after vacuation to eliminate temperature and pressure differences. They were inserted into the water of the density kit. The mass m_2 was measured. The water temperature was measured too. The surface of the samples was carefully dried with laboratory paper, but the water was kept inside open pores. The samples were measured in the air to get the mass of open porosity m_3. The relative density in % was calculated by the following equation (8):

$$\rho_{rel} = \frac{m_1}{(m_3 - m_2)} \cdot \frac{\rho_{H_2O}}{\rho_{teor}}, \tag{8}$$

Where ϱ_{H2O} was the density of water at the measured temperature.

The porosity (%) was measured with the measured sample´s mass and dimensions, and gained values were used in the following formula (9):

$$\Pi = 1 - \frac{\rho_{scaf}}{\rho_{teor}}. \tag{9}$$

4.3.2 Mechanical properties

Flexural strength was determined for sintered samples at room temperature with no surface treatment, using the three-point bending test with a crosshead speed of 0.1 mm·min^{-1} and a span of 16 mm. The three-point bending test (3PB) was performed using a universal testing machine ZwickRoell Z50 (Zwick, Germany).

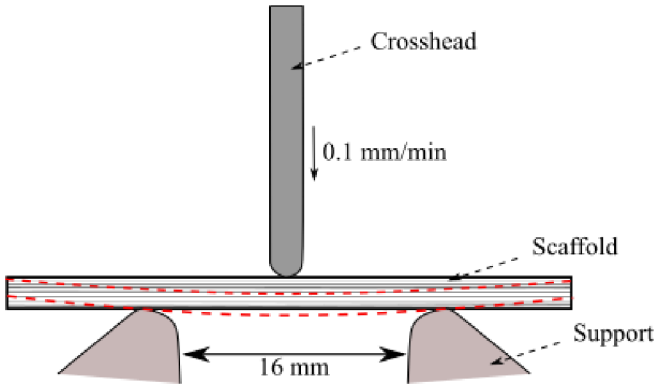

Figure 16: *Three-point bending test apparatus.*

4.3.3 Biological properties

A scaffold is a structure that facilitates cell attachment, proliferation, differentiation, and forms an extracellular matrix. The cells interact with the scaffold by adhesion when they are seeded on the scaffold. When the cell is successfully attached, it provides signaling for proliferation and differentiation. However, the behaviour of the cells on the scaffold is severely limited by the surface topography, chemistry, and architecture [80].

Scaffold pores make it possible to exchange waste, oxygen, and nutrients for supporting cell migration and infiltration, which biological properties interpret. The pore size of the scaffold must be larger than the physical diameter of the cells. For neural cells, it is 10–25 μm. Pore size

smaller than cell size prevents the infiltration of cells. Vice versa, larger pores also limit cell migration due to insufficient bonding [81].

The biological properties were characterized by bioactivity testing in SBF solution, cytotoxicity testing with MTT assay, and cell attachment was observed by confocal microscopy and scanning electron microscopy.

Bioactivity testing in SBF solution

A simulated body fluid (SBF) was prepared to simulate a human physiological environment. SBF is a solution with an ion concentration close to the human blood plasma at physiological temperature. This method is usually used to follow the formation of *in vivo* apatite layer on the material's surface, which causes bonding of the material to the human bone. Once apatite nuclei form, they grow spontaneously by taking the calcium and phosphate from SBF. The formation process is pointing to the bioactivity of the used material. It is often used for ceramic materials, including CaP materials. The solution was prepared according to Kokubo and Takadama with ion concentration shown in table 6 [82].

Table 6*: The comparison of ion concentrations in SBF to the human plasma [81].*

	Ion concentration (mM)								
	Na^+	K^+	Mg^{2+}	Ca^{2+}	Cl^-	HCO_3^-	HPO_4^{2-}	SO_4^{2-}	pH
Blood plasma	142.0	5.0	1.5	2.5	103.0	27.0	1.0	0.5	7.2–7.4
SBF	142.0	5.0	1.5	2.5	147.8	4.2	1.0	0.5	7.4

SBF solution is supersaturated, so it was necessary to avoid precipitation of the solution during preparation. If the precipitation occurred, the SBF preparation was stopped and prepared again. The SBF was prepared in an amount of 1000 ml. First, the 700 ml of ion-exchanged and distilled water was added into the plastic beaker. It was necessary to avoid glass containers because the glass surface could induce apatite nucleation. The beaker was placed into the water bath with a magnetic stirrer covered with a watch glass and tempered at 36.5 °C. The reagents 1 to 8, one by one in the same order, were dissolved (Table 7). Tris-hydroxymethyl aminomethane (Tris) was added to the solution little by little. Simultaneously the pH was controlled to gain 7.45. Then pH was lowered to 7.42 with 1M HCl, and the remaining Tris was dissolved again. The pH was lowered again with HCl to 7.4. The supernatant was cooled down at 20 °C, and the distilled water was added to reach a volume of 1000 ml. The samples were weighed before soaking and soaked in SBF (2.5 ml) at 36.5 °C for 21 days in an incubator (POL-EKO Aparatura CL 53, Poland).

After soaking, the sample was removed from SBF, washed with deionized water, and dried at room temperature. The presence of an apatite layer on the surface of the sample was examined using scanning electron microscopy. The material was considered to be bioactive if the presence of an apatite layer was confirmed.

Table 7: *Order and amounts of reagents for preparing 1000 ml of SBF.*

Order	Reagent	Amount
1	NaCl	8.035 g
2	$NaHCO_3$	0.355 g
3	KCl	0.225 g
4	$K_2HPO_4 \cdot 3\ H_2O$	0.231 g
5	$MgCl_2 \cdot 6\ H_2O$	0.311 g
6	1M HCl	39 ml
7	$CaCl_2$	0.292 g
8	Na_2SO_4	0.072 g
9	Tris	6.118 g
10	1M HCl	0–5 ml

Cell seeding and cultivation

The Schwann cell line was studied *in vitro* to determine the effect of the scaffold using a direct contact assay. The neuronal Schwann cells from cell line *Rattus norvegicus* located in the peripheral nervous system (RT4D6P2T) were used. The Schwann cells are one of the essential regenerative factors in nerve repair – the conduction of nervous impulses along axons, the nerve extracellular matrix production, and the production of chemotactic factors [83].

The cells were stored in liquid nitrogen at a temperature −130 °C. The vial with culture was gently agitated in a water bath (Biosan WB-4MS) at a temperature of 37 °C for 2 minutes with the O-ring and cap out of the water to prevent contamination. The vial with heated cells was decontaminated with a 70% ethanol spray and transferred to a clean box. The 15 ml of RPMI-1640 cultivation medium, containing L-glutamine, sodium bicarbonate, antibiotics, growth factors, was pipetted to the cultivation vessel to cover the entire bottom surface. The cells were pipetted inside the cultivation medium and incubated for a day inside an incubator (Galaxy 48R) in an air atmosphere at 37 °C, and 5% CO_2.

The passaging, or subculturing of cells, was the next step of cytotoxicity testing. The inactivated FBS (fetal bovine serum) was taken from the freezer and defrosted at 37 °C in a water bath. The medium was removed from the cultivation vessel, and the vessel was washed with PBS (Phosphate-buffer saline) buffer and removed. The trypsin was ten times diluted with PBS buffer. The 0.5 ml proteolytic enzyme trypsin was added to the cell culture for dissociation adherent cells on the vessel and slowly spilled on the vessel's bottom. After 3 minutes, the cell dissociation was checked under an optical microscope. The trypsin was inactivated with the medium. The 10 µl of cells were mixed with the same amount of triptany urine. Then it was pipetted on the counter plate and inserted into the counter (Countess II FL). The program of the counter recalculated the ratio of living and death cells inside of one ml. The amount of 5 000 living cells (in ml) with the medium were added inside a hole of 96 microtiter plate with a

multichannel pipette; 12 holes were omitted for solvent. The remaining cells were pipetted to the cultivation vessel.

After 24 hours of cultivation in the microtiter plate, the powder dissolved in PBS (1 mg/ml) was added to the microtiter plate in the concentration series in a ratio of 1:1 with the medium. For each sample, the concentration series were triplicated. The titration plate was left in an incubator for 24 hours.

Cytotoxicity testing – MTT assay

The MTT (3-(4,5-dimethylthiazol-2-yl)-2,5-diphenyltetrazolium bromide) solution was prepared at a concentration of 5 mg/ml. The medium with the powder from the holes was carefully removed, 10 µl of MTT was added to the holes with a multichannel pipette, left for 2 hours in an incubator to create MTT purple crystals. The MTT was removed, and 100 µl of DMSO was added to each hole, crystals were dissolved. Samples were prepared for spectrophotometry measurement with plate reader Infinite 200Pro (Tecan) at 570 nm with 5 number flashes. When cells die, they lose the ability to convert MTT into purple-colored formazan, in which absorbance is measured.

Analysis of cell viability

The cytotoxicity was determined by the obtained absorbance, which described the viability (%) of the cells according to the equation (10):

$$Viability = \frac{A_{sample}}{A_{control}} \cdot 100\,, \tag{10}$$

A_{sample} was absorbance measured for each concentration of the sample, $A_{control}$ was the absorbance of the cells cultivated in a pure medium. The absorbance ratio must be multiplied by 100 to give a percentage of cell viability. Absorbance values greater than the control indicate cell proliferation. Lower values suggest cell death or inhibition.

Confocal microscopy

The cell infiltration into the lamellar system and cell adhesion was evaluated with a confocal microscope Zeiss LSM 880 (Zeiss, Germany). The microscope is equipped with four solid-state lasers (405, 561, 594, and 633 nm), argon laser (458, 488, and 514 nm), two multi alkali PMT detectors, 32 channel spectral GaAsP detector, Airyscan detector, and T-PMT for transmitted light detection.

To maintain the cellular structure as much as possible to the native state allows a fixation process. The sample was first washed in PBS buffer and fixed in 4% formaldehyde. After 15 minutes, the sample was rewashed with PBS and permeabilized with detergent (Triton X-100, Sigma-Aldrich) for 15 minutes, washed with PBS, and the phalloidin dye dissolved in 1% BSA with PBS was added. The phalloidin (Alexa Fluor™ 488 Phalloidin, Thermo Fisher Scientific) dyes the nerve fibers. The samples were let with phalloidin per 1 hour. Then the samples were washed in PBS, and the DAPI (DAPI Solution, Thermo Fisher Scientific) was added to the dye cell nucleus. For fixation of characteristic green (phalloidin) and blue (DAPI) colors, the slow fade (Diamond antifade, Thermo Fisher Scientific) was added.

Scanning electron microscopy

The adhesion of neural cells was observed under field emission scanning electron microscope MAIA 3 (TESCAN, Czech republic). The microscope contains a detection system and high spatial resolution, which allows the observation of the most delicate surface details.

The fixation process is also necessary for SEM microscopy. The sample with cultured cells was washed with pre-heated PBS at 37 °C. Then, the cells were fixed with 2% glutaraldehyde in PBS. The samples were washed with Milli-Q water two times for 10 minutes. Dehydration is an essential step in preparing samples for SEM. It was realized with an EtOH concentration board (40–100%). For all concentrations 40–90% of EtOH, the sample was dehydrated for 10 minutes, but the sample in 100% EtOH was dried two times for 15 minutes. After the dehydrating, the sample was incubated in hexamethyldisilazane (HMDS) for 30 minutes 2 times.

5 RESULTS

5.1 Calcium phosphate neural scaffolds

The calcium phosphate (CaP) scaffolds were observed as primary samples. The samples were frozen with freezing processes described in chapter 4.2.1 and sintered at two temperatures: 1200 °C and 1550 °C to determine the change in the microstructure levels. The summary of samples and their labels is described in table 8.

Table 8*: Short characteristic of prepared samples.*

Label	Freezing process	Sintering temperature (°C)
CaP_20_1200	−5 °C/20 min	1200 °C/2 h
CaP_N_1200	Liquid nitrogen ~ −16 °C/20 min	1200 °C/2 h
CaP_20_1550	−5 °C/20 min	1550 °C/2 h

5.1.1 Microstructure

The microstructure was determined with SEM micrographs of samples with both freezing velocities. The form of interlamellar spaces, the appearance of interlamellar bridges, grain size, and intergranular porosity were observed and compared.

The sintering temperature was firstly set at 1200 °C, and the effect of the freeze-casting process on porosity and interlamellar distance was studied. The measurements were performed for sintered CaP scaffolds frozen in liquid nitrogen and with a controlled thermal gradient. The results of the measurement are shown in table 9. The lamellar thickness, interlamellar distances, were measured with ten samples, and porosity was measured with 30 samples (only porosity for CaP_20_1550 was measured with five samples). The comparison of porosity showed no significant differences for all prepared samples.

Table 9: *Average interlamellar distances, lamellar thickness, and porosity of sintered CaP scaffolds.*

Sample	Freezing rate (µm/s)	Interlamellar distance (µm)	Lamellar thickness (µm)	Porosity (%)
CaP_20_1200	5.3 ± 0.2	58.1 ± 6.4	93.0 ± 7.3	71.9 ± 2.8
CaP_N_1200	27.9 ± 3.7	12.6 ± 3.5	23.0 ± 5.6	71.4 ± 1.9
CaP_20_1550	5.3 ± 0.2	63.3 ± 5.7	76.7 ± 9.1	71.1 ± 0.4

The compelling changes based on freezing rates could be found in changes in interlamellar distances and lamellar thickness. When the freezing rate was lower, the ice-crystal growth was supported, giving rise to a lamellar system with larger distances between lamellas. The interlamellar distances decreased when the freezing rate increased. A lower freezing rate resulted in almost five times greater interlamellar spaces (58.1 µm). The neural scaffolds

require interlamellar distances of about 10–20 µm for precise infiltration of neural cells. This fact showed that proper infiltration provides scaffold prepared with liquid nitrogen (CaP_N_1200) with an interlamellar distance of 12.6 µm. Verification of this fact is discussed in chapter 5.1.3.

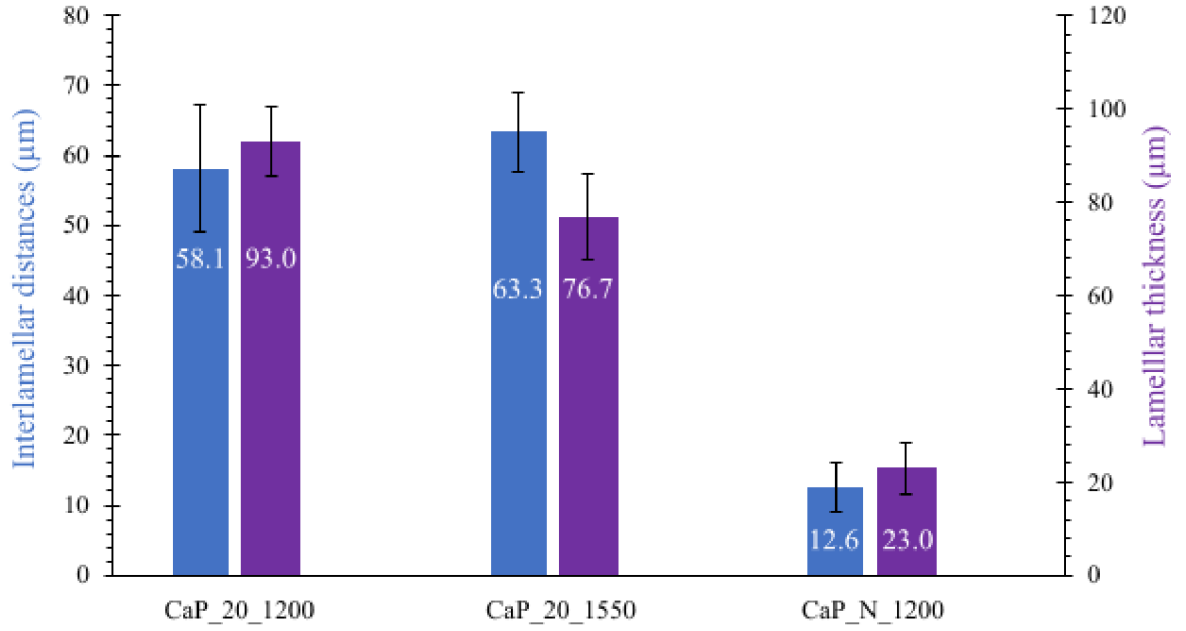

Figure 17: *Differences in interlamellar distances and lamellar thickness of CaP samples. The blue columns represent interlamellar distances, and the purple columns are values of lamellar thickness.*

Samples prepared by freeze-casting with a controlled temperature gradient

The microstructure of sintered samples frozen with a controlled thermal gradient can be seen in figure 18. Prepared scaffolds were highly porous and with a spacious lamellar system. The detailed photo of interlamellar spaces (Figure 18a) shows perpendicular ice growth to the cooling plate. The average interlamellar size was 51.5 ± 9.1 µm.

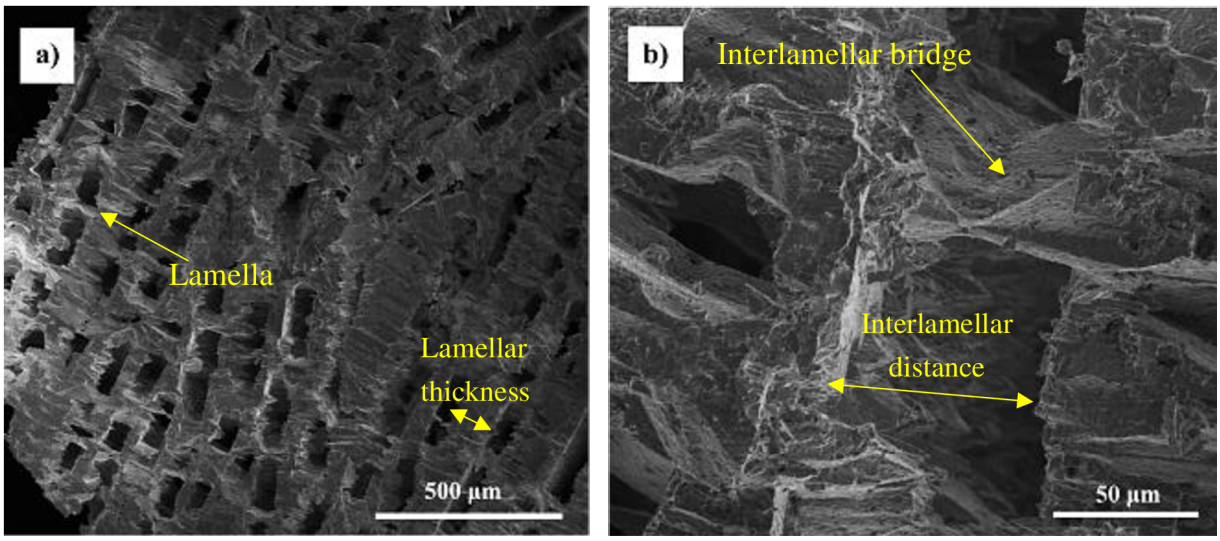

Figure 18: *Microstructure of sintered neural scaffolds CaP_20_1200; a) parallel lamellar system, b) interlamellar bridges.*

The slower cooling gave rise to ice crystals with larger dimensions than nitrogen freezing (Figure 21). The appearance of interlamellar bridges is shown in figure 18b.

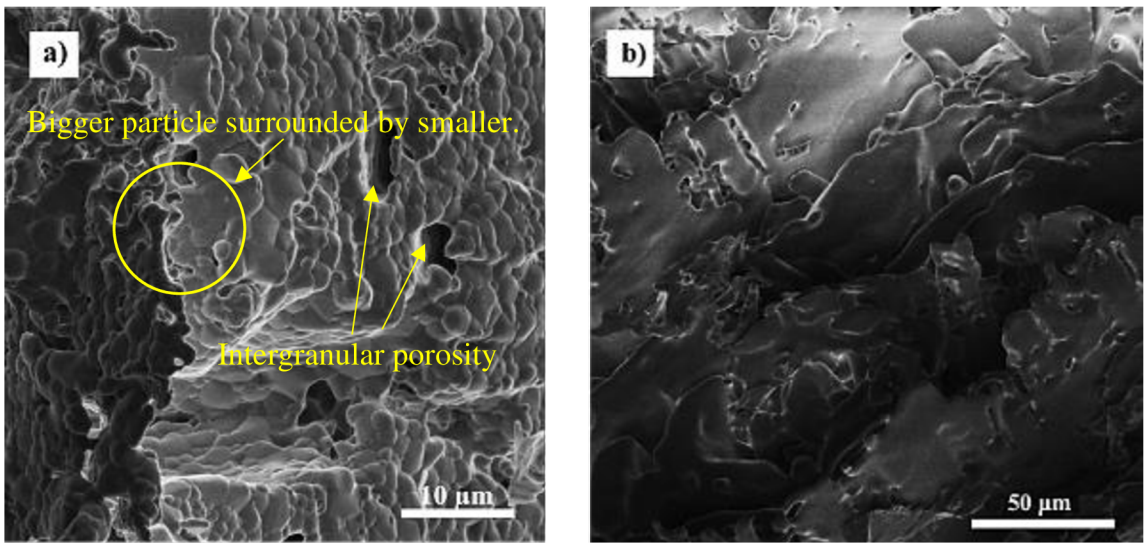

Figure 19: *Sintering temperature effect on CaP particles; a) CaP_20_1200, b) α-TCP phase of CaP_20_1550.*

The HAP was decomposed to β-TCP during sintering with a temperature of 1200 °C. It is possible to see bigger particles surrounded by smaller ones in figure 19a, which indicated the presence of the β-TCP phase [84]. There was the presence of multiscale grain sizes from 1–6 µm. The slower cooling supported the increase of the number of β-TCP particles, which were more compact and larger than HAP particles. The sample sintered at 1550 °C had fully connected particles without intergranular porosity (Figure 19b). Unseparated particles indicated the presence of the α-TCP phase. A temperature of 1550 °C is not an appropriate sintering temperature. Ceramic particles became more aggregated, and the ceramic became much denser when the temperature increased.

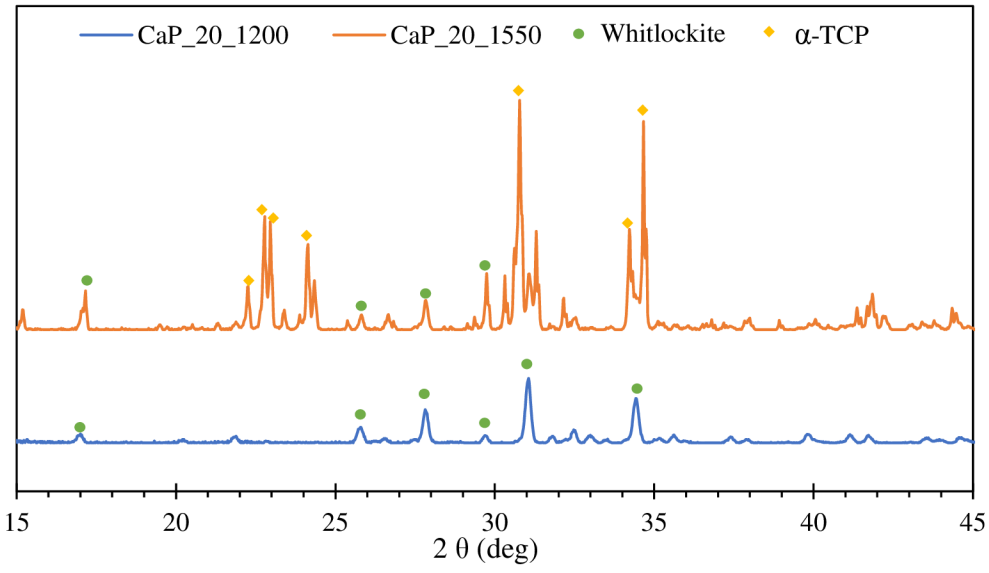

Figure 20: *XRD analysis of CaP samples frozen with the same controlled thermal gradient program and sintered at different temperatures.*

The presence of α-TCP and β-TCP (Whitlockite) was confirmed with XRD analysis (Figure 20), where phase composition of the sample sintered at 1200 °C (CaP_20_1200) was compared to sample sintered at 1550 °C (CaP_20_1550). The samples CaP_20_1200 contained only the Whitlockite phase, which is a stable phase with less solubility. On the other hand, sample CaP_20_1550 consisted of multiple phases, including Whitlockite and α-TCP. The aggregation of particles, which makes the structure look over-sintered, is caused by the presence of the α-TCP phase, which is the most soluble phase.

Samples prepared by freeze-casting in liquid nitrogen

Figure 21 shows the microstructure of the highly porous sintered scaffold frozen in liquid nitrogen. The liquid nitrogen gave rise to ice crystals with a smaller dimension but with higher multiplicity, parallel to each other and perpendicular to the cooling ring (Figure 21a). SEM images of the CaP_N_1200 sample show a uniform lamellar-type microstructure throughout the sample, with the lamellas oriented with the freezing direction. The lamellar system shows significant thinness with an interlamellar size of 12.6 ± 3.5 µm, with a length of 4 cm extended from the bottom of the construct to the top.

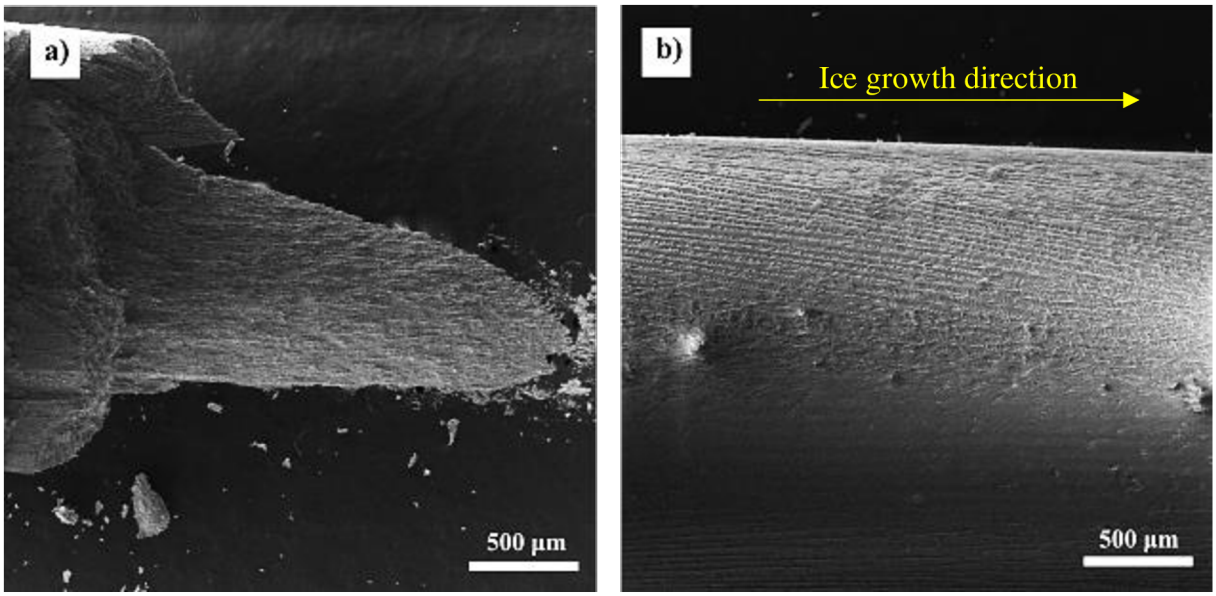

Figure 21*: Microstructure of sintered CaP neural scaffolds frozen in liquid nitrogen (CaP_N_1200); a) lamellar system, b) detailed view on the lamellar system.*

Figure 22 shows a detailed view of the lamellar system with lamellar bridges. During the freeze-casting, ice-crystal grew in branch-like morphology, deviating from the main direction, visible as a dendritic structure (Figure 22a). The dendritic structures formed interlamellar bridges in some cases. At a closer look, it is possible to observe some microcracks, which are defects in the ceramic walls and reduces their strength. However, it is a common phenomenon in the freeze-casting process. Figure 22b was taken to compare grain size and intergranular porosity with samples frozen with a controlled thermal gradient. It is possible to see places with intergranular porosity. The grain size is smaller but more oval, which leads to the fact that HAP was in a higher ratio. Compared to freezing with a controlled thermal gradient, the freeze-casting in liquid nitrogen created uniform grains with a diameter of about 1–2 µm. The aggregation was not present.

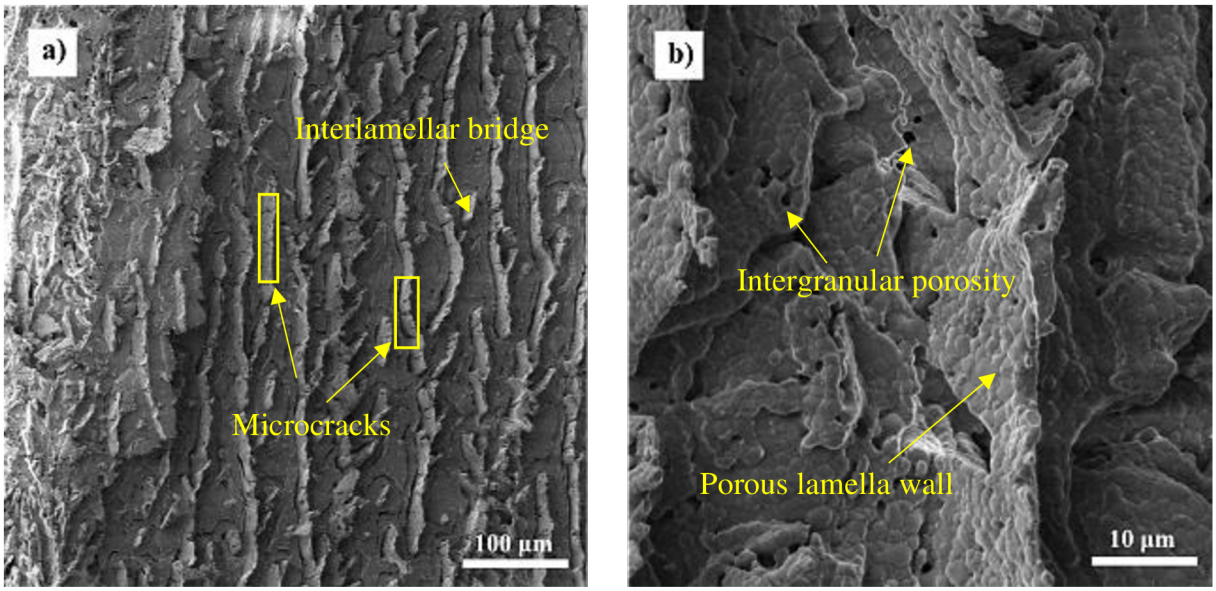

Figure 22: *The detailed micrographs of CaP_N_1200 scaffolds; a) lamellar system with interlamellar bridges, b) detailed view on porous lamella wall.*

5.1.2 Mechanical properties

One of the most important parameters to evaluate the performance of the CaP bioceramic scaffold is mechanical stability. The resistance of prepared CaP neural scaffolds to the mechanical loading was characterized by a bending test with 30 samples for both types. Mechanical performance under a 3-point flexural test was evaluated for freeze-casted scaffolds CaP_20_1200 and CaP_N_1200. The comparison of the sintered scaffolds is shown in Figure 23.

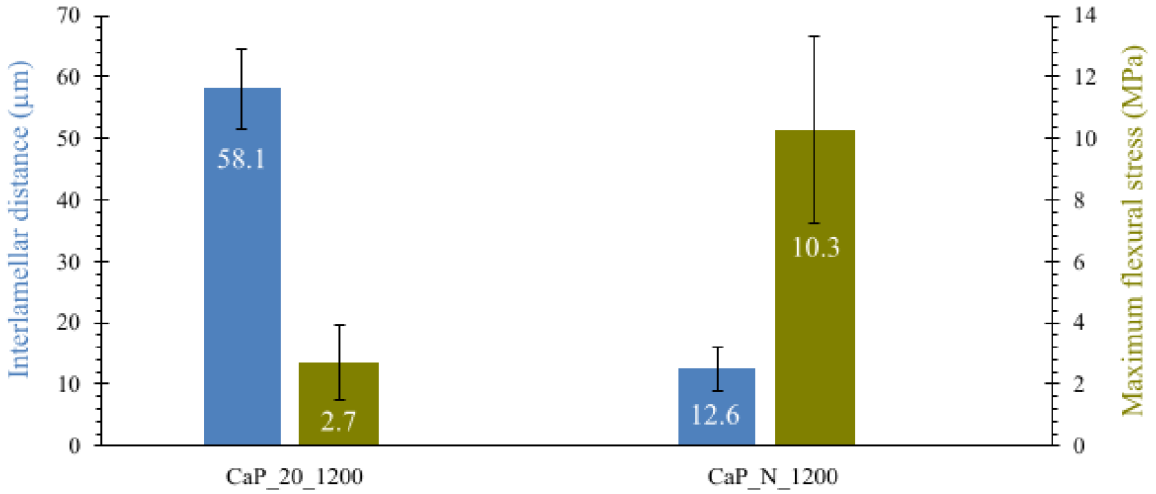

Figure 23: *A dependence of interlamellar distances on the maximum flexural stress of manufactured CaP scaffolds. The blue columns represent interlamellar distances, and the green columns are values of applied maximum flexural stress.*

The dependency of mechanical resistance with both freezing processes was present. According to the high porosity values, around 71 %, the mechanical properties were very high. The porosity of CaP scaffolds had no compelling impact as the interlamellar distance had on mechanical tolerance. The higher freezing rate and higher freezing time formed scaffolds with smaller interlamellar spaces, reflecting better mechanical properties. The flexural strength of the CaP_20_1200 sample was 2.7 ± 1.2 MPa, where the lowest value was 0.8 MPa and the highest 5.5 MPa. The flexural strength of CaP_N_1200 was 10.2 ± 3.1 MPa, which is twice the value. The highest measurement had 16.3 MPa, and the lowest value was 5.9 MPa. The worst sample from the measurement of CaP_N_1200 samples had higher flexural strength than the best sample from CaP_20_1200 measurements. The difference between the highest and lowest value was connected to different pore distribution in the samples. Both values of flexural stress are excellent because they are not low for scaffold with a porosity of ~71 %. The sample CaP_20_1550 was not mechanical tested due to low stability during the manipulation.

With increasing relative density, the cell walls thicken, and pore space shrinks. With the increase of the relative density of the neural scaffolds, the mechanical properties increase. The relative density of CaP scaffold frozen in liquid nitrogen was higher than for scaffolds frozen with controlled thermal gradient, which correlates with increasing flexural stability.

5.1.3 Biological properties

The goal of the thesis was to study cell survival and proliferation in the context of the CaP neural scaffold. Due to the high content of calcium ions in hydroxyapatite powder, the effect of calcium ions on cell proliferation and survival was observed.

Bioactivity testing in simulated body fluid

The calcium phosphate film is formed on the CaP scaffold surface when implanted into the body, allowing bonding to the living bone *in vivo* [82]. The high resorbality of CaP bioceramic probably causes this phenomenon. However, this sensation can be a paradox for nerve cells.

The CaP scaffolds were soaked in SBF for 21 days. Samples were weighed before soaking m_B and after soaking m_{SBF}. The weight change was determined to investigate the growth of apatite on the surface. The results are shown in table 10. The weight was higher after soaking in SBF, which was caused by forming the apatite layer during the soaking.

Table 10: *Results of CaP scaffolds soaked in SBF for 21 days.*

Label	m_B (g)	m_{SBF} (g)	Weight change
CaP_20_1200	0.0377	0.0398	+ 5.6 %
CaP_20_1550	0.0416	0.0432	+ 3.9 %
CaP_N_1200	0.0508	0.0639	+ 25.8 %

The iso-electric point of HAP in water is between 5 and 7 pH. Therefore, the HAP can reveal the negative surface charge by exposing hydroxyl and phosphate units in its crystal structure (Figure 24). The negative surface charge interacts with the positive Ca^{2+} ions from SBF solution with the formation of Ca-rich ACP. This layer increases the positive charge of HAP. Hence, it interacts with negative ions PO_4^{2-} contained in SBF, consequently forming Ca-poor ACP. This type of ACP is considered a precursor of bone-like apatite crystallization due to the low solubility of apatite in SBF. The Ca-rich and Ca-poor ACP are considered nucleation sites [85].

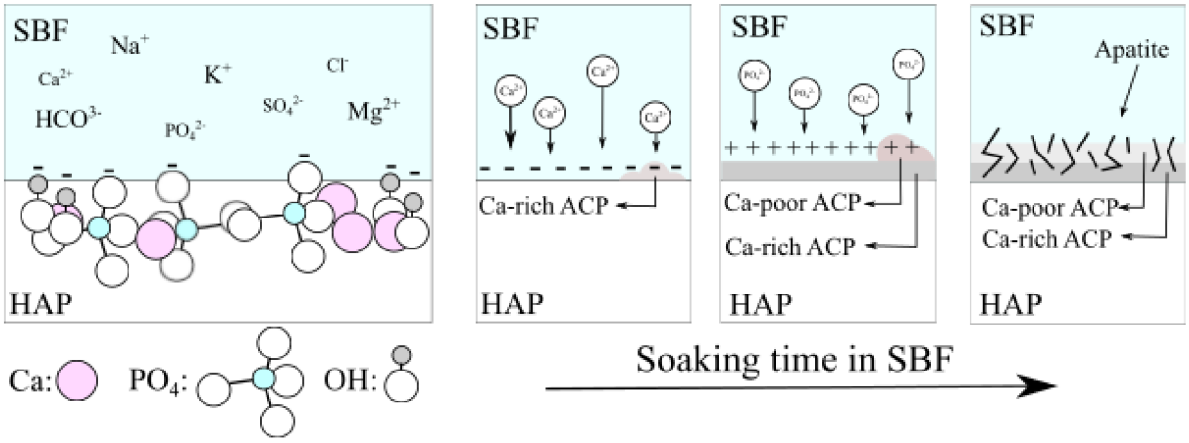

Figure 24: *Process of forming an apatite layer on the surface of HAP scaffolds [85].*

Once the apatite layer was formed in SBF, the apatite grew spontaneously, consuming the calcium and phosphate ions from the solution and incorporating other ions (Na^+, K^+, Mg^{2+}) into its structure. Thus, the weight of the sample increased as a result.

After 21 days of immersion in SBF, the formation of the apatite layer was present in all CaP samples. In figure 25, the origin of nucleation centers can be observed. Figure 25 shows abnormal grains on the CaP grains, which were not observed with SEM analysis for not-soaked samples (Figure 19). Both samples had these abnormal sites, from which it was possible to infer the origin of nucleation sites. In figure 25b, the formation from nucleation centers to apatite structures can be observed.

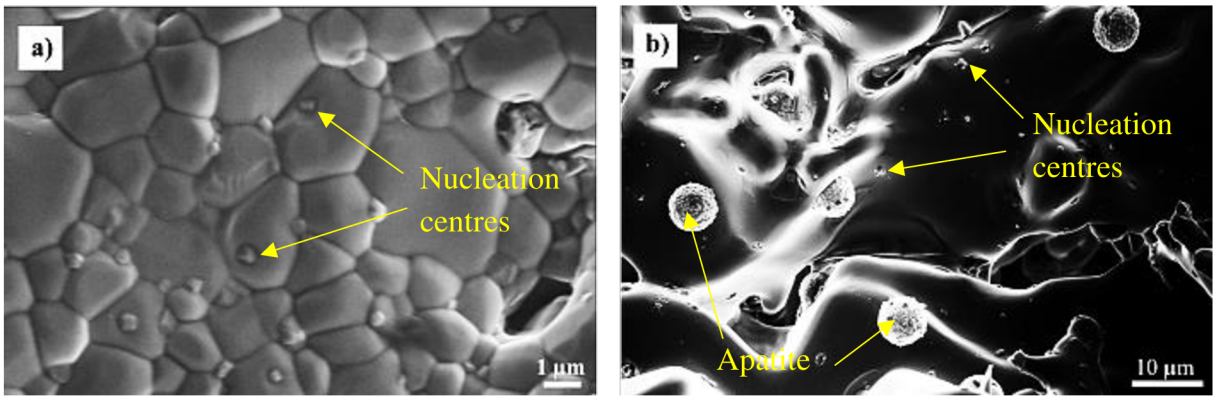

Figure 25: *The present origin of the nucleation centers in samples frozen with a controlled thermal gradient; a) CaP_20_1200, b) CaP_20_1550.*

The typical cauliflower structure was observed with CaP samples frozen in liquid nitrogen and sintered at 1200 °C. Table 10 follows that this sample gained weight over 25 %, indicating the apatite layer's growth. The freezing in liquid nitrogen could help phase transformation of HAP to α-TCP, the most soluble CaP phase. The ions were more effectively exchanged, which helped the formation of a cauliflower structure. In figure 26, it is possible to see a detailed Ca-rich and Ca-poor ACP layer, which was more porous.

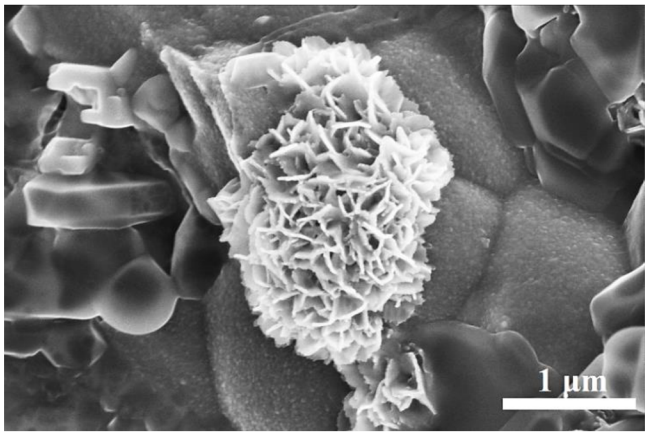

Figure 26: *Crystallized cauliflower structure in CaP_N_1200.*

Cytotoxicity of calcium phosphate powders

Four powders were used for cytotoxicity testing: untreated commercial one (Sigma-Aldrich), and the three same powders, but thermally treated – calcinated at 800 °C/1h (HAP 800 °C), frozen in nitrogen (HAP N_2), and frozen with a thermal gradient (HAP 20 min). The HAP nitrogen and HAP 20 min were sintered at 1200 °C. The temperature treating has profits, including eliminating organic impurities, sterilizing the powders, or coursing grains. The thermal treatment of the powder causes phase transformation of calcium phosphates. Therefore, the β-TCP and α-TCP phases presence were expected, associated with varying solubility of calcium and phosphate ions (Table 1).

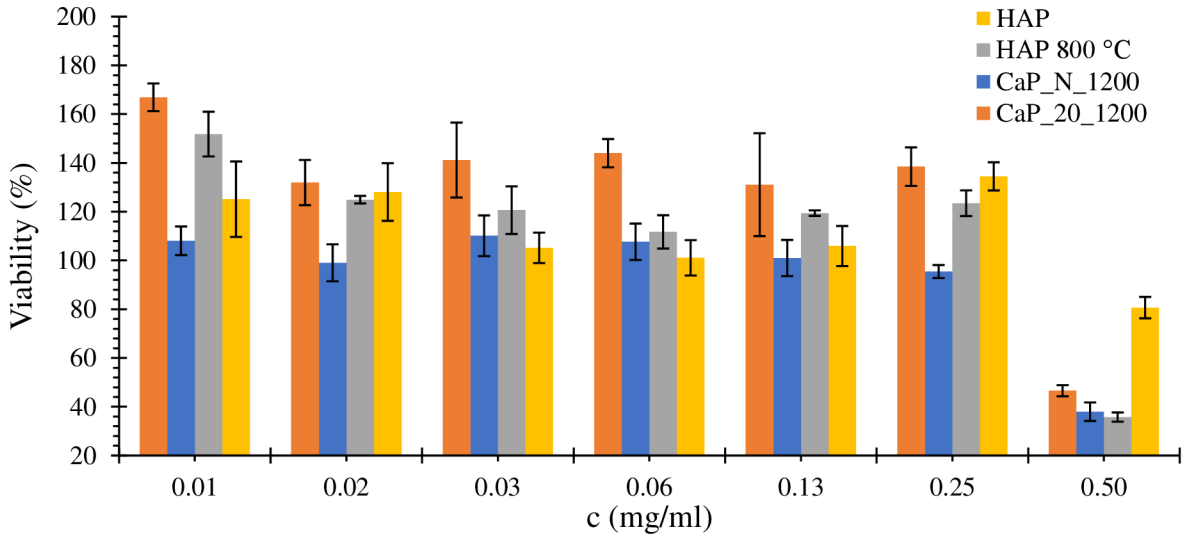

Figure 27: *Viability of Schwann cells with increasing calcium phosphate concentration in PBS. The viability over 100 % causes bioactive properties of the powder. The viability under 100 % causes cytotoxicity of Schwann cells.*

A high ratio of calcium ions causes harmful effects on the Schwann cells, which are the most critical dynamic cells in nerve regeneration. There was a present fine line between a tolerable level of calcium ions and one that will kill the most cells in culture. For prepared scaffolds, it was 0.25 mg/ml of CaP contain.

Biocompatibility of CaP scaffold with Schwann cells

The samples were observed under the optical microscope (EVOS FL Auto) after 24 hours. Figure 28b shows less amount of adhered cells on the scaffolds than the control sample (Figure 28a). During the observation, it was possible to see the excretion of the material on the surface of the scaffold (Figure 28b) and to the media. Probably, it was calcium and phosphate ions, which were fatal for Schwann cells.

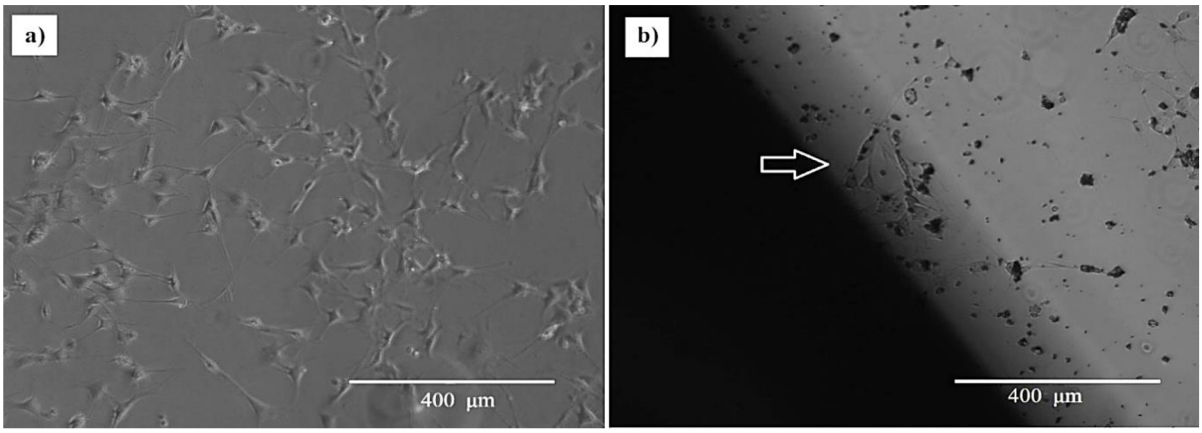

Figure 28: *Comparison of cell viability after 24 hours cultivation on CaP scaffold; a) control sample; b) adhered cells on the CaP scaffold.*

The neural scaffold was evaluated for its ability to support *in vitro* neurite extension using Schwann cells. The cells were seeded into the 9-hole cultivation plate, with a higher concentration of cells than is commonly used. The higher concentration should support the finding of cells floating in media, not only adhere to the cultivation hole's bottom. After 48 hours, the cells were fixed and checked under a confocal microscope and scanning electron microscope. The photos from the surface and lamellar system were performed.

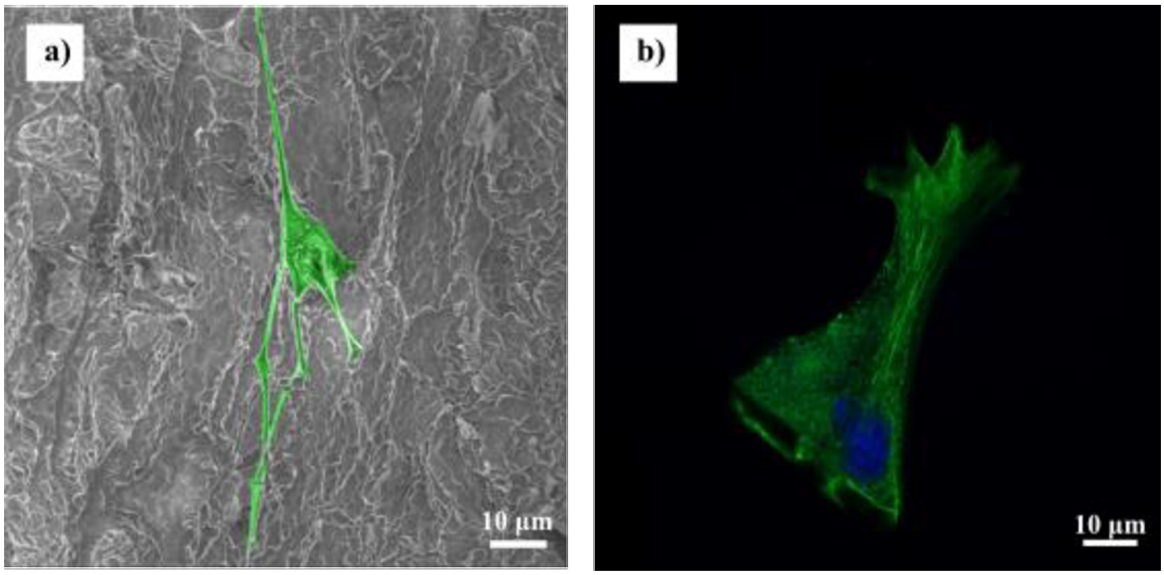

Figure 29: *Adhered cells on CaP_20_1200 scaffolds; a) SEM micrograph, b) photo taken by confocal microscope.*

The cell adhesion was observed for all CaP scaffolds. In figure 29, the cell surface growth on a scaffold frozen in liquid nitrogen and sintered at 1200 °C can be observed. The cell was not under stress, which the elongated shape represented (Figure 29a). The cells grew only on the surface of the scaffold. No cells were current inside of the lamellar system. The infiltration was not successful 48 hours after the cultivation.

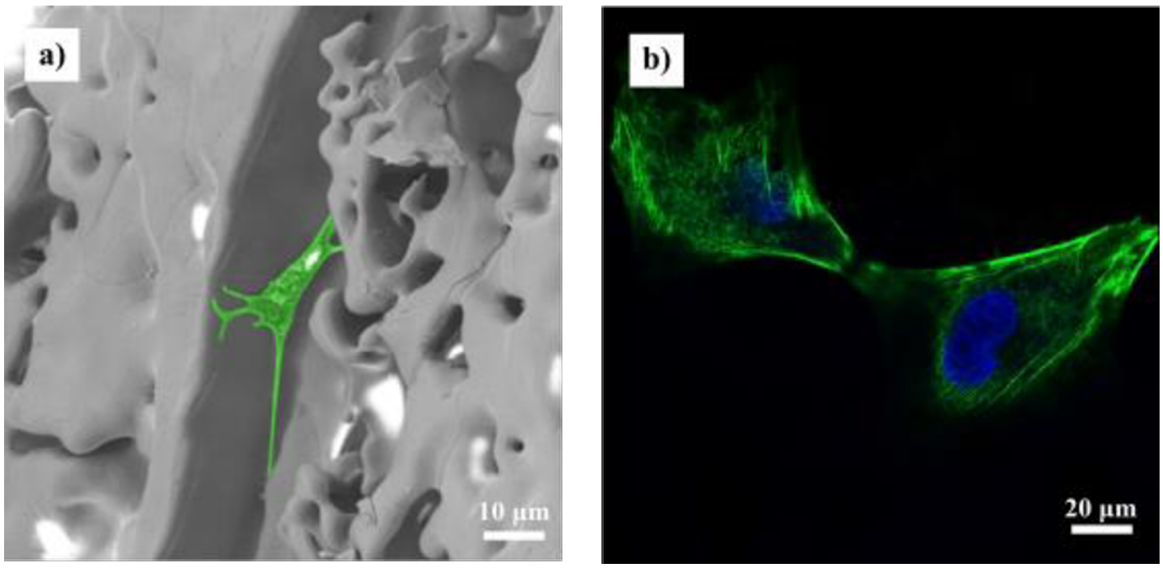

Figure 30: *Adhered cells on CaP_20_1550; a) SEM micrograph, b) photo taken by confocal microscope.*

The CaP scaffolds sintered at 1550 °C had different pore morphology – the structure was melted with a smooth surface. Figure 30a follows that neural cells had not required a rough surface. The morphology of the cell was accurate, without any stress cells observed. Figure 30b shows that the cell's connection was probably observed.

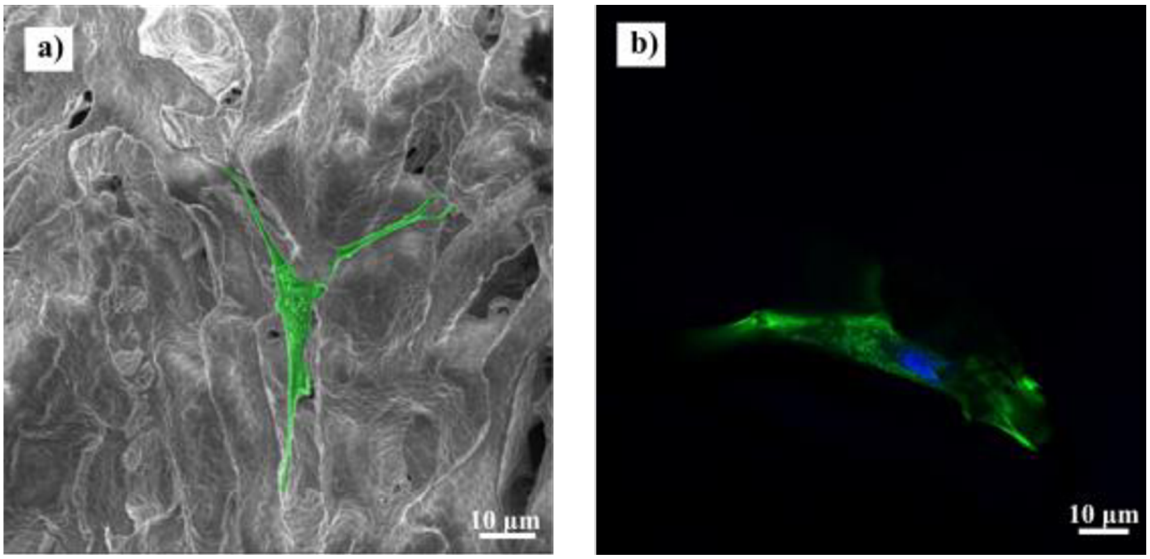

Figure 31: *Adhered cells on CaP_N_1200 scaffolds; a) SEM micrograph, b) photo taken by confocal microscope.*

The cells adhered to the surface and inner lamellar system in a sample frozen in liquid nitrogen and sintered at 1200 °C (CaP_N_1200). The cell fitted the space that is defined by its surroundings without stress reactions (Figure 31a). The elongated shape was observed under a confocal microscope (Figure 31b), which represented growth in the direction of the lamella.

5.1.4 Summary of Chapter 5.1

The three types of CaP scaffolds were prepared with different grain morphology and lamellar system – scaffold frozen with controlled thermal gradient (CaP_20_1200) and scaffold frozen in liquid nitrogen (CaP_N_1200), where both were sintered at 1200 °C; and the scaffold frozen with controlled thermal gradient and sintered at 1550 °C (CaP_20_1550). All samples had total porosity values of ~71 %. Freezing rates had a severe impact on final interlamellar distances. When the freezing rate was lower, the ice-crystal had a long time to grow, it froze in a larger dimension, and after lyophilization, the lamellar distance was more extensive. A neural scaffold should have a pore diameter range between 10–30 µm, which the CaP_N_1200 sample had (12.6 ± 3.5 µm). The most significant impact of sintering temperature is on the grains, which were reflected in mechanical properties. At the temperature of 1550 °C, the grains of CaP_20_1550 were more aggregated, which indicated the presence of α-TCP. The phase composition was confirmed with XRD analysis. The mechanical properties of CaP_20_1550 were not measured due to low mechanical stability during the manipulation. The CaP_N_1200 sample had optimistic flexural stress values of 10.2 ± 3.1 MPa.

The CaP based scaffolds could exchange ions in a solution, where Ca^{2+} and PO_4^{2-} ions were present. When the pH of the surrounding was between 5–7, the HAP in the structure revealed the negative surface charge by exposing hydroxyl and phosphate groups and interact with calcium and phosphate ions in solution. This fact was determined with testing in the SBF solution, where the apatite cauliflower structure was observed in the sample CaP_N_1200 (Figure 26). The origin of nucleation sites was observed on samples CaP_20_1200 and CaP_20_1550 (Figure 25). High calcium levels were harmful to neural cells. It damaged them

and caused cell death. This fact was observed with all CaP samples in cytotoxicity tests (Figure 27), where the scaffolds had a negative impact on cell viability with higher concentrations. When the apatite was formed on the scaffolds´ surface, it related to a higher concentration of calcium ions on the surface and around the scaffold in media solution. It was necessary to use higher concentrations of cell suspensions to ensure cultivation on the scaffold surface also. This step ensured that the cell adhesion was on all CaP scaffolds, where cells had appropriate morphology, not under stress (elongated shape of cells). From the SEM micrographs, it was possible to observe that cells wanted to adhere; their fibers were caught in several dimensions. CaP_N_1200 scaffold was infiltrated by cells also inside of the lamellar system.

5.2 Zirconia neural scaffolds

5.2.1 Microstructure

The comparison of yttria-stabilized zirconia (YSZ, TZ-8Y) microstructure was specified on samples frozen with a thermal gradient (−5 °C/20 min) and in liquid nitrogen approximately −16 °C/20 min. The samples were sintered at two different temperatures (1200 °C and 1550 °C). Therefore, the temperature effect was observed. The summary of samples is described in table 11.

Table 11: *Summary of zirconia samples.*

Label	Freezing process	Sintering temperature (°C)
Zr_20_1200	−5 °C/20 min	1200 °C/2 h
Zr_N_1200	Liquid nitrogen ~ −16 °C/20 min	1200 °C/2 h
Zr_20_1550	−5 °C/20 min	1550 °C/2 h
Zr_N_1550	Liquid nitrogen ~ −16 °C/20 min	1550 °C/2 h

Zirconia neural scaffolds of different total porosity and interlamellar distances were prepared by changing the sintering temperature and freezing process. The freezing process had no impact on relative density and porosity values, as sintering temperature had. With increasing sintering temperature, the porosity decreased, which relates to the shrink of the sample. Decreasing the porosity of the scaffolds increased the mechanical properties. The high porosity values of scaffolds sintered at 1200 °C caused low mechanical properties. The manipulation destroyed the samples, so the mechanical and biological properties were not observed.

Table 12: *Average interlamellar distances, relative density, and porosity of sintered zirconia scaffolds.*

Sample	Freezing rate (µm/s)	Interlamellar distance (µm)	Lamellar thickness (µm)	Porosity (%)
Zr_20_1200	5.9 ± 0.3	63.2 ± 9.9	58.0 ± 9.6	81.7 ± 1.7
Zr_N_1200	25.2 ± 2.4	23.2 ± 4.2	12.6 ± 2.8	82.4 ± 2.1
Zr_20_1550	5.9 ± 0.3	50.8 ± 8.3	139.4 ± 24.3	64.1 ± 2.4
Zr_N_1550	25.2 ± 2.4	14.5 ± 2.6	14.8 ± 3.5	63.4 ± 2.1

The interlamellar distances were determined for all prepared zirconia samples (Table 12). The interlamellar distances decreased as the freezing velocities increased, as predicted by CaP samples' results. The sintering temperature had an impact on final interlamellar distances. It shrank the sample. The interlamellar distances decreased about 10 µm with increasing sintering temperature (Figure 32). The lamellas wall had larger dimensions after sintering, which relates to grains' growth. The grains grew during the sintering, and walls become thicker.

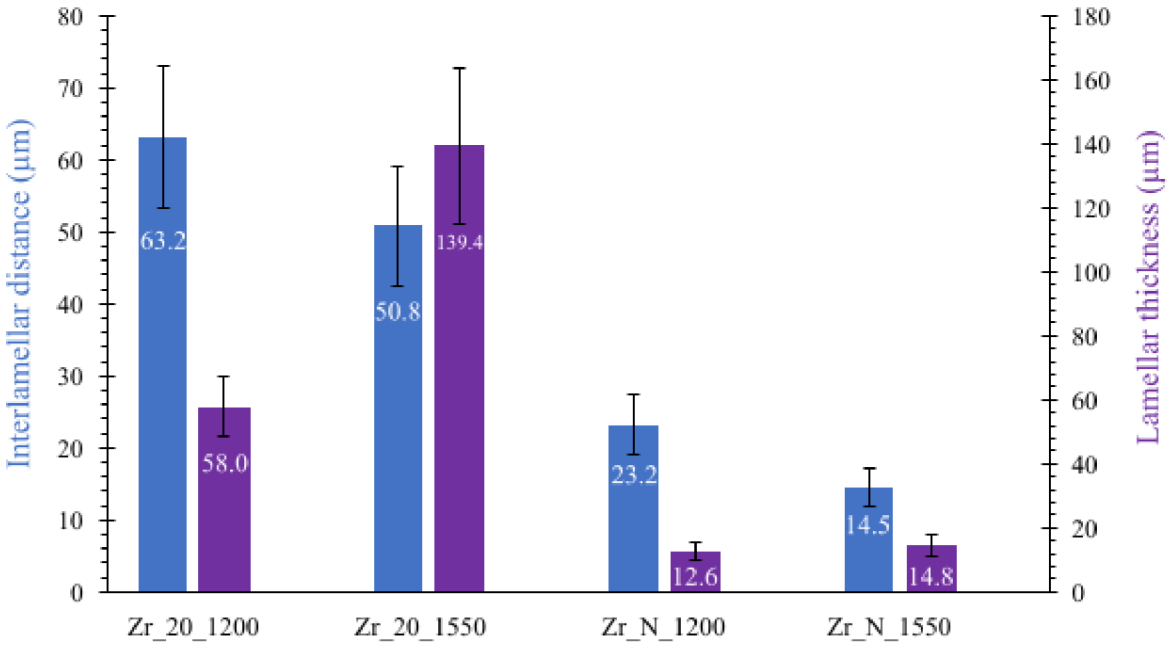

Figure 32: *Differences in interlamellar distances and lamellar thickness of zirconia samples. The blue columns represent interlamellar distances, and the purple columns are values of lamellar thickness.*

The samples frozen with controlled thermal gradient had a bigger standard deviation because ice-crystal grew slower, and the lamellar formation was not homogenous, as for nitrogen samples.

Samples prepared by freeze-casting with a controlled temperature gradient

Different sintering temperatures prepared porous zirconia samples frozen with a controlled temperature gradient with different porosity and pore architecture. The microstructure of the yttria-stabilized zirconia scaffold Zr_20_1200 is shown in figure 33 on several magnification levels. The samples were sintered at the temperature of 1200 °C per 2 hours. It is possible to see a lamellar system perpendicular to ice growth with a dendritic structure (Figure 33a). The apparent intergranular porosity is shown in figure 33b, with the size of grains under 1 µm.

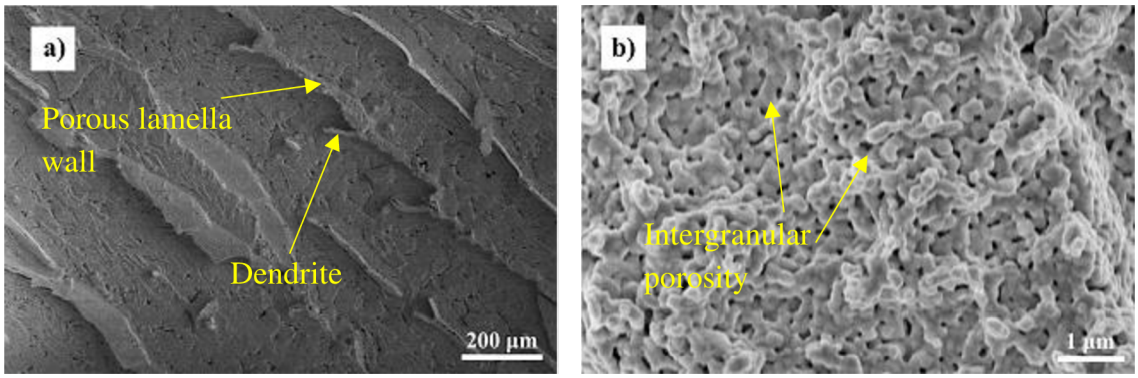

Figure 33: *Microstructure of sintered zirconia neural scaffold Zr_20_1200; a) interlamellar bridges, b) partially sintered zirconia particles.*

With the increasing sintering temperature, the lamellar walls became thicker (Figure 34a), which related to increasing the relative density. The narrower lamellar spacing could create more bridges during sintering and promote shrinkage between adjacent ceramic walls, resulting in lower porosity. The significant difference was in grains' appearance. The grains were more aggregated (Figure 34b) with no apparent intergranular porosity than sample Zr_20_1200. The lamella wall was denser. The grain size was in the range of 2–7 µm. It was reflected in the higher mechanical stability as the samples sintered at 1200 °C had.

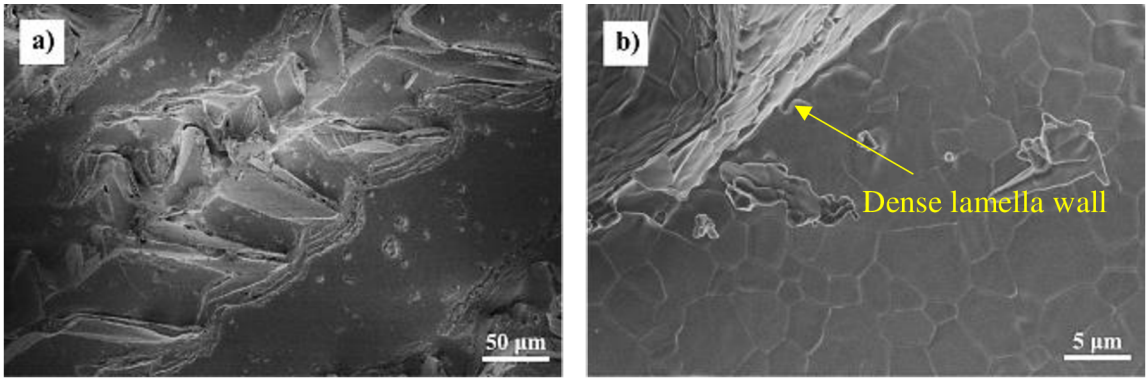

Figure 34: *Microstructure of sintered zirconia neural scaffold Zr_20_1550; a) lamella with interlamellar bridges, b) sintered zirconia particles.*

The freezing with a lower freezing rate gave rise to the dendritic structure of ceramic lamella walls. In the sample Zr_20_1550, the diversity of interlamellar bridges was present. The ceramic wall was denser with no visible porosity inside of lamella walls. There was a large amount of dense interlamellar bridges, according to figure 35.

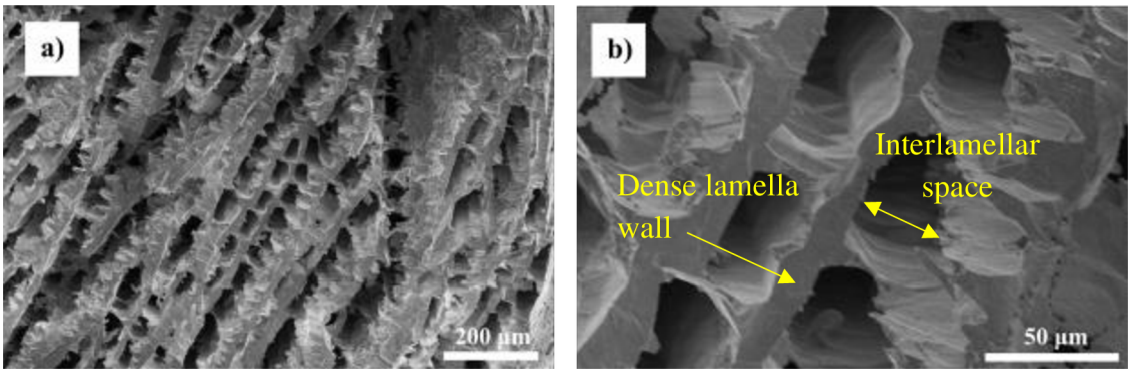

Figure 35: *Lamellar system of Zr_20_1550 sample; a) top view on lamellar system, b) detailed view on interlamellar bridges.*

Samples prepared by freeze-casting in liquid nitrogen

The neural scaffolds should have an interlamellar distance of 10–30 µm. To achieve this property, samples were frozen in liquid nitrogen with higher freezing-front velocity. Figure 36 shows SEM micrographs of the yttria-stabilized zirconia samples Zr_N_1200. If the freezing rate increased, the ice front velocity enhanced while the distance between lamellar structures reduced. The presence of a lamellar system was observed in figure 36a. The uniform grains with a size under 1 µm are shown in figure 36b with considerable intergranular porosity.

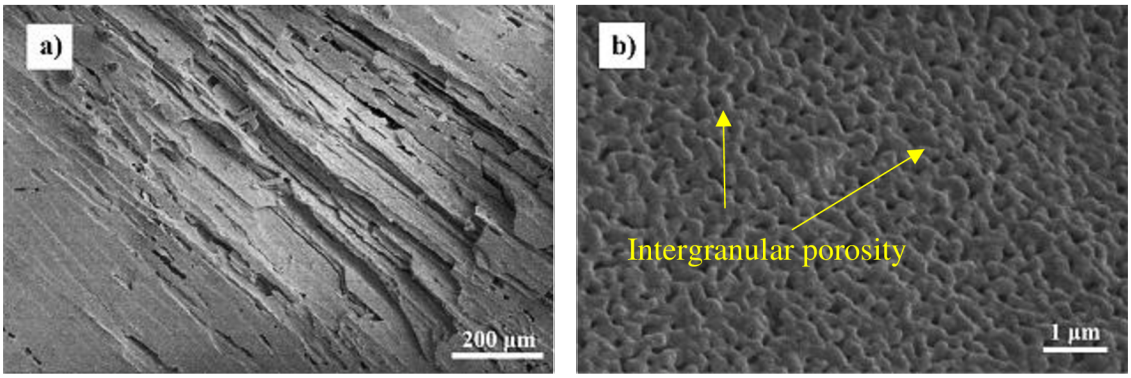

Figure 36: *Micrographs of the sintered zirconia scaffold Zr_N_1200; a) lamellar system, b) intergranular porosity.*

The growth of the grains strongly accompanied the densification of yttria-stabilized zirconia. The sintering temperature affected the aggregation of grains, which was correlated to the lower porosity, and higher density. It was also observed with SEM micrographs, where it is possible to see differences in grain size and diameter (Figure 36b and Figure 37b). The lamellar system of Zr_N_1550 was much denser than the porous lamellar system in sample Zr_N_1200. The densification is connected to higher mechanical properties.

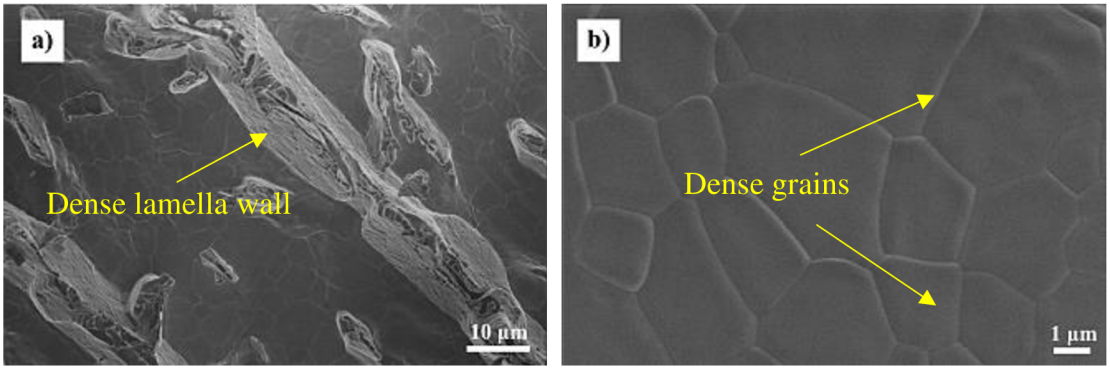

Figure 37: *Micrographs of the sintered zirconia scaffold Zr_N_1550; a) lamellar system with interlamellar bridges, b) detailed view on grains.*

The top view of the Zr_N_1550 sample revealed a lamellar system perpendicular to the cooling rate in an ice-growth direction (Figure 38a). The lamellar system was partially homogenous. There was a present site with bigger interlamellar distances. As it is possible to see, the growth of the ice was not parallel, but it grows irregularly, but always in the direction of the ice front.

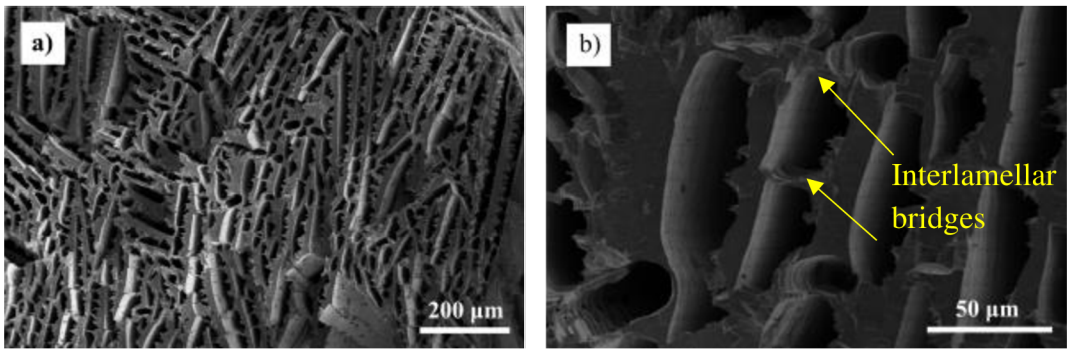

Figure 38: *The top view on interlamellar system of Zr_N_1550; a) irregular lamellar system, b) detailed view on interlamellar bridges.*

5.2.2 Mechanical properties

The mechanical properties of TZ-8Y samples were determined by flexural stress, concretely by a 3-point bending test. An amount of 30 samples was tested with samples sintered at a temperature of 1550 °C (Zr_20_1550 and Zr_N_1550). Samples sintered at 1200 °C showed low mechanical stability during manipulation. The comparison of the sintered scaffolds is shown in figure 39.

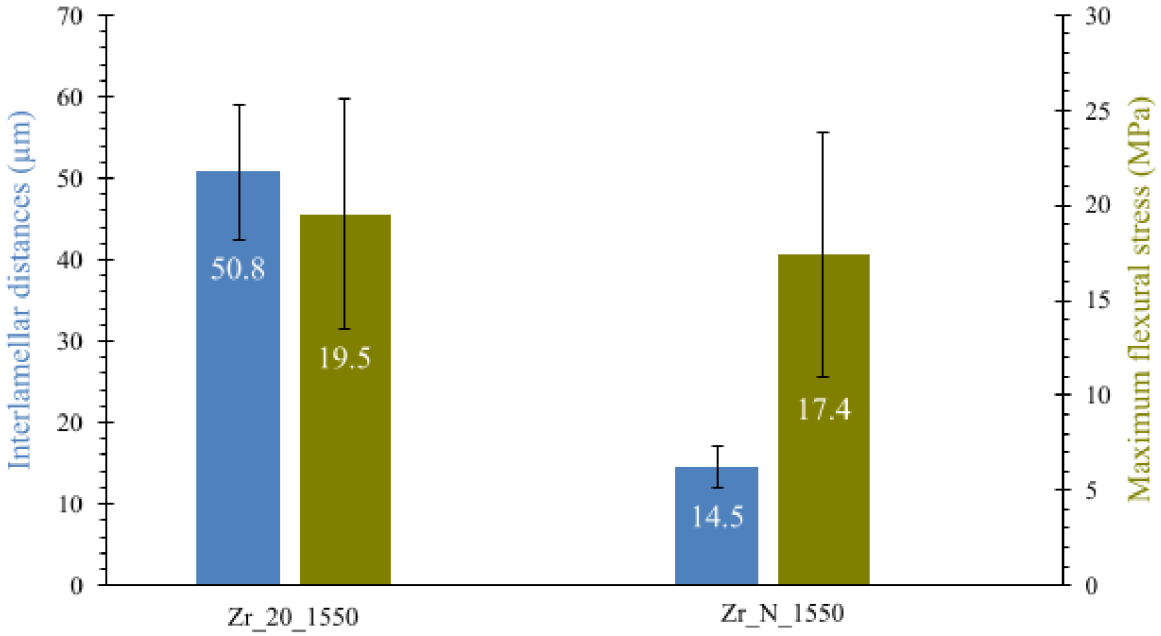

Figure 39: *A dependence of interlamellar distances on the maximum flexural stress of manufactured TZ-8Y scaffolds. The blue columns represent interlamellar distances, and the green columns are values of applied maximum flexural stress.*

Both types of prepared samples had high porosity values ~64 %, and their mechanical resistance was outstanding. The porosity and interlamellar distances of TZ-8Y scaffolds had no compelling impact on mechanical tolerance. The flexural strength of the Zr_20_1200 sample was 19.5 ± 6.1 MPa, where the lowest value was 5 MPa and the highest 28 MPa. The flexural strength of CaP_N_1200 was 17.4 ± 6.4 MPa. The highest measurement was 35 MPa, and the lowest value was 3 MPa. According to the measurements, the results are very similar, and the existence of a dependence of interlamellar distances on the maximum flexural stress was not confirmed. Higher sintering temperatures could cause these results because grains were very dense and similar in both samples. Probably, if the more suitable sintering temperature was set, the dependence will be observed. Another possible theory is that the proportion of lamella thickness to lamellar distance was very high in Zr_20_1550. Samples could have many supporting points, and there were many interlamellar bridges too, which increased mechanical stability.

5.2.3 Biological properties

Bioactivity testing in simulated body fluid

The apatite formation on the surface of the ZrO_2 hydrogel scaffold can be observed when it is implanted into the human body. Zirconia ceramics have attractive properties, such as high mechanical properties for biomedical applications. According to the study, Uchida et al. demonstrated that zirconia ceramics do not bond to the living bone except zirconia gels [88]. However, Quan et al. used 8% yttria-stabilized zirconia in SBF testing, and the apatite formation was present after seven days [89].

Pure zirconia has poor ionic conductivity and has a cubic structure only at 2300 °C. To stabilize the cubic structure at lower temperatures and to increase the concentration of oxygen vacancies, which results in ionic conduction via vacancy hopping, the doping is usually performed with yttria [90]. At actual materials, the formation of peroxide-group (O_2^{2-}) is more favourable than delocalized hole states.

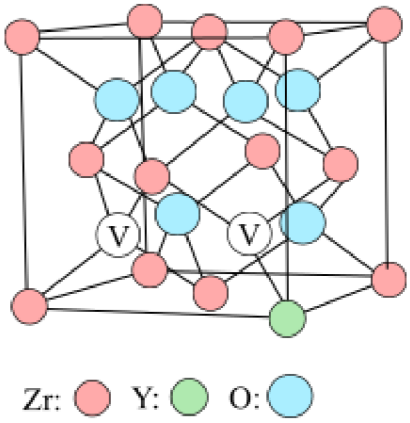

Figure 40: *Defect crystal structure of yttria-stabilized zirconia; V means vacancies [90].*

The TZ-8Y scaffolds were soaked in SBF for 21 days. Samples were weighed before soaking m_B, and after soaking m_{SBF}. The weight change was determined to investigate the formation of an apatite layer on the samples soaked in simulated body fluid. Table 13 follows that the weight of samples after soaking in SBF increased due to the formation of the apatite layer.

Table 13: *Results of TZ-8Y scaffolds soaked in SBF.*

Label	m_B (g)	m_{SBF} (g)	Weight change (%)
Zr_20_1550	0.0992	0.1020	+ 2.8 %
Zr_N_1550	0.0445	0.0468	+ 5.9 %

The iso-electric point of yttria-stabilized zirconia in water is between 4 and 11 pH. Therefore, the YSZ can reveal the negative surface charge by exposing the hydroxyl group obtained from SBF carbonate ions and the crystal structure vacancies. The negative surface charge interacted with the positive Ca^{2+} ions from SBF solution with the formation of a Ca-rich layer (calcium zirconate, CZ). With the increase of the positive charge of YSZ, it interacts with negative ions

PO_4^{2-} contained in SBF forming Ca-poor layer (calcium zirconium phosphate, CZP). Thermodynamically, apatite is more preferred. Therefore, it can be observed with SEM analysis. The possible process of apatite formation in YSZ ceramic is shown in figure 41.

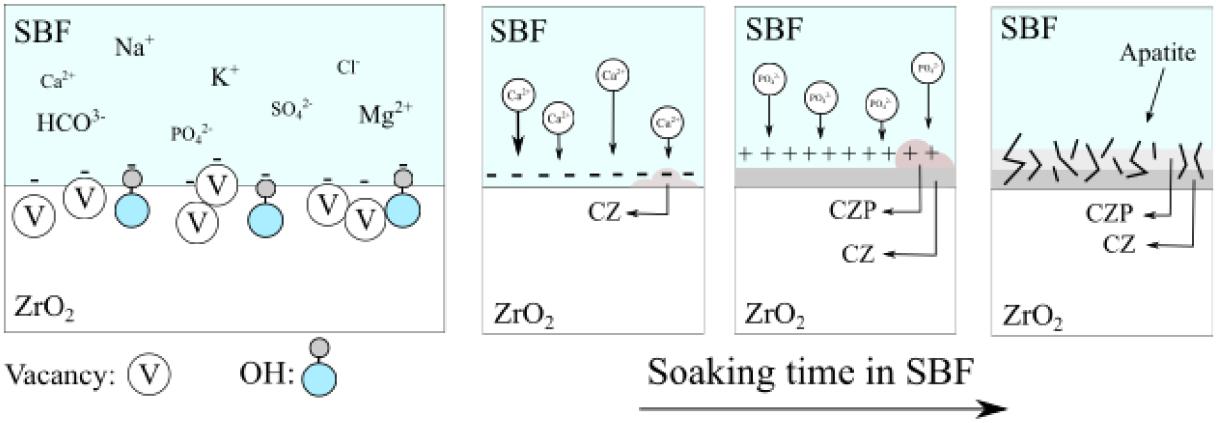

Figure 41: *Process of the formation of an apatite layer on the surface of YSZ scaffolds. Figure is inspired by reported surface behavior in [88, 89, 90].*

The SEM analysis of the cauliflower structure was only investigated with the samples frozen in liquid nitrogen. The cauliflower structure was observed alternately on the lamellar system, which is possible to see in figure 42. The lamellar surface was overgrown with nano crystallized cauliflower structures.

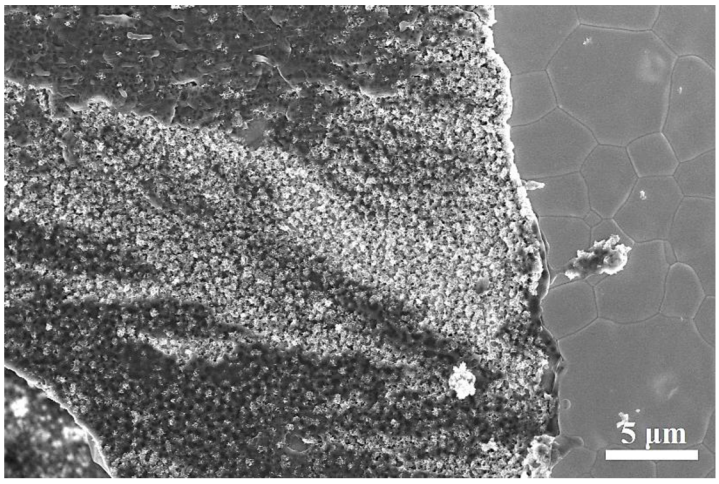

Figure 42: *Crystallized cauliflower structures in YSZ (TZ-8Y) samples frozen in liquid nitrogen.*

Cytotoxicity of zirconia ceramic powders

Zirconia is considered to be non-cytotoxic and bioinert in contact with the host tissue. The cytotoxicity of the zirconia powders was evaluated with an MTT assay for confirmation of this statement. Two types of YSZ powders were chosen for zirconia cytotoxicity evaluation: 3% yttria-stabilized zirconia powder (ZirPro, CY3Z) and 8% yttria-stabilized zirconia (Tosoh, TZ-8Y).

In figure 43, it is possible to see a very similar trend of cytotoxicity behaviour. Lower concentrations had a positive effect on cell viability. Viability values were over 100% in all cases. The higher concentrations showed considerable cell behaviour: CY3Z powder had

viability values about 90 %, TZ-8Y had about 70 %. The neural cells produce electrical impulses, TZ-8Y scaffolds have electrical responses due to the more vacancies in crystal-grain structure. For this reason, despite the lower viability of Schwann cells values, the TZ-8Y was chosen for further biological and mechanical testing.

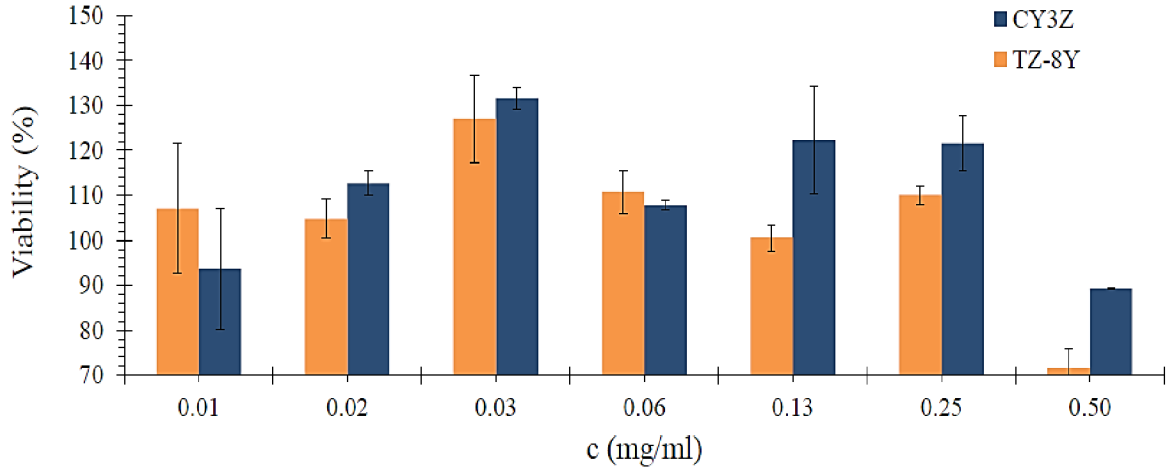

Figure 43: *Viability dependence of Schwann cells on increasing zirconia powders concentration in SBF medium.*

Biocompatibility of zirconia neural scaffolds with Schwann cells

A similar cultivation process with CaP scaffolds was carried out with zirconia TZ-8Y scaffolds sintered at 1550 °C. After 48 hours, the adhesion and infiltration of cells into the lamellar system were checked with a confocal microscope and scanning electron microscope. Both zirconia scaffolds had a small amount of adhered cells on the surface, and no cell was found inside the lamellar system. The cells had not elongated shape. They only adhered to the surface. The elongated shape represents the growth in the lamellar direction. Nevertheless, the shape is not elongated. The cell was not under stress and grew sprawled on the surface.

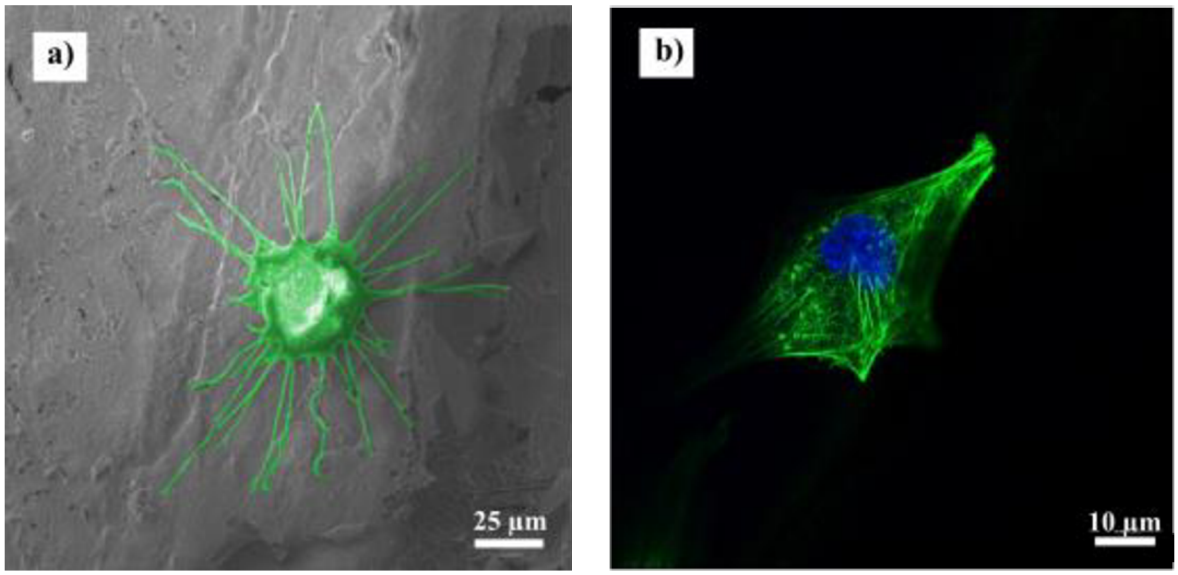

Figure 44: *Adhered cells on scaffold Zr_20_1550; a) adhered Schwann cell taken by SEM, b) photo taken by confocal microscope.*

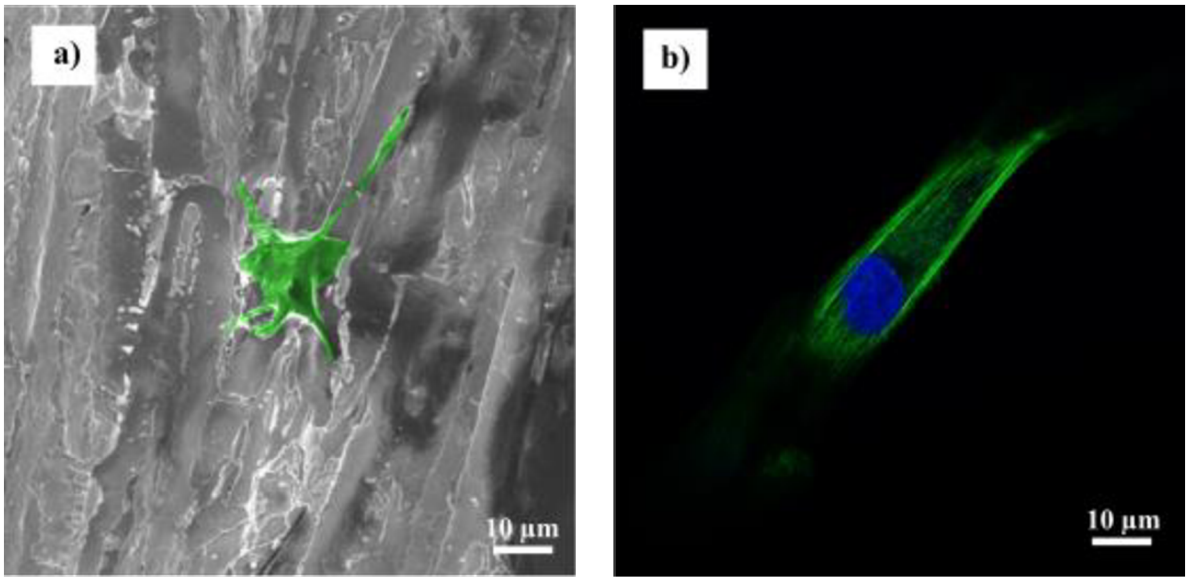

Figure 45: *Adhered cells on Zr_N_1550 scaffold; a) micrograph od Schwann cell observed by SEM, b) elongated shape of Schwann cell taken with a confocal microscope.*

The TZ-8Y samples did not have bioactive properties compared to other materials. It was hard to find living cells. Sample Zr_N_1550 contained smaller adhered cells with aggravated structure (Figure 45a). It is possible to see white structures in the image, which were not observed with a clean sample. Under a confocal microscope, only one living cell was observed with an elongated shape (Figure 45b), which could be related to growth in the lamella direction. Even though this phenomenon was presented, the number of living cells was the lowest compared to the other materials.

5.2.4 Summary of Chapter 5.2

The four types of TZ-8Y scaffolds were prepared with different grain morphology and lamellar system – scaffold frozen with controlled thermal gradient (Zr_20_1200) and scaffold frozen in liquid nitrogen (Zr_N_1200), where both were sintered at 1200 °C; and the scaffold frozen with controlled thermal gradient (Zr_20_1550) and in liquid nitrogen (Zr_N_1550) sintered at 1550 °C. The interlamellar distances changed fundamentally with the freezing rate but also with higher sintering temperatures. The sintering temperature shrank the samples by decreasing the interlamellar system by about 10 µm. The samples Zr_N_1550 had required interlamellar distances with appropriate mechanical properties (17.4 ± 6.4 MPa). For mechanical properties, Zr_20_1550 and Zr_N_1550 were chosen due to their higher mechanical stability during manipulation. The results of applied maximum flexural stress were exemplary. For sample Zr_20_1550, the value was 19.5 ± 6.1 MPa. The sintering temperature impacted the porosity values; with the increasing sintering temperature, the porosity decreased. The most significant impact of sintering temperature was on the grains, which were reflected in mechanical properties. At the temperature of 1550 °C, the samples Zr_20_1550 and Zr_N_1550 had more aggregated grains, without intergranular porosity, which was reflected in gained mechanical stability. When the sintering temperature was at 1200 °C, the intergranular porosity was higher, and the sample did not hold tight together.

The 8% yttria-stabilized zirconia scaffolds can exchange ions in a solution, thanks to the defect in crystal structure and the revelation of hydroxyl units. When the pH of the surrounding is between 4–11, the hydroxyl in the structure could reveal the negative surface charge by exposing hydroxyl units and vacancies and interact with calcium and phosphate ions in solution. This fact was determined with testing in the SBF solution, where the multiple apatite cauliflower structures were observed in the sample Zr_N_1550 (Figure 42). This fact caused higher calcium levels and was harmful to the Schwann cells. The TZ-8Y sample was fatal for neural cells in the highest concentration (Figure 43). The apatite was formed in larger quantities on the scaffold surface. It is related to a higher concentration of calcium ions on the surface and around the scaffold in media solution. In the SEM micrographs from observation of adhered Schwann cells, the apatite formation was not observed. Only minor surface abnormalities were presented (possible nucleation centers). It is possible to count with the charging of the surface and attraction of calcium from media, and the origin of nucleation centers. From the SEM micrographs, it was possible to observe that cells did not want to grow in the lamella direction; they only adhered to the surface.

5.3 Titania neural scaffolds

5.3.1 Microstructure

Titania neural scaffolds were prepared by freezing in liquid nitrogen and sintered at 1200 °C for 2 hours (Ti_N_1200). The porosity of sintered green-body can be seen in table 14, also interlamellar distance. The porosity values were shallow compared to CaP and TZ-8Y samples, caused by using titania nano-powder. The interlamellar distances were in the range for the neural scaffold.

Table 14: *Average interlamellar distances, relative density, and porosity of sintered titania scaffolds.*

Label	Freezing rate (µm/s)	Interlamellar distance (µm)	Lamellar thickness (µm)	Porosity (%)
Ti_N_1200	21.61 ± 3.08	15.6 ± 2.5	14.5 ± 1.5	51.9 ± 3.9

Scanning electron micrograph showed unidirectional regular lamellar morphology inside the scaffold with the presence of numerous interlamellar bridges (Figure 46a). The freezing in liquid nitrogen gave rise to a thicker lamellar system with multiple interlamellar spaces. A detailed view of the lamella is shown in figure 46b. The lamella consisted of irregular particles, where the smaller ones surrounded the larger ones. The lamellas were also porous, where micropores in lamella were observed, but the bonding between particles was strong. The lamellar shape was distorted in some sections. The distortion was caused by a higher sintering temperature, as titania requires. The average interlamellar distance was about 19 µm.

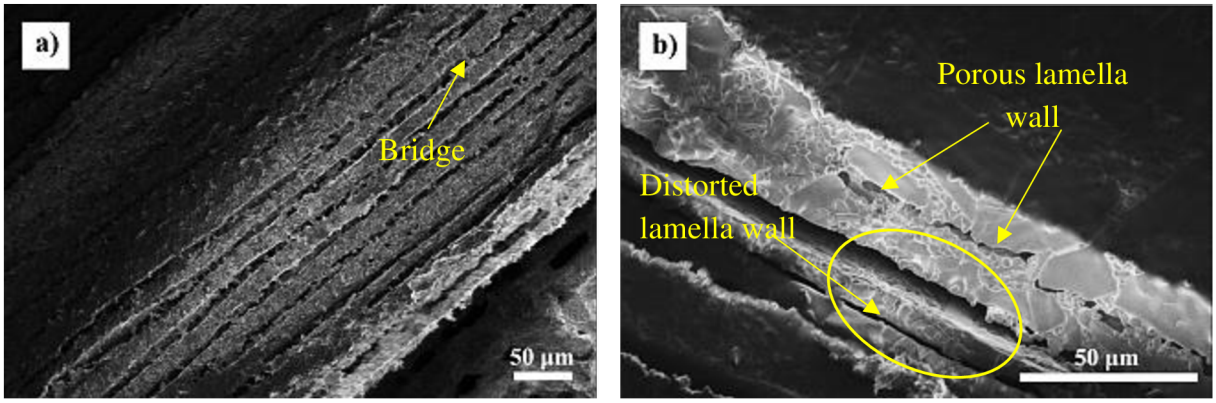

Figure 46: *Micrographs of the sintered titania scaffold Ti_N_1200; a) lamellar system, b) intergranular porosity.*

The lamellar system was perpendicular to ice growth with a dendritic structure (Figure 47a). There was not present typical lamellar shape at the top of the sample, as for CaP samples. The shape of the interlamellar system was more oval. There were present other open pores connected between large unidirectional lamella because tiny branch-like ice-crystals also grew, deviating from the main direction of the thermal gradient. The titania nano-powder contains non-uniform particles from the factory. Sintered grains had small dimensions around 2 µm, and larger grains up to 7 µm with apparent intergranular porosity.

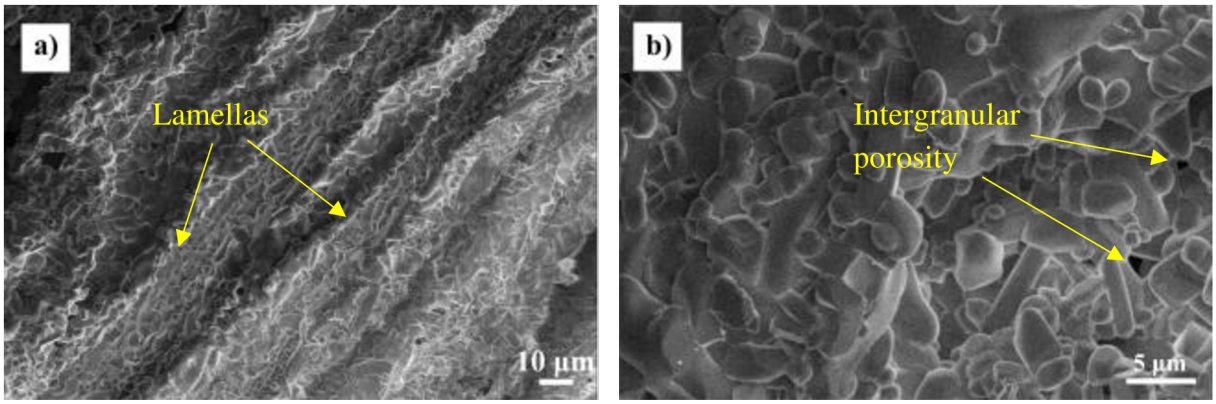

Figure 47: *Micrographs of sintered Ti_N_1200 samples; a) cross-view on the lamellar system, b) detailed view on particles.*

5.3.2 Mechanical properties

The flexural stress of the Ti_N_1200 sample was 17.2 ± 12.7 MPa. The standard deviation was very high because nanopowder tends to rapid sedimentation. Due to this fact, the porosity is nonhomogenous in the whole sample. Also, the distortion of lamella walls was observed, which decreased mechanical stability. The maximum flexural strength was 78 MPa, and the minimum was 1 MPa.

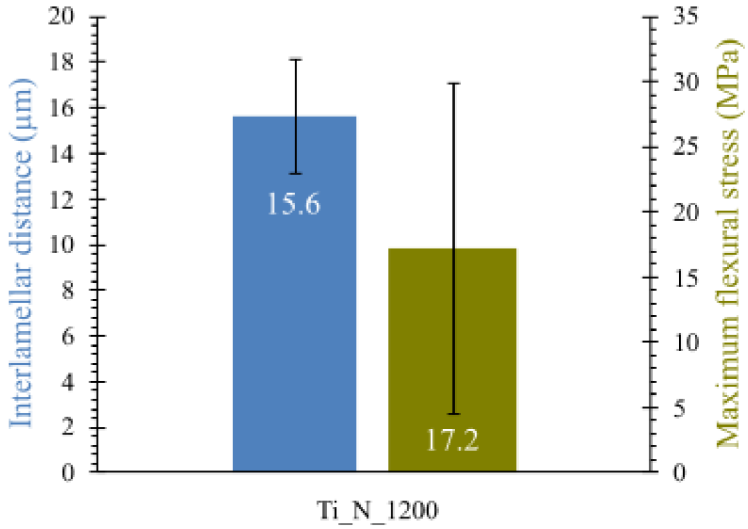

Figure 48: *A dependence of interlamellar distances on the maximum flexural stress of manufactured titania scaffolds.*

5.3.3 Biological properties

Bioactivity testing in simulated body fluid

Titania and its alloys have been successfully used in bone tissue engineering to form a dense amorphous layer on the titania surface, separating titania and bone tissue. SEM analysis showed that titania powders could induce the nucleation and growth of apatite on the surface [92].

The titania scaffolds were soaked in SBF for 21 days. Samples were weighed before soaking m_B, and after soaking m_{SBF} to determine the apatite growth on their surface. The results are shown in table 15. The weight increased by 3.7 %, and apatite formation was expected.

Table 15: *Results of titania scaffolds soaked in SBF.*

Label	m_B (g)	m_{SBF} (g)	Weight change (%)
Ti_N_1200	0.0536	0.0556	+ 3.7 %

The Ti-OH groups are charged to $Ti\text{-}O^-$ and $Ti\text{-}OH^{2+}$ in a pH range of 7.25–7.40 in the SBF solution. In this model, both groups are active sites and welcome calcium and phosphate ions together. The well-organized regions (pre-embryos) are formed. Pre-embryos are less stable, and it is hard for them to differentiate into the embryos and nuclei. Otherwise, they will decompose and dissolve into the SBF. However, a few pre-embryos survive compared to trillions of atoms on the surface and are formed into the embryos and crystallized into the appetite [93]. The possible mechanism is shown in figure 49.

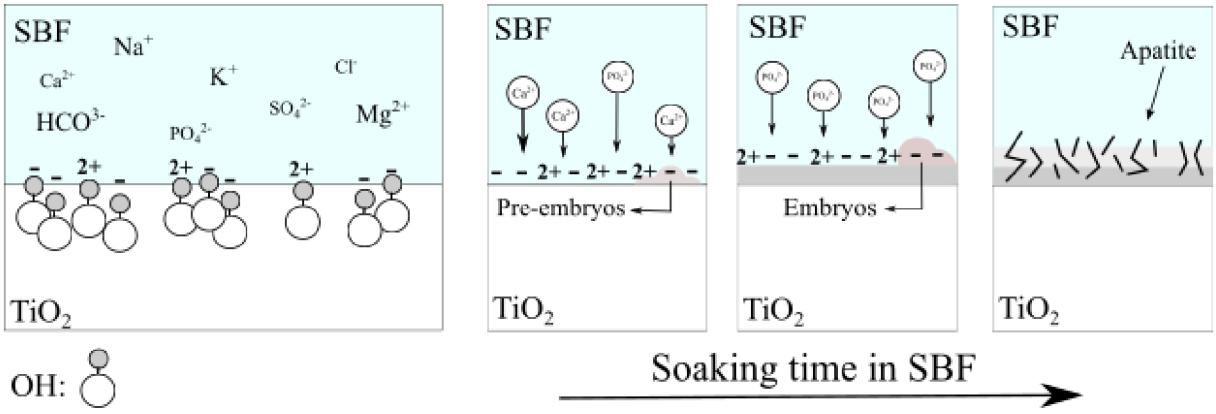

Figure 49: *Process of the formation of an appetite layer on the surface of TiO_2 scaffolds. Figure is inspired by the detailed description reported by Hayakawa et al. [93].*

Figure 50 shows the SEM photograph of the surface of the titania neural scaffold after its exposure to simulated body fluid for three weeks. The formation of new morphologically different structures is visible on the surface. The structures morphologically look like apatite nucleation centers. The typical cauliflower structure was not observed on the whole sample. It was possible to see different grain structures, which were more irregular. It was assigned with the formation of embryos surface, probably calcium titanium phosphate (CTP).

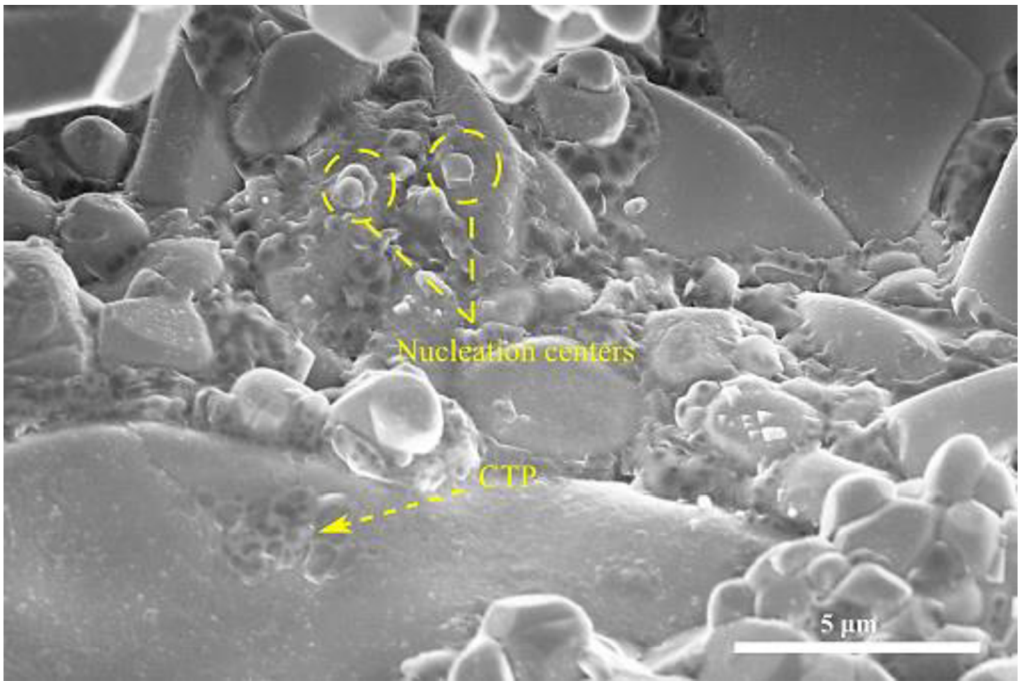

Figure 50: *Apatite nucleation sites with amorphous CTP layer on TiO_2 scaffolds.*

Biocompatibility of titania neural scaffolds with Schwann cells

Titania was the last material where the biocompatibility with Schwann cells was observed. This material showed outstanding results. The titania nano-powder had, after sintering irregular shapes of grains, which supported the possibility for adhesion of the cells. The cell morphology was in good condition. The fibers from cells were spread in several directions and used correctly on the titania surface (Figure 51a). The cells could connect and grow inside the scaffold along the entire length (Figure 51b). The cells had an elongated shape, where the presence of growth in the lamellar direction was expected. The surface of the scaffold was illuminated with visible light, and the interlamellar ingrowth was confirmed.

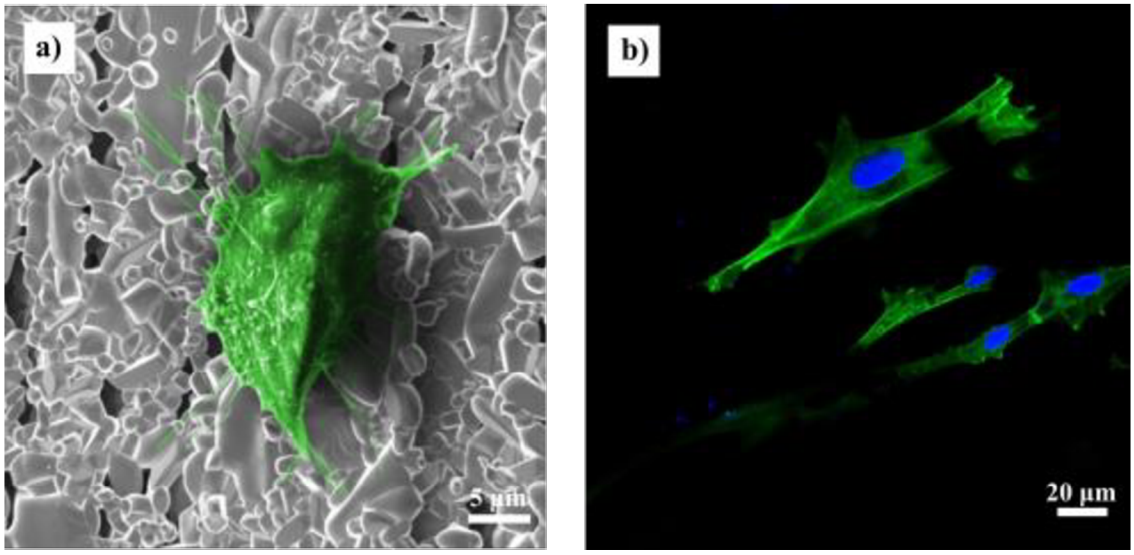

Figure 51: *Adhered cells on titania scaffold Ti_N_1200; a) adhered Schwann cell, b) interconnected Schwann cells in lamellar direction.*

5.3.4 Summary of Chapter 5.3

The titania neural scaffold was used for its bioinert properties in the studies for bone regeneration scaffolds and approval by FDA [54]. The scaffolds were prepared only by freezing in liquid nitrogen (Ti_N_1200) to achieve excellent interlamellar distances. It was possible to produce titania scaffolds with 52 % porosity values. During the sintering, the nano-powder did not sustain and aggregated into larger but heterogeneous particles, which is also one of the properties of a successful scaffold for nerve regeneration. The prepared scaffolds had mechanical properties ~17.2 MPa.

The titania can form a negative charge on its surface, thanks to the formation of hydroxyl groups in a pH 7.25–7.40. The apatite cauliflower structure was not observed, but nucleation centers and embryos were formed (Figure 50). The titania neural scaffold was made from the gentlest material to the Schwann cells. It had many grains where the cells could be adhered (Figure 51a), and the cells wanted to grow inside the lamellar system (Figure 51b), which had not been observed in such quantities yet.

6 DISCUSSION

6.1 Open questions from the literature review

This section of the thesis is focused on the discussion of obtained results in the context of the literature. Namely, microstructure, mechanical and biological properties are discussed for all used materials. The goal of the present investigation was to obtain *in vitro* indication of the capacity of a highly oriented bioceramic scaffold to perform two functions: acting as a cell carrier for implantation of axon-like cells and supporting the migration inside to the structure. Figure 52 points to a simple overview of crucial scaffold problems: oriented substratum, seeded support cells, and controlled release of nerve growth factors. The thesis is emphasizing the first two problems.

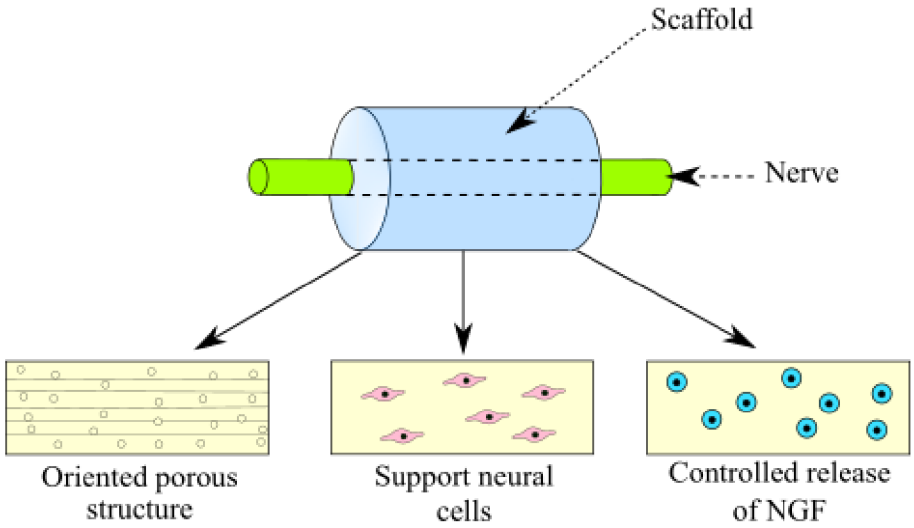

Figure 52: *Oriented bioceramic nerve scaffold, where the support of neural cells and controlled release of growth factors are guaranteed [7].*

We expect the following advantages of the bioceramics compared with the models presented in the literature:

- shape stability during the implementation and interaction with the living cells environment,
- defined chemical composition and bioactive behaviour,
- improved mechanical properties for small diameter scaffolds, but with length to bridge the gap.

6.2 Control of the microstructure

Regeneration of axons after spinal cord injury is vital for the recovery of the function of the nerve. The presented studies showed that materials, size, and morphology of scaffolds, type, age of neurons, and surface adhesion influence stimulation of neurites growth and neural repair. Bioengineered scaffolds guide the growth after the injury with linearly oriented growth. One of the principal methods to fabricate interconnected porous scaffolds with unidirectional channels is the freeze-casting method. The method provides a noteworthy improvement in physicomechanical features, controlling pore size distribution by cell size and designing

elongated pores to guide cellular proliferation and differentiation [37]. Freeze-casting has been used with several natural biomaterials (collagen, agarose, chitosan) for neural tissue engineering, where each scaffold showed different architecture [2, 38, 39]. In the freeze-casting method, the suspension is poured into PLA mold with PVC tubes. The solvent forms crystals in the vertical direction along the freezing direction, organizing a proper macrostructure for neural scaffolds. The freeze-casting process forms a lamellar system with interconnected pores via interlamellar bridges (Figure 53b). There exists optimum pore size or range for each distinct cell type. For neural cells, the value is in the range (10–30 μm) according to Wiering et al. [1]. It is necessary to utilize a uniform scaffold with similar pore distribution to obtain successful cell attachment.

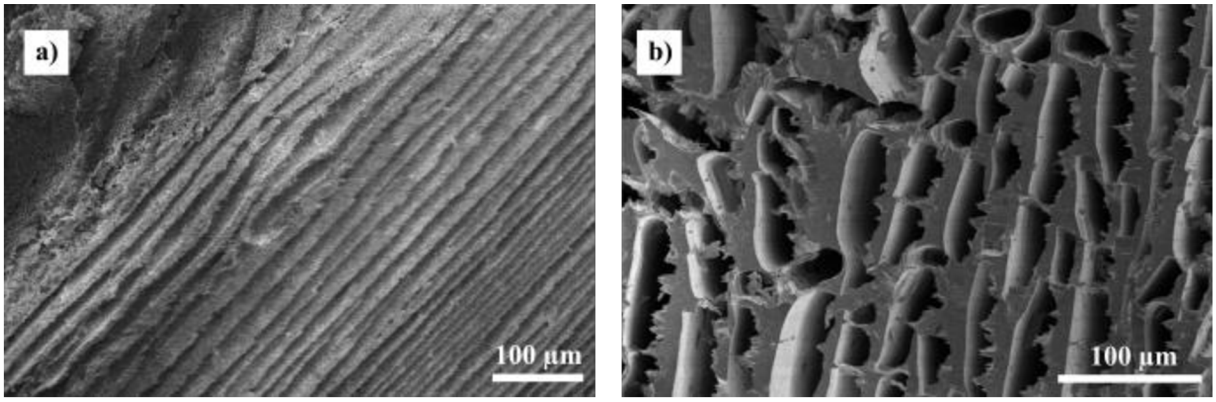

Figure 53: *SEM micrographs of achieved microstructure; a) linearly oriented Ti_N_1200, b)lamellar system interconnected by interlamellar bridges of Zr_N_1550.*

The manipulation of pore orientation, morphology, and surface topography is typically very limited by shaping techniques. However, freeze-casting allows using different mechanism control, in which structures can be tailored independently, including freezing rates. The right combination of experimental freezing conditions and suspension formulation allows the adaptation of scaffold on micro levels (the size and shape of the pores of the grain, the roughness of the lamellae surface) and the macro levels (distance of the lamella walls, interlamellar bridges) [73]. Macro levels features are shown in figure 53.

The prepared scaffolds had a 4 cm length with a diameter of 2 mm with various interlamellar distances. The surface of freeze-casted scaffolds possessed all microscale topographic features (curvatures, roughness, anisotropic microstructure). Cellular communication, transportation of oxygen and nutrients, removal of wastes, and cellular metabolism should be available by multiple lamellar systems obtained in all prepared samples.

Influence of freezing kinetics on interlamellar distances

The freezing rate influences the final relative density, which correlates to changes in porosity [3]. The minor differences between porosities showed that porosity decreased with the higher freezing rate, which relates to decreasing interlamellar distances. High-speed cooling rates resulted in the ice front trapping the particles and the formation of dense material, but only when the particles had a specific diameter (Ti_N_1200). Slower velocity resulted in the dendritic structure with lower density values.

The total porosity was independent of the cooling rate and was the same for CaP and ZrO_2 materials freezing with different methods (CaP_20_1200 vs. CaP_N_1200, Zr_20_1200 vs. Zr_N_1200 and Zr_20_1550 vs. Zr_N_1550).

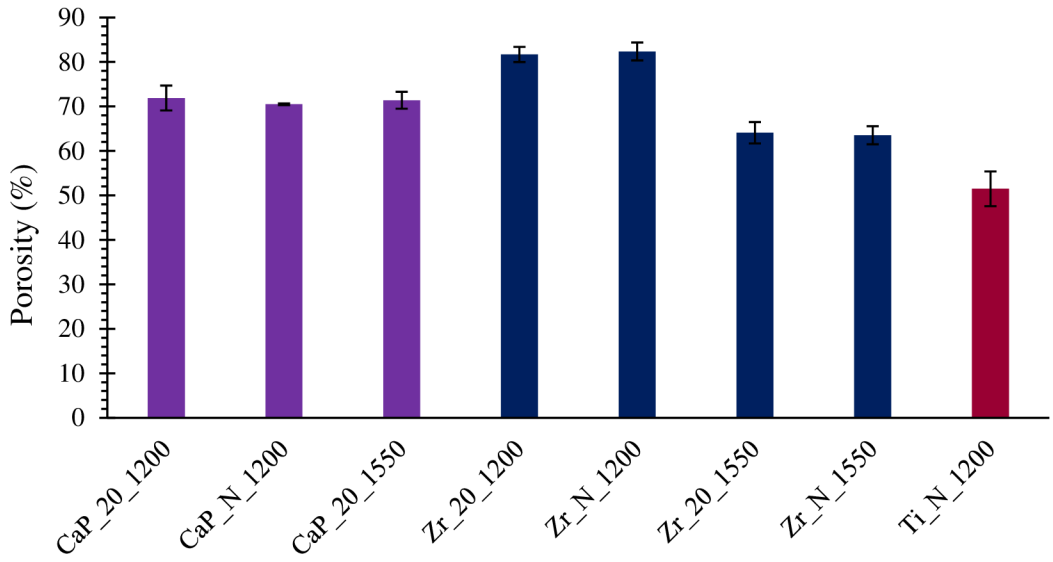

Figure 54: *The comparison of changes in porosity caused by freezing velocities.*

The samples possessed pores in lamellar shape, where they were replicas of the crystals, concretely water crystals. Ceramic particles were rejected by the moving solidification front, concentrated, and entrapped in-between ice crystals. This phenomenon was observed by Deville [3] and in all prepared samples. The freezing rate enormously influenced the diameter of ice crystal growth. The freeze-casting setup was defined with temperature gradient, where the freezing-front velocities were contrasting for different materials. The suspension was frozen in liquid nitrogen, which had the highest value of freezing-front velocities, but it was different again for various materials. All samples were frozen with unidirectional freezing to achieve a lamellar system perpendicular to the cooling. Extremely low velocities lead to a breakdown of lamellae formation resulting in a planar solidification front growth [69, 71].

According to Deville et al., when the freezing kinetics increases (the freezing-front speed increases), the width of the channels and lamellas are drastically affected (interlamellar distance decreases) [3, 68]. This trend was observed for all ceramic samples (Figure 55). The measured values of freezing rates for samples frozen with controlled thermal gradient were very similar (5–6 µm/s) with comparable interlamellar distances (50–60 µm). The samples frozen in liquid nitrogen had small differences in freezing rate values (22–28 µm/s), where small differences in interlamellar distances were observed. The CaP particles were calcinated, which caused roughening of particles. The sample had the lowest values of interlamellar distances, 12.6 ± 0.5 µm. Titania and zirconia powders had grain sizes under 100 nm, but interlamellar distances were higher. This result was caused by the different diameters of ceramic particles, which is connected to different solidification principles, concretely the capillary force [3].

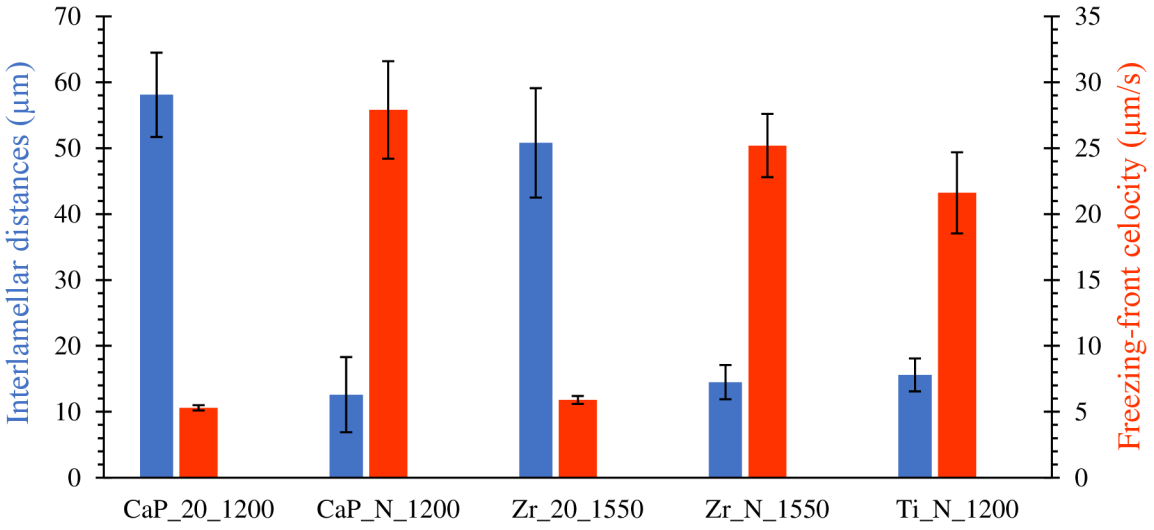

Figure 55: *The dependence of interlamellar distances on freezing-front velocity. With the higher values of the freezing rate, the interlamellar distances decreased.*

The freeze-casting method of the porous structure is a unique fabrication process. The neural scaffold with the diameter of pores 10–30 µm can be prepared only by increasing solidification velocity, which does not depend on used ceramic powder. The increasing freezing rate velocity can be provided by liquid nitrogen freezing. Homogenous freezing, where the pre-cooling of the copper ring is used, forms the interlamellar structure across the whole structure.

Influence of sintering temperature on microstructure

To determine the effect of sintering temperature on final scaffolds, the CaP samples were frozen with a controlled thermal gradient and sintered at 1550 °C (CaP_20_1550). Zirconia samples were sintered at two sintering programs – 1200 °C/2 h and 1550 °C/2 h. An ideal sintering temperature for full densification of CaP scaffolds is 1200–1250 °C and 1400–1600 °C for zirconia samples [91, 95]. For ceramic materials, sintering shrinkage can be significant for the average change in diameter, height, and volume [94]. The volume reduction was detected in comparison with zirconia samples. In these cases, the sintering shrinkage was observed by reduction of lamella thickness (Zr_N_1200 vs. Zr_N_1550), by reduction of interlamellar distances over 10 µm, or by a reduction in porosity ~20 %.

The sintering of CaP samples over recommended temperature does not result in a volume change but also results in phase changes. CaP scaffolds sintered at 1550 °C/2 h had smooth surfaces, where grains were not recognizable. A change in phase composition caused it when β-TCP was transformed to α-TCP. Sample CaP_20_1200 contained an increased amount Whitlockite (β-TCP) phase, as it was expected according to the literature [84]. CaP_20_1550 consisted of a high α-TCP amount, which was not present in the 1200 °C/2 h sample. The phase change was also possible to see by changing the sample color from white to blue. Changes in phase composition can be observed in figure 20.

Influence of interlamellar distances on mechanical properties

The mechanical behaviour of tissue-engineered scaffolds can be affected by their microstructure. The 3-point bending test was performed with CaP samples to confirm mechanical stability. According to the results, the total porosity did not influence the mechanical properties as the cooling rate did. The increase in freezing velocity leads to a reduction in pore (lamellar) size due to higher interface velocity and increased pore wall density. The same results were reported by Ghorbani et al. [96].

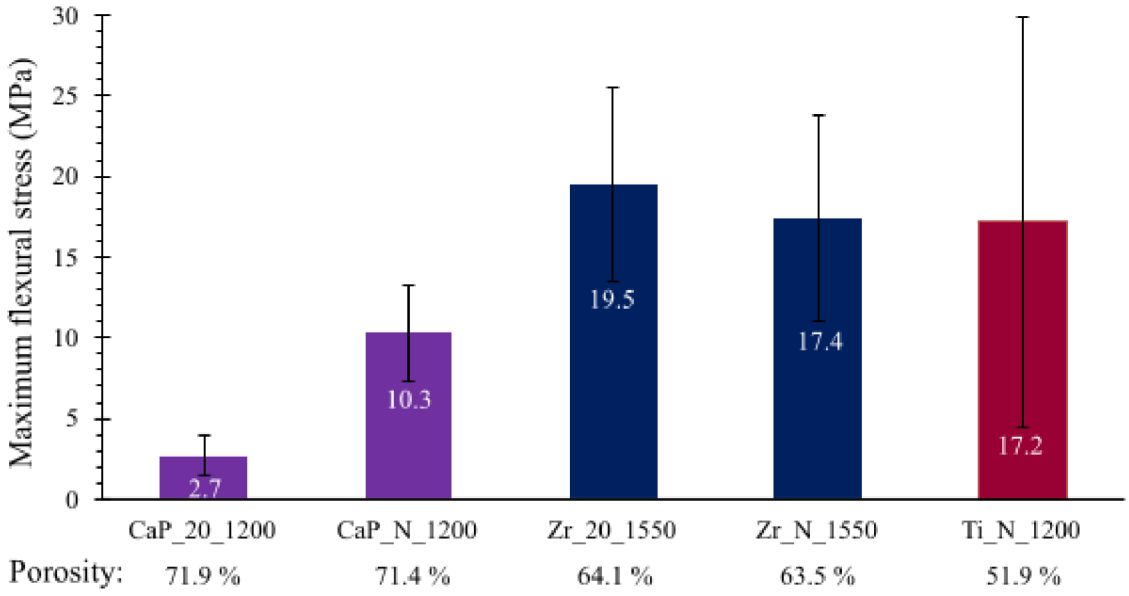

Figure 57: *Maximum flexural stress for all prepared samples with highlighted porosity values.*

Figure 57 shows the differences in flexural stress applied to the samples. CaP samples for low cooling rate (<6 µm/s), where the interlamellar distances were up to 50 µm, had flexural stress ~2.7 MPa. The flexural stress increased up to 10.3 MPa with a faster cooling rate (>20 µm/s). This effect is fully connected with the microstructural properties. Porosity size (defect size) decreases as the cooling rate increases so that the strength also increases as the defects become smaller. The influence of defects on compressive strength was explained by Deville et al. [68]. Mechanical test for sample CaP_20_1550 was not performed due to low mechanical stability during manipulation. The highest results were achieved for zirconia samples. The results were very similar. Also, the titania showed a similar outcome. Thanks to this example, it is possible to show how freeze-casting is an unpredictable, diverse method. Suspension composition, freezing rate, sintering temperature, etc., have a severe impact on resulting mechanical stability. However, zirconia samples behaved differently, which is connected to different solidification principles. The force between ceramic particles in zirconia suspension is stronger and obstructs the crystal from moving particles. The ice-crystal grows along with the particles, and the formation of interlamellar bridges occurs in more significant numbers. The different behaviour of several ceramic materials was reported by Scotti et al. [94].

6.3 Effect of freeze-casting on biological properties

The prepared freeze-casted scaffold obtained a whole spectrum of structure properties for the neural scaffold. However, freeze-casting does not allow precise control of pore size. Only the shape is defined by ice growth. This fabrication method resulted in highly stable scaffolds, where the cells' attachment was observed. It was necessary to observe several materials due to their cytotoxicity *in vitro* behaviour. The ambition of the presented thesis was to prepare calcium phosphate-based scaffolds, where the calcium ions would support axonal elongating, as Francis et al. demonstrated in their study [2]. Nagappan et al. described the positive effect of calcium ions, where the ions were involved as the initial part of the calcium influx. It sealed the axon and facilitated successful axon regeneration [83].

On the other hand, several studies described the negative effect of calcium ions on Schwann cells' survival. The increasing concentration of Ca^{2+} supported the reduction of cell numbers [86, 97]. In this study, the calcium ions had adverse to fatal consequences on cell survival (Figure 28). Hydroxyapatite-based materials are not suitable for Schwann cell cultivation in higher concentrations. All types of prepared powders had very similar cell viability. Non-sintered HAP (sample HAP) powder had approximately the same value for all concentrations. On the other hand, this type of hydroxyapatite is not free of impurities, which can cause inflammatory problems over time. CaP_20_1200 had the highest viability values for concentrations under 0.25 mg/ml. It could be observed that the only reason for the progressive reduction of cell viability was the increasing Ca^{2+} concentrations in the media and on the scaffold surface. With a high concentration of Ca^{2+}, the Ca^{2+} influx activates the phospholipases, endonucleases, and protease enzymes, which are the source of the cells' self-damage [86, 87]. Due to this fact, other freeze-casted scaffolds based on zirconia and titania were observed.

Apatite formation in simulated body fluid

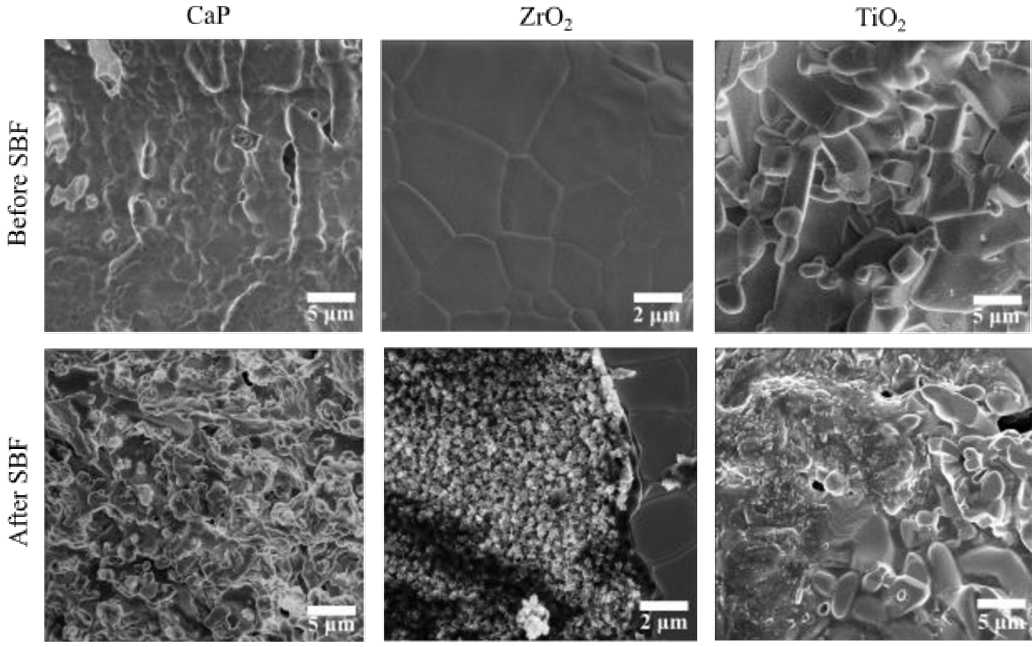

Figure 58: *The comparison of apatite formation after 21 days of soaking in SBF.*

The classic model of crystallization consists of two fundamental processes – nucleation and crystallization. When the calcium and phosphate units are adsorbed on the surface, the initial embryo state (prenucleation clusters) occurs. However, such a region cannot always grow into a nuclei state only if it is thermodynamically efficient. If the nuclei are formed, the crystallization is entirely driven [93].

The prenucleation centers and nucleation centers were observed in this thesis, all similar to abnormalities on agglomerates' surface regions. If the conditions were convenient, the nucleic states of calcium phosphates grew into the bone-like apatite, also called cauliflower structure. This structure was observed on the hydroxyapatite sample (CaP_N_1200) and zirconia sample (Zr_N_1200). The titania sample possessed only nucleation states. The behaviour of materials is fully connected to the material-solution relationship, concretely surface charging of used material. One new trend of neural scaffold design is to create a conductive platform that introduces external electrical stimuli to cells since electrical stimulation can affect the migration, differentiation, and proliferation of neural stem cells [31]. Due to this fact, the 8% yttria-stabilized zirconia samples were prepared. This material obtains the highest electrical conductivity from all used material, follows hydroxyapatite and titania. The electrical conductivity of materials can be seen as apatite formation on materials surfaces (Figure 58). The electrical properties of hydroxyapatite-based ceramic powders are described in detail by Das et al. [98]. After 21 days in the SBF medium, the zirconia samples formed many crystals close to each other. Hydroxyapatite samples possessed typical cauliflower structures, but only nucleic centers were observed in smaller numbers on titania samples. Posner and Betts described that only ~10 % of the clusters (nuclei centers) survive and are transformed to bone-like apatite. Titania is a less conductive material. The complicated mechanism of embryo formation was present, which relates to dissolution back to the SBF. Also, the nuclei centers were not stable [99].

The apatite layer contains a high concentration of Ca^{2+} ions. The probable reason for the worse survival of Schwann cells could be connected to the attraction of calcium ions to negatively charged materials' surfaces, which was verified by the SBF test. Hight concentrations of cauliflower structures reflected a high concentration of calcium ions on the surface, and the Schwann cells did not want to adhere and proliferate *in vitro* properly.

The freezing process affected the kinetics of the formation of the apatite layer. Namely, the sample frozen with a controlled thermal gradient (CaP_20_1200) formed only the nucleation sites after soaking for 21 days. The sample frozen in liquid nitrogen (CaP_N_1200) formed the Ca-rich ACP and Ca-poor ACP and apatite earlier. This fact indicates that samples frozen with liquid nitrogen having higher surface area exposed to the air may have also a more negatively charged surface.

Cell-scaffold interactions

The scaffolds were cultivated with Schwann cells and visualized with SEM to understand the cell morphology and cell interactions on the 3D scaffold. After two days of cultivation, some of the Schwann cells were observed outside and inside the scaffold. The porous scaffolds are not designed only as cell carriers but also allow the diffusion of waste and nutrients to

remain viable cells. The highly porous freeze-casted scaffolds were prepared with the required properties. The highly connected scaffold was hardly observed due to probable interactions in all three dimensions. The photos of scaffolds were taken from the surface and the one breaking point. However, there were apparent differences between the orientation and adhesion on scaffolds.

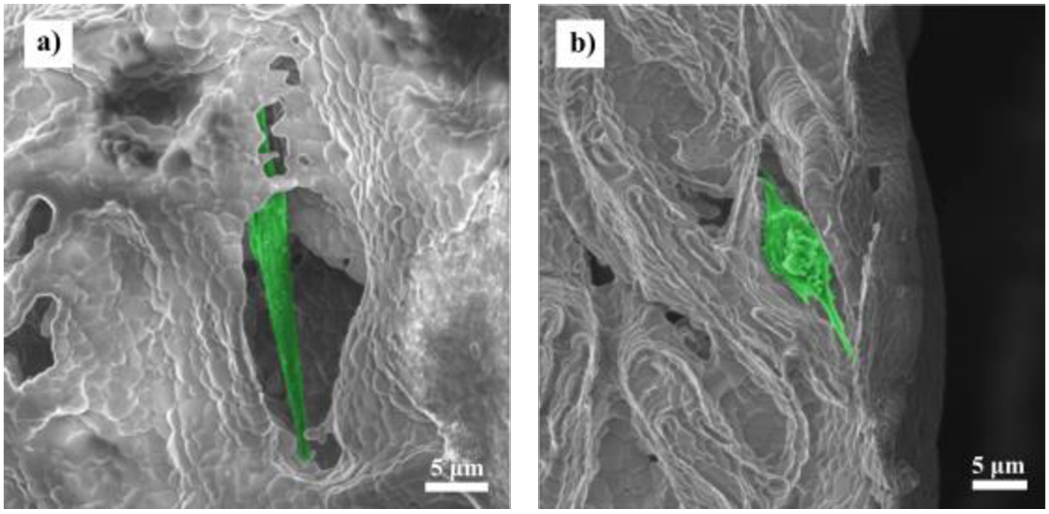

Figure 59*: The SEM micrographs of sample CaP_N_1200; a) elongated cell inside of the lamellar system taken from surface observation, b) adhered cell inside of the structure.*

The default scaffold was CaP_N_1200 with appropriate microstructure and mechanical properties for neural applications. The Schwann cells wanted to infiltrate into the whole structure, and they used the whole structure's macro and micro properties. They were bridging the lamellar system (Figure 59a) and adhered to the dendritic structures (Figure 59b). It was demonstrated that *in vitro* cytotoxicity tests were not appropriate for larger scaffolds, and cell survival was utterly different. However, the 48 hours of cultivation were less than the cells needed. Mollers et al. pointed that four weeks of cultivation are necessary for oriented scaffolds [38]. However, after 48 hours, the cells had already adhered to the surface in all samples, and some penetrated inside of the structure. It has been observed that small-diameter profiles (10–20 µm) promoted better orientation of cells (samples CaP_N_1200 and Ti_N_1200), which was expected according to [1, 38]. The smaller pore showed a positive effect on cell adhesion, and the bigger ones realized the cell penetration. However, the effect of anisotropic microstructure should not be ignored. The unidirectional pores provide guiding channels for growth.

According to the SEM photos, the cell migration and spreading of the cells were better in CaP_N_1200 scaffolds, but cell adhesion was observed in samples Zr_N_1550 and Ti_N_1550 (Figure 60). The intergranular porosity helped cells bridge the lamella wall and allowed cells to grow throughout the open porous structure (Figure 60b). The elongated shape of cells was observed by a confocal microscope with titania samples also.

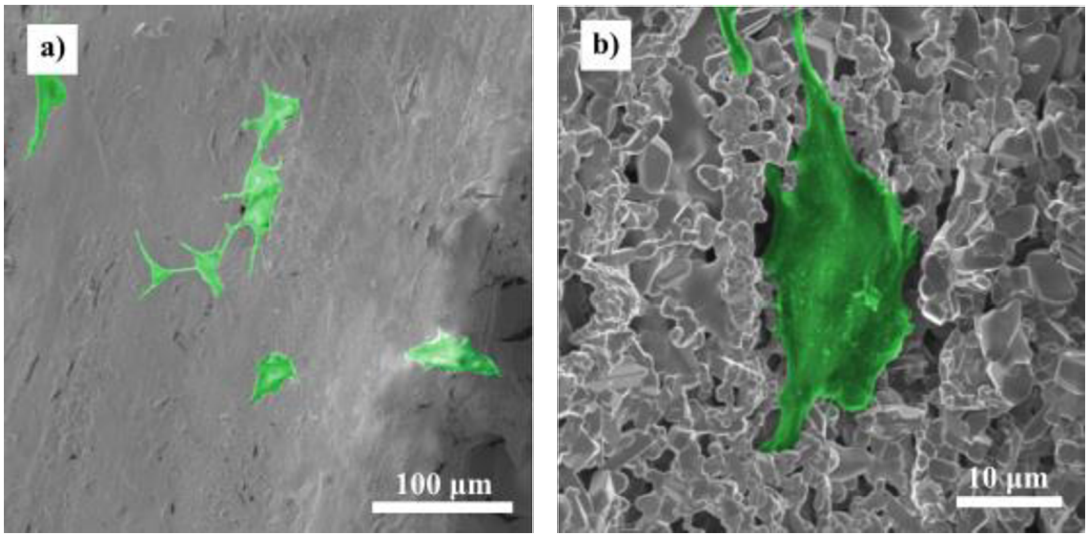

Figure 60*: Different types of adhesion on scaffold´s surface; a) smooth dense surface of Zr_N_1550; b) the porous surface of Ti_N_1200.*

In this thesis, it was shown that calcium phosphate and titania scaffolds support cell attachment and directionally oriented growth of Schwann cells *in vitro*, which are viable as a substrate with outstanding mechanical properties for neural regeneration.

7 CONCLUSION

The highly oriented porous scaffolds with unidirectional porous distribution prepared by the freeze-casting method were successfully tested. The CaP, ZrO_2, and TiO_2 materials were used to prepare scaffolds with required micro (size and shape of pores, lamella roughness) and macro features (distance of lamella walls, interlamellar bridges).

Among all the neural scaffolds' fabrication methods, freeze-casting provides open pores along the whole structure (4 cm) with a lamellar shape, which is necessary for neural tissue engineering. The size of interlamellar distances is possible to minimize by increasing of freezing front velocity to achieve the required lamellar distances of neural scaffolds (10–30 µm). When the freezing rate is lower, the ice-crystal growth is supported, giving rise to a lamellar system with larger distances between lamellas (50–63 µm). The interlamellar distances decrease when the freezing rate increased (12–16 µm). An increase in freezing rate showed better mechanical properties due to a reduction in pore (lamellar) size and an increase in the density of pore walls. Freezing with a controlled thermal gradient showed that the flexural strength of CaP samples depends on interlamellar distances. CaP_20_1200 had maximum flexural stress of 2.7 ±1.2 MPa with interlamellar distances 58.1 ± 6.4 µm, and CaP_N_1200 had a flexural strength of 10.3 ± 3.1 MPa with interlamellar distance 12.6 ± 3.5 µm. The obtained mechanical properties were very high for samples frozen in liquid nitrogen. All values were up to 10 MPa, and concretely the highest value achieved Zr_N_1550 (17.4 MPa).

The procedure of scaffold biocompatibility testing was successfully developed. For the scaffold testing, it is necessary to use a high suspension concentration of Schwann cells for successful cell attachment on the surface of the scaffold. The directionality of Schwann cells' growth was somewhat random and poorly oriented with present adhesion. However, the scaffolds based on calcium phosphates (CaP_N_1200) and titania (Ti_N_1200) supported the linearly oriented growth *in vitro*. During the testing, a harmful influence of calcium ions was observed with CaP scaffolds. The CaP can be found in several phases, including soluble α-TCP. This phase causes a release of Ca^{2+} inside of the media. CaP_20_1550 obtains this phase. All used materials have properties to interact with the medium by exposing hydroxyl units (CaP also exposes phosphate units). It is an attractive feature in the context of bone tissue engineering. However, it was found by testing in simulated body fluid that this charging interacts with Ca^{2+} from the media and is fatal for Schwann cells. The simulated body fluid reveals this feature by the formation of cauliflower structures (CaP_N_1200 and Zr_N_1550), and embryonic and nucleic centres (CaP_20_1200, CaP_20_1550 and Ti_N_1200).

The present work suggested that a promising candidate for neural tissue engineering is CaP_N_1200 and Ti_N_1200. Both scaffolds exhibited physical guidance in the lamellar direction *in vitro* and had accurate interlamellar distances with satisfiable mechanical properties. The obtained data from SBF testing showed the bioactive properties of all used materials, where the highest biocompatibility had zirconia ceramic scaffold. Even though the formation of bone-like apatite is not suitable for Schwann cells, the fabricated structures can find a place in bone tissue engineering.

The selected shaping method, freeze-casting, allows the construction of scaffolds with outstanding mechanical properties with required microstructural and macrostructural properties. Selecting the suitable material provides the preparation of scaffolds with biological properties designed for the applied environment. Future research is necessary, but this work demonstrated a promising outcome.

8 LIST OF REFERENCES

[1] WIERINGA, Paul A., Ana Rita GONÇALVES DE PINHO, Silvestro MICERA, Richard J. A. WEZEL a Lorenzo MORONI, 2018. Biomimetic Architectures for Peripheral Nerve Repair: A Review of Biofabrication Strategies. Advanced Healthcare Materials. 7(8). ISSN 2192-2640. Dostupné z: doi:10.1002/adhm.201701164

[2] FRANCIS, Nicola L., Philipp M. HUNGER, Amalie E. DONIUS, Benjamin W. RIBLETT, Antonios ZAVALIANGOS, Ulrike G. K. WEGST a Margaret A. WHEATLEY, 2013. An ice-templated, linearly aligned chitosan-alginate scaffold for neural tissue engineering. Journal of Biomedical Materials Research Part A [online]. 101(12), 3493-3503 [cit. 2020-04-02]. DOI: 10.1002/jbm.a.34668. ISSN 15493296. http://doi.wiley.com/10.1002/jbm.a.34668

[3] DEVILLE, S., 2008. Freeze-Casting of Porous Ceramics: A Review of Current Achievements and Issues. *Advanced Engineering Materials*. **10**(3), 155-169. DOI: 10.1002/adem.200700270. ISSN 14381656. http://doi.wiley.com/10.1002/adem.200700270

[4] BIAZAR, Esmaeil, 2010. Types of neural guides and using nanotechnology for peripheral nerve reconstruction. International Journal of Nanomedicine [online]. DOI: 10.2147/IJN.S11883. ISSN 1178-2013. http://www.dovepress.com/types-of-neural-guides-and-using-nanotechnology-for-peripheral-nerve-r-peer-reviewed-article-IJN

[5] BAIN, J.R, 1998. Peripheral nerve allografting: review of the literature with relevance to composite tissue transplantation. Transplantation Proceedings [online]. 30(6), 2762-2767 [cit. 2020-04-02]. DOI: 10.1016/S0041-1345(98)00804-5. ISSN 00411345. https://linkinghub.elsevier.com/retrieve/pii/S0041134598008045

[6] ZASZCZYNSKA, Angelika, Paweł SAJKIEWICZ a Arkadiusz GRADYS, 2020. Piezoelectric Scaffolds as Smart Materials for Neural Tissue Engineering. *Polymers*. **12**(1). ISSN 2073-4360. Dostupné z: doi:10.3390/polym12010161

[7] BONI, Rossana, Azam ALI, Amin SHAVANDI a Andrew N. CLARKSON, 2018. Current and novel polymeric biomaterials for neural tissue engineering. *Journal of Biomedical Science*. **25**(1). ISSN 1423-0127. Dostupné z: doi:10.1186/s12929-018-0491-8

[8] FROST, Hanna K., Tomas ANDERSSON, Sebastian JOHANSSON, U. ENGLUND-JOHANSSON, Per EKSTRÖM, Lars B. DAHLIN a Fredrik JOHANSSON, 2018. Electrospun nerve guide conduits have the potential to bridge peripheral nerve injuries in vivo: review of the literature with relevance to composite tissue transplantation. Scientific Reports [online]. 8(1), 2762-2767 [cit. 2020-04-02]. DOI: 10.1038/s41598-018-34699-8. ISSN 2045-2322. http://www.nature.com/articles/s41598-018-34699-8

[9] LAMPE, Kyle J., Rachael G. MOONEY, Kimberly B. BJUGSTAD a Melissa J. MAHONEY, 2010. Effect of macromer weight percent on neural cell growth in 2D and 3D nondegradable PEG hydrogel culture. *Journal of Biomedical Materials Research Part A*. **9999A**, NA-NA. ISSN 15493296. Dostupné z: doi:10.1002/jbm.a.32787

[10] LUO, Jian, Richard BORGENS, Riyi SHI a Melissa J. MAHONEY, 2002. Polyethylene glycol immediately repairs neuronal membranes and inhibits free radical production after acute spinal cord injury. *Journal of Neurochemistry*. **83**(2), 471-480. ISSN 00223042. Dostupné z: doi:10.1046/j.1471-4159.2002.01160.x

[11] FLYNN, L, 2003. Fiber templating of poly(2-hydroxyethyl methacrylate) for neural tissue engineering. *Biomaterials*. **24**(23), 4265-4272. ISSN 01429612. Dostupné z: doi:10.1016/S0142-9612(03)00334-X

[12] FARZAMAR, Saeed, Farshid ESMAILPOUR, Majid RAHMATI a Ahmed VAEZ, 2017. Poly-lactic Acid/Gelatin Nanofiber (PLA/GTNF) Conduits Containing Platelet-Rich Plasma for Peripheral Nerve Regeneration. *International Journal of Health Studies*. **3**(2), 29-32. Dostupné z: doi:10.22100/ijhs.v3i2.236

[13] XUE, Chengbin, Nan HU, Yun GU, Yumin YANG, Yan LIU, Jie LIU, Fei DING a Xiaosong GU, 2012. Joint Use of a Chitosan/PLGA Scaffold and MSCs to Bridge an Extra Large Gap in Dog Sciatic Nerve. *Neurorehabilitation and Neural Repair*. **26**(1), 96-106. ISSN 1545-9683. Dostupné z: doi:10.1177/1545968311420444

[14] GARBAYO, E., C.N. MONTERO-MENEI, E. ANSORENA, J.L. LANCIEGO, M.S. AYMERICH a M.J. BLANCO-PRIETO, 2009. Effective GDNF brain delivery using microspheres—A promising strategy for Parkinson's disease. *Journal of Controlled Release*. **135**(2), 119-126. ISSN 01683659. Dostupné z: doi: 10.1016/j.jconrel.2008.12.010

[15] PARENTEAU-BAREIL, Rémi, Robert GAUVIN a François BERTHOD, 2010. Collagen-Based Biomaterials for Tissue Engineering Applications. Materials [online]. 3(3), 1863-1887 [cit. 2020-04-02]. DOI: 10.3390/ma3031863. ISSN 1996-1944. http://www.mdpi.com/1996-1944/3/3/1863

[16] ARCHIBALD, SJ, J SHEFNER, C KRARUP a RD MADISON, 1995. Monkey median nerve repaired by nerve graft or collagen nerve guide tube. *The Journal of Neuroscience*. **15**(5), 4109-4123. ISSN 0270-6474. Dostupné z: doi:10.1523/JNEUROSCI.15-05-04109.1995

[17] CAO, Jiani, Changkai SUN, Hui ZHAO, et al., 2011. The use of laminin modified linear ordered collagen scaffolds loaded with laminin-binding ciliary neurotrophic factor for sciatic nerve regeneration in rats. *Biomaterials*. **32**(16), 3939-3948. ISSN 01429612. Dostupné z: doi: 10.1016/j.biomaterials.2011.02.020

[18] WANGENSTEEN, Kirk J. a Loree K. KALLIAINEN, 2009. Collagen Tube Conduits in Peripheral Nerve Repair: A Retrospective Analysis. *HAND*. **5**(3), 273-277. ISSN 1558-9447. Dostupné z: doi:10.1007/s11552-009-9245-0

[19] SILL, Travis J. a Horst A. VON RECUM, 2008. Electrospinning: Applications in drug delivery and tissue engineering. *Biomaterials*. **29**(13), 1989-2006. ISSN 01429612. Dostupné z: doi: 10.1016/j.biomaterials.2008.01.011

[20] BINAN, Loïc, Charlène TENDEY, Gregory DE CRESCENZO, Rouwayda EL AYOUBI, Abdellah AJJI a Mario JOLICOEUR, 2014. Differentiation of neuronal stem cells into motor neurons using electrospun poly-l-lactic acid/gelatin scaffold: Applications in drug delivery and tissue engineering. *Biomaterials*. **35**(2), 664-674. ISSN 01429612. Dostupné z: doi: 10.1016/j.biomaterials.2013.09.097

[21] NASERI-NOSAR, Mahdi, Majid SALEHI a Shahriar HOJJATI-EMAMI, 2017. Cellulose acetate/poly lactic acid coaxial wet-electrospun scaffold containing citalopram-loaded gelatin nanocarriers for neural tissue engineering applications. *International Journal of Biological Macromolecules*. **103**, 701-708. ISSN 01418130. Dostupné z: doi: 10.1016/j.ijbiomac.2017.05.054

[22] SURI, Shalu a Christine E. SCHMIDT, 2010. Cell-Laden Hydrogel Constructs of Hyaluronic Acid, Collagen, and Laminin for Neural Tissue Engineering. *Tissue Engineering Part A*. **16**(5), 1703-1716. ISSN 1937-3341. Dostupné z: doi: 10.1089/ten.tea.2009.0381

[23] YANG, Ruirui, Caixia XU, Tao WANG, Yuanqi WANG, Jingnan WANG, Daping QUAN a David Y. B. DENG, 2017. PTMAc-PEG-PTMAc hydrogel modified by RGDC and hyaluronic acid promotes neural stem cells' survival and differentiation in vitro. *RSC Advances*. **7**(65), 41098-41104. ISSN 2046-2069. Dostupné z: doi: 10.1039/C7RA06614G

[24] BONI, Rossana, Azam ALI, Amin SHAVANDI a Andrew N. CLARKSON, 2018. Current and novel polymeric biomaterials for neural tissue engineering. *Journal of Biomedical Science*. **25**(1). ISSN 1423-0127. Dostupné z: doi: 10.1186/s12929-018-0491-8

[25] WANG, Shuping, Changkai SUN, Shui GUAN, et al., 2017. Chitosan/gelatin porous scaffolds assembled with conductive poly(3,4-ethylenedioxythiophene) nanoparticles for neural tissue engineering. *Journal of Materials Chemistry B*. **5**(24), 4774-4788. ISSN 2050-750X. Dostupné z: doi: 10.1039/C7TB00608J

[26] GU, Qi, Eva TOMASKOVIC-CROOK, Rodrigo LOZANO, Yu CHEN, Robert M. KAPSA, Qi ZHOU, Gordon G. WALLACE a Jeremy M. CROOK, 2016. Functional 3D Neural Mini-Tissues from Printed Gel-Based Bioink and Human Neural Stem Cells. *Advanced Healthcare Materials*. **5**(12), 1429-1438. ISSN 21922640. Dostupné z: doi: 10.1002/adhm.201600095

[27] ZHANG, Yongbin, Syed F. ALI, Enkeleda DERVISHI, Yang XU, Zhongrui LI, Daniel CASCIANO a Alexandru S. BIRIS, 2010. Cytotoxicity Effects of Graphene and Single-Wall Carbon Nanotubes in Neural Phaeochromocytoma-Derived PC12 Cells. *ACS Nano*. **4**(6), 3181-3186. ISSN 1936-0851. Dostupné z: doi:10.1021/nn1007176

[28] SONG, Qin, Ziyun JIANG, Ning LI, Ping LIU, Liwei LIU, Mingliang TANG a Guosheng CHENG, 2014. Anti-inflammatory effects of three-dimensional graphene foams cultured with microglial cells. *Biomaterials*. **35**(25), 6930-6940. ISSN 01429612. Dostupné z: doi: 10.1016/j.biomaterials.2014.05.002

[29] KIM, Tae-Hyung, Ki-Bum LEE a Jeong-Woo CHOI, 2013. 3D graphene oxide-encapsulated gold nanoparticles to detect neural stem cell differentiation. *Biomaterials*. **34**(34), 8660-8670. ISSN 01429612. Dostupné z: doi: 10.1016/j.biomaterials.2013.07.101

[30] PARK, Dong-Wook, Amelia A. SCHENDEL, Solomon MIKAEL, et al., 2014. Graphene-based carbon-layered electrode array technology for neural imaging and optogenetic applications. *Nature Communications*. **5**(1). ISSN 2041-1723. Dostupné z: doi: 10.1038/ncomms6258

[31] LI, Ning, Qi ZHANG, Song GAO, et al., 2013. Three-dimensional graphene foam as a biocompatible and conductive scaffold for neural stem cells. *Scientific Reports*. **3**(1). ISSN 2045-2322. Dostupné z: doi: 10.1038/srep01604

[32] BARDI, Giuseppe, Antonio NUNES, Lisa GHERARDINI, et al., 2013. Functionalized Carbon Nanotubes in the Brain: Cellular Internalization and Neuroinflammatory Responses. *PLoS ONE*. **8**(11). ISSN 1932-6203. Dostupné z: doi: 10.1371/journal.pone.0080964

[33] IZAK-NAU, Emilia, Kata KENESEI, Kumarasamy MURALI, Matthias VOETZ, Stefanie EIDEN, Victor F. PUNTES, Albert DUSCHL a Emilia MADARÁSZ, 2014. Interaction of differently functionalized fluorescent silica nanoparticles with neural stem- and tissue-type cells. *Nanotoxicology*. **8**(sup1), 138-148. ISSN 1743-5390. Dostupné z: doi: 10.3109/17435390.2013.864427

[34] KOSMIDIS, Efstratios, Georgia KASTRINAKI, Christos SAMSOURIS, Eleni PAPAIOANNOU, Athanasios KONSTANDOPOULOS a George THEOPHILIDIS. Assessing the axonal translocation of CeO2 and SiO2 nanoparticles in the sciatic nerve fibers of the frog: an ex vivo electrophysiological study. *International Journal of Nanomedicine*. ISSN 1178-2013. Dostupné z: doi: 10.2147/IJN.S93663

[35] LAURENTI, Marco a Valentina CAUDA, 2017. ZnO Nanostructures for Tissue Engineering Applications. *Nanomaterials*. **7**(11). ISSN 2079-4991. Dostupné z: doi: 10.3390/nano7110374

[36] PRANG, P, R MULLER, A ELJAOUHARI, et al., 2006. The promotion of oriented axonal regrowth in the injured spinal cord by alginate-based anisotropic capillary hydrogels. Biomaterials [online]. 101(12), 3493-3503 [cit. 2020-04-02]. DOI: 10.1016/j.biomaterials.2006.01.053. ISSN 01429612. https://linkinghub.elsevier.com/retrieve/pii/S0142961206001293

[37] GHORBANI, Farnaz a Ali ZAMANIAN, 2016. Oriented Microstructure in Neural Tissue Engineering: A Review [online]. 07(03) [cit. 2020-04-02]. DOI: 10.4172/2157-

7552.1000182. ISSN 21577552. https://www.omicsonline.org/open-access/oriented-microstructure-in-neural-tissue-engineering-a-review-2157-7552-1000182.php?aid=81832

[38] MÖLLERS, Sven, Ingo HESCHEL, Leon H.H. Olde DAMINK, et al., 2009. Cytocompatibility of a Novel, Longitudinally Microstructured Collagen Scaffold Intended for Nerve Tissue Repair. *Tissue Engineering Part A*. **15**(3), 461-472. ISSN 1937-3341. Dostupné z: doi: 10.1089/ten.tea.2007.0107

[39] STOKOLS, Shula a Mark H TUSZYNSKI, 2004. The fabrication and characterization of linearly oriented nerve guidance scaffolds for spinal cord injury. *Biomaterials*. **25**(27), 5839-5846. ISSN 01429612. Dostupné z: doi:10.1016/j.biomaterials.2004.01.041

[40] CAI, Jie, Xuejun PENG, Kevin D. NELSON, Robert EBERHART a George M. SMITH, 2005. Permeable guidance channels containing microfilament scaffolds enhance axon growth and maturation: A Review of Current Achievements and Issues. *Journal of Biomedical Materials Research Part A*. **75A**(2), 374-386. DOI: 10.1002/jbm.a.30432. ISSN 1549-3296. http://doi.wiley.com/10.1002/jbm.a.30432

[41] RAJESWARI, S. a T.V. SIVASANKARI, 2003. Biological Evaluation of Bioceramic Materials—A Review Trends. *Trends Biomater. Artif. Organs*. **18**.

[42] CRANIN, A. Norman, 1985. Biomaterials: An interfacial approach, L. L. Hench and E. C. Ethridge, New York, Academic, 1982, 384 pp. 14 Chapters, Glossary, Bibliography, and Index. Price. *Journal of Biomedical Materials Research*. **19**(5), 611-612. ISSN 0021-9304. Dostupné z: doi: 10.1002/jbm.820190515

[43] HENCH, Larry L., 1991. Bioceramics: From Concept to Clinic. *Journal of the American Ceramic Society*. **74**(7), 1487-1510. ISSN 0002-7820. Dostupné z: doi: 10.1111/j.1151-2916.1991.tb07132.x

[44] KANNAN, S., A. BALAINURUGAN, S. RAJESVVARI a M. SUBBAIYAN, 2002. Metallic Implants - An Approach for Long Term Applications in Bone Related Defects. Corrosion Reviews. 20(4-5). DOI: 10.1515/CORRREV.2002.20.4-5.339. ISSN 2191-0316. https://www.degruyter.com/view/j/corrrev.2002.20.4-5/corrrev.2002.20.4-5.339/corrrev.2002.20.4-5.339.xml

[45] LEMONS, Jack E., 1996. Ceramics: Past, present, and future. *Bone*. **19**(1), S121-S128. ISSN 87563282. Dostupné z: doi: 10.1016/S8756-3282(96)00128-7

[46] PICONI, C., G. MACCAURO a F. MURATORI, 2003. Alumina and Zirconia Ceramics in Joint Replacements. *Journal of Applied Biomaterials & Biomechanics*. **1**, 19-32. Dostupné z: doi: 10.1177/228080000300100103

[47] MADFA, Ahmed A., Fadhel A. AL-SANABANI, Nasser H. AL-QUDAMI, Jabr S. AL-SANABANI a Abdullah G. AMRAN, 2014. Use of Zirconia in Dentistry: An

Overview. *The Open Biomaterials Journal*. **5**(1), 1-7. ISSN 18765025. Dostupné z: doi: 10.2174/1876502501405010001

[48] ROY, Marcel E, Leo A WHITESIDE, Brian J KATERBERG, Jerry A STEIGER a TariqA NAYFEH, 2007. *Not All Zirconia Femoral Heads Degrade In Vivo*. **465**, 220-226. ISSN 0009-921X. Dostupné z: doi: 10.1097/BLO.0b013e318158b4d3

[49] HANNINK, Richard H. J., Patrick M. KELLY a Barry C. MUDDLE, 2000. Transformation Toughening in Zirconia-Containing Ceramics. *Journal of the American Ceramic Society*. **83**(3), 461-487. ISSN 00027820. Dostupné z: doi: 10.1111/j.1151-2916.2000.tb01221.x

[50] GARVIE, R. C., C. URBANI, D. R. KENNEDY a J. C. MCNEUER, 1984. Biocompatibility of magnesia-partially stabilized zirconia (Mg-PSZ) ceramics. *Journal of Materials Science*. **19**(10), 3224-3228. ISSN 0022-2461. Dostupné z: doi: 10.1007/BF00549808

[51] CHRISTEL, P., A. MEUNIER, M. HELLER, J. P. TORRE a C. N. PEILLE, 1989. Mechanical properties and short-termin vivo evaluation of yttrium-oxide-partially-stabilized zirconia. *Journal of Biomedical Materials Research*. **23**(1), 45-61. ISSN 0021-9304. Dostupné z: doi: 10.1002/jbm.820230105

[52] KUSAKAWA, You, Eiji YOSHIDA a Tohru HAYAKAWA, 2017. Protein Adsorption to Titanium and Zirconia Using a Quartz Crystal Microbalance Method. *BioMed Research International*. **2017**, 1-8. ISSN 2314-6133. Dostupné z: doi: 10.1155/2017/1521593

[53] TOSIRIWATANAPONG, Terawat a Weerachai SINGHATANADGIT, 2018. Zirconia-Based Biomaterials for Hard Tissue Reconstruction. *Bone and Tissue Regeneration Insights*. **9**. ISSN 1179-061X. Dostupné z: doi: 10.1177/1179061X18767886

[54] SKOCAJ, Matej, Metka FILIPIC, Jana PETKOVIC a Sasa NOVAK, 2011. Titanium dioxide in our everyday life; is it safe? Radiology and Oncology. 45(4). ISSN 1581-3207. Dostupné z: doi: 10.2478/v10019-011-0037-0

[55] EL-SAYED, Naglaa Salem, Mohamed EL-SAKHAWY, Nicolas BRUN, Peter HESEMANN a Samir KAMEL, 2018. New approach for immobilization of 3-aminopropyltrimethoxysilane and TiO2 nanoparticles into cellulose for BJ1 skin cells proliferation. *Carbohydrate Polymers*. **199**, 193-204. ISSN 01448617. Dostupné z: doi: 10.1016/j.carbpol.2018.07.004

[56] ISMAIL, Nur Arifah, Khairul Anuar MAT AMIN a Mohd Hasmizam RAZALI, 2018. Novel gellan gum incorporated TiO2 nanotubes film for skin tissue engineering. *Materials Letters*. **228**, 116-120. ISSN 0167577X. Dostupné z: doi: 10.1016/j.matlet.2018.05.140

[57] CHEN, Yunhui, Jessica Ellen FRITH, Ali DEHGHAN-MANSHADI, Hooyar ATTAR, Damon KENT, Nicolas Dominique Mathieu SORO, Michael J. BERMINGHAM a Matthew S. DARGUSCH, 2017. Mechanical properties and biocompatibility of porous titanium scaffolds for bone tissue engineering. *Journal of the Mechanical Behavior of Biomedical Materials*. **75**, 169-174. ISSN 17516161. Dostupné z: doi: 10.1016/j.jmbbm.2017.07.015

[58] HENCH, Larry L., 1991. Bioceramics: From Concept to Clinic. *Journal of the American Ceramic Society*. **74**(7), 1487-1510. ISSN 0002-7820. Dostupné z: doi: 10.1111/j.1151-2916.1991.tb07132.x

[59] SAMAVEDI, Satyavrata, Abby R. WHITTINGTON a Aaron S. GOLDSTEIN, 2013. Calcium phosphate ceramics in bone tissue engineering: A review of properties and their influence on cell behaviour. *Acta Biomaterialia*. **9**(9), 8037-8045. ISSN 17427061. Dostupné z: doi: 10.1016/j.actbio.2013.06.014

[60] MAGALHÃES, M. Clara F. a M. Odete G. COSTA, 2018. On the solubility of whitlockite, Ca9Mg(HPO4)(PO4)6, in aqueous solution at 298.15 K. *Monatshefte für Chemie - Chemical Monthly*. **149**(2), 253-260. ISSN 0026-9247. Dostupné z: doi: 10.1007/s00706-017-2129-z

[61] WALLACE, Betty M. a Walter E. BROWN, 1971. Stoichiometric Composition of Whitlockite. *Journal of Dental Research*. **50**(2), 343-346. ISSN 0022-0345. Dostupné z: doi: 10.1177/00220345710500023701

[62] JIN, Yuan-Zhe, Guang-Bin ZHENG, Hae Lin JANG, Kyung Mee LEE a Jae Hyup LEE, 2019. Whitlockite Promotes Bone Healing in Rabbit Ilium Defect Model. *Journal of Medical and Biological Engineering*. **39**(6), 944-951. ISSN 1609-0985. Dostupné z: doi: 10.1007/s40846-019-00471-0

[63] JEONG, Jiwoon, Jung Hun KIM, Jung Hee SHIM, Nathaniel S. HWANG a Chan Yeong HEO, 2019. Bioactive calcium phosphate materials and applications in bone regeneration. *Biomaterials Research*. **23**(1). ISSN 2055-7124. Dostupné z: doi: 10.1186/s40824-018-0149-3

[64] RAPACZ-KMITA, A., C. PALUSZKIEWICZ, A. ŚLÓSARCZYK a Z. PASZKIEWICZ, 2005. FTIR and XRD investigations on the thermal stability of hydroxyapatite during hot pressing and pressureless sintering processes. *Journal of Molecular Structure*. **744-747**, 653-656. ISSN 00222860. Dostupné z: doi: 10.1016/j.molstruc.2004.11.070

[65] PATEL, N., S. M. BEST, W. BONFIELD, I. R. GIBSON, K. A. HING, E. DAMIEN a P. A. REVELL. *Journal of Materials Science: Materials in Medicine*. **13**(12), 1199-1206. ISSN 09574530. Dostupné z: doi: 10.1023/A:1021114710076

[66] BOHNER, Marc a Jacques LEMAITRE, 2009. Can bioactivity be tested in vitro with SBF solution? *Biomaterials*. **30**(12), 2175-2179. ISSN 01429612. Dostupné z: doi: 10.1016/j.biomaterials.2009.01.008

[67] POPP, Jenni R., Kate E. LAFLIN, Brian J. LOVE a Aaron S. GOLDSTEIN, 2011. In vitro evaluation of osteoblastic differentiation on amorphous calcium phosphate-decorated poly(lactic-co-glycolic acid) scaffolds. *Journal of Tissue Engineering and Regenerative Medicine*. **5**(10), 780-789. ISSN 19326254. Dostupné z: doi: 10.1002/term.376

[68] DEVILLE, Sylvain, Eduardo SAIZ, Antoni P. TOMSIA, Robert EBERHART a George M. SMITH, 2006. Freeze casting of hydroxyapatite scaffolds for bone tissue engineering: A Review of Current Achievements and Issues. Biomaterials. 27(32), 5480-5489. DOI: 10.1016/j.biomaterials.2006.06.028. ISSN 01429612. https://linkinghub.elsevier.com/retrieve/pii/S0142961206005801

[69] LI, W L, K LU, J Y WALZ, Robert EBERHART a George M. SMITH, 2013. Freeze casting of porous materials: review of critical factors in microstructure evolution. International Materials Reviews. 57(1), 37-60. DOI: 10.1179/1743280411Y.0000000011. ISSN 0950-6608. http://www.tandfonline.com/doi/full/10.1179/1743280411Y.0000000011

[70] Wegst, U. G. K., Schecter, M., Donius, A. E., & Hunger, P. M. (2010). Biomaterials by freeze casting. *Philosophical Transactions of the Royal Society A: Mathematical, Physical and Engineering Sciences, 368(1917), 2099–2121.* doi: 10.1098/rsta.2010.0014

[71] WASCHKIES, Thomas, Rainer OBERACKER, Michael J. HOFFMANN a E.G. CRAVALHO, 2009. Control of Lamellae Spacing During Freeze Casting of Ceramics Using Double-Side Cooling as a Novel Processing Route. Journal of the American Ceramic Society. 92(1), S79-S84. DOI: 10.1111/j.1551-2916.2008.02673.x. ISSN 00027820. http://doi.wiley.com/10.1111/j.1551-2916.2008.02673.x

[72] MEYERS, Marc André, Po-Yu CHEN, Albert Yu-Min LIN a Yasuaki SEKI, 2008. Biological materials: Structure and mechanical properties. *Progress in Materials Science*. **53**(1), 1-206. ISSN 00796425. Dostupné z: doi: 10.1016/j.pmatsci.2007.05.002

[73] MUNCH, Etienne, Eduardo SAIZ, Antoni P. TOMSIA a Sylvain DEVILLE, 2009. Architectural Control of Freeze-Cast Ceramics Through Additives and Templating. *Journal of the American Ceramic Society*. **92**(7), 1534-1539. ISSN 00027820. Dostupné z: doi: 10.1111/j.1551-2916.2009.03087.x

[74] SHAO, Gaofeng, Dorian A. H. HANAOR, Xiaodong SHEN a Aleksander GURLO, 2020. Freeze Casting: From Low-Dimensional Building Blocks to Aligned Porous Structures—A Review of Novel Materials, Methods, and Applications. *Advanced Materials*. **32**(17). ISSN 0935-9648. Dostupné z: doi: 10.1002/adma.201907176

[75] KÖRBER, Ch., G. RAU, M.D. COSMAN a E.G. CRAVALHO, 1985. Interaction of particles and a moving ice-liquid interface. Journal of Crystal Growth. 72(3), 649-662. DOI: 10.1016/0022-0248(85)90217-9. ISSN 00220248. https://linkinghub.elsevier.com/retrieve/pii/0022024885902179

[76] CHINO, Yasumasa, David C. DUNAND, M.D. COSMAN a E.G. CRAVALHO, 2008. Directionally freeze-cast titanium foam with aligned, elongated pores. Acta Materialia. 56(1), 105-113. DOI: 10.1016/j.actamat.2007.09.002. ISSN 13596454. https://linkinghub.elsevier.com/retrieve/pii/S1359645407006076

[77] FRANKS, Felix, Rainer OBERACKER, Michael J. HOFFMANN a E.G. CRAVALHO, 1998. Freeze-drying of bioproducts: putting principles into practice. European Journal of Pharmaceutics and Biopharmaceutics. 45(3), 221-229. DOI: 10.1016/S0939-6411(98)00004-6. ISSN 09396411. https://linkinghub.elsevier.com/retrieve/pii/S0939641198000046

[78] ABDELWAHED, W, G DEGOBERT, S STAINMESSE a H FESSI, 2006. Freeze-drying of nanoparticles: Formulation, process and storage considerations☆. Advanced Drug Delivery Reviews. 58(15), 1688-1713. DOI: 10.1016/j.addr.2006.09.017. ISSN 0169409X. https://linkinghub.elsevier.com/retrieve/pii/S0169409X06001840

[79] EN 623-2. Advanced technical ceramics. Monolithic ceramics. General and textural properties. Determination of density and porosity. British standard, 1993.

[80] MAULI AGRAWAL, J. a Robert B. RAY, 2001. Biodegradable polymeric scaffolds for musculoskeletal tissue engineering. *Journal of Biomedical Materials Research*. **55**(2), 141-150. Dostupné z: doi: 10.1002/1097-4636(200105)55:2<141::aid-jbm1000>3.0.co;2-j

[81] CHANG, Hsin-I a Yiwei WANG, 2011. Cell Responses to Surface and Architecture of Tissue Engineering Scaffolds. *Regenerative Medicine and Tissue Engineering - Cells and Biomaterials*. InTech, 2011-08-29. ISBN 978-953-307-663-8. Dostupné z: doi: 10.5772/21983

[82] KOKUBO, Tadashi a Hiroaki TAKADAMA, 2006. How useful is SBF in predicting in vivo bone bioactivity? *Biomaterials*. **27**(15), 2907-2915. ISSN 01429612. Dostupné z: doi: 10.1016/j.biomaterials.2006.01.017

[83] NAGAPPAN, Palaniappan Ganesh, Hong CHEN a De-Yun WANG, 2020. Neuroregeneration and plasticity: a review of the physiological mechanisms for achieving functional recovery postinjury. *Military Medical Research*. **7**(1). ISSN 2054-9369. Dostupné z: doi: 10.1186/s40779-020-00259-3

[84] PEJCHALOVÁ, Lucie. Přizpůsobení fázového složení a mikrostruktury vápenatých fosforečnanů aplikovaných v regenerativní medicíně. Brno, 2020. Dostupné také z: https://www.vutbr.cz/studenti/zav-prace/detail/122609. Diplomová práce. Vysoké učení technické v Brně, Fakulta chemická, Ústav fyzikální a spotřební chemie. Vedoucí práce David Salamon.

[85] KIM, Hyun-Min, Teruyuki HIMENO, Tadashi KOKUBO a Takashi NAKAMURA, 2005. Process and kinetics of bonelike apatite formation on sintered hydroxyapatite in a simulated body fluid. *Biomaterials*. **26**(21), 4366-4373. ISSN 01429612. Dostupné z: doi:10.1016/j.biomaterials.2004.11.022

[86] YANG, Kai, Yuhui YAN, Lin-Ling ZHANG, Michael AGRESTI, Hani MATLOUB, John LOGIUDICE, Robert HAVLIK a Ji-Geng YAN, 2017. Increasing Calcium Level Limits Schwann Cell Numbers In Vitro following Peripheral Nerve Injury. *Journal of Reconstructive Microsurgery*. **33**(06), 435-440. ISSN 0743-684X. Dostupné z: doi: 10.1055/s-0037-1599836

[87] RAJDEV, S. a I.J. REYNOLDS, 1994. Glutamate-induced intracellular calcium changes and neurotoxicity in cortical neuronsin vitro: Effect of chemical ischemia. *Neuroscience*. **62**(3), 667-679. ISSN 03064522. Dostupné z: doi: 10.1016/0306-4522(94)90468-5

[88] UCHIDA, Masaki, Hyun-Min KIM, Tadashi KOKUBO, Fumiaki MIYAJI a Takashi NAKAMURA, 2001. Bonelike Apatite Formation Induced on Zirconia Gel in a Simulated Body Fluid and Its Modified Solutions. *Journal of the American Ceramic Society*. **84**(9), 2041-2044. ISSN 00027820. Dostupné z: doi: 10.1111/j.1151-2916.2001.tb00955.x

[89] QUAN, Hongxuan, Yoon-Kyung PARK, Seong-Kyun KIM, Seong-Joo HEO, Jai-Young KOAK, Jung-Suk HAN a Joo-Hee LEE, 2016. *Surface Characterization and Human Stem Cell Behaviors of Zirconia Implant Disks Biomimetic-Treated in Simulated Body Fluid*. **31**(4), 928-938. ISSN 08822786. Dostupné z: doi:10.11607/jomi.4376

[90] TSAMPAS, M. N., F. M. SAPOUNTZI a P. VERNOUX, 2015. *Applications of yttria stabilized zirconia (YSZ) in catalysis*. **5**(11), 4884-4900. ISSN 2044-4753. Dostupné z: doi: 10.1039/C5CY00739A

[91] AMAT, Noor Faeizah, Andanastuti MUCHTAR, Muhammad Sufiyan AMRIL, Mariyam Jameelah GHAZALI a Norziha YAHAYA, 2019. Effect of sintering temperature on the aging resistance and mechanical properties of monolithic zirconia. *Journal of Materials Research and Technology*. **8**(1), 1092-1101. ISSN 22387854. Dostupné z: doi: 10.1016/j.jmrt.2018.07.017

[92] LI, Panjian, Chikara OHTSUKI, Tadashi KOKUBO, Kazuki NAKANISHI, Naohiro SOGA a Klaas DE GROOT, 1994. The role of hydrated silica, titania, and alumina in inducing apatite on implants. *Journal of Biomedical Materials Research*. **28**(1), 7-15. ISSN 0021-9304. Dostupné z: doi: 10.1002/jbm.820280103

[93] HAYAKAWA, Satoshi, Kanji TSURU, Keita UETSUKI, Keisuke AKASAKA, Yuki SHIROSAKI a Akiyoshi OSAKA, 2015. Calcium phosphate crystallization on titania in a flowing Kokubo solution. *Journal of Materials Science: Materials in Medicine*. **26**(8). ISSN 0957-4530. Dostupné z: doi:10.1007/s10856-015-5552-x

[94] SCOTTI, Kristen L. a David C. DUNAND, 2018. Freeze casting – A review of processing, microstructure and properties via the open data repository, FreezeCasting.net. *Progress in Materials Science*. **94**, 243-305. ISSN 00796425. Dostupné z: doi:10.1016/j.pmatsci.2018.01.001

[95] MURALITHRAN, G a S RAMESH, 2000. The effects of sintering temperature on the properties of hydroxyapatite. *Ceramics International*. **26**(2), 221-230. ISSN 02728842. Dostupné z: doi:10.1016/S0272-8842(99)00046-2

[96] GHORBANI, Farnaz, Ali ZAMANIAN, Fatemeh KERMANIAN a Atefeh SHAMOOSI, 2019. A bioinspired 3D shape olibanum-collagen-gelatin scaffolds with tunable porous microstructure for efficient neural tissue regeneration. *Biotechnology Progress*. **36**(1). ISSN 8756-7938. Dostupné z: doi:10.1002/btpr.2918

[97] YAN, J.-G., M. AGRESTI, L.-L. ZHANG, H. S. MATLOUB a J. R. SANGER, 2012. Negative Effect of High Calcium Levels on Schwann Cell Survival. *Neurophysiology*. **44**(4), 274-278. ISSN 0090-2977. Dostupné z: doi:10.1007/s11062-012-9297-6

[98] DAS, Apurba a D. PAMU, 2019. A comprehensive review on electrical properties of hydroxyapatite based ceramic composites. *Materials Science and Engineering: C*. **101**, 539-563. ISSN 09284931. Dostupné z: doi:10.1016/j.msec.2019.03.077

[99] POSNER, Aaron S. a Foster BETTS, 1975. Synthetic amorphous calcium phosphate and its relation to bone mineral structure. *Accounts of Chemical Research*. **8**(8), 273-281. ISSN 0001-4842. Dostupné z: doi:10.1021/ar50092a003

9 LIST OF ABBREVATIONS

3PB	Three-point bending test
ACP	Nano-crystalline calcium phosphate
BCP	Biphasic calcium phosphate
CaP	Calcium phosphate
CNT	Carbon nanotubes
CPC	Calcium phosphate ceramic
CTP	Calcium titanium phosphate
CY3Z	3% yttria-stabilized zirconia
CZ	Calcium zirconate
CZP	Calcium zirconium phosphate
DAPI	4´,6-diamidino-2-phenylindole
DRG	Dorsal-root gangliom
ECM	Extracellular matrix
FBS	Fetal bovine serum
FDA	Food and Drug Administration
FEI	Field emission electron microscope
FIB	Focused ion beam
FSZ	Fully stabilized zirconia
HAP	Hydroxyapatite
HCA	Hydroxycarbonate apatite
HMDS	Hexamethyldisilazane
MTT	3-(4,5-dimethylthiazol-2-yl)-2,5-diphenyltetrazolium bromide
MWCNT	Multi-walled carbon nanotubes
NSC	Neural stem cells
PAA	Polyacrylic acid
PBS	Phosphate-buffer saline

PCL	Polycaprolactone
PEG	Polyethylene glycol
PGA	Polyglycolide
pHEMA	Polyhydroxyethylmethacrylate
PLA	Polylactic acid
PLGA	Poly(lactic acid-co-glycolic acid)
PS	Polystyrene
PSZ	Partially stabilized zirconia
PTFE	Polytetrafluorethylene
PVA	Polyvinyl alcohol
PVC	Polyvinyl chloride
SBF	Simulated body fluid
SEM	Scanning electron microscopy
SWCNT	Single-walled carbon nanotubes
TBA	Tert-butyl alcohol
TCP	Tricalcium phosphate
TZ-8Y	8% yttria-stabilized zirconia
TZP	Tetragonal zirconia polycrystals
UV	Ultraviolet
WH	Whitlockite
XRD	X-ray diffraction
YSZ	Yttria-stabilized zirconia